Broadband Electrooptic Modulators Based on Gallium Arsenide Materials

by

Orit A. Shamir

M.Eng. Electrical Engineering and Computer Science
Massachusetts Institute of Technology 2008
and
S.B. Electrical Engineering
Massachusetts Institute of Technology 2007

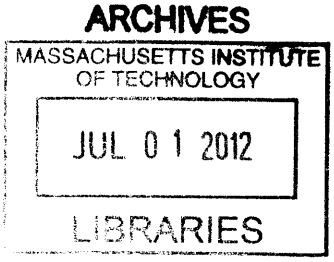

Submitted to the Department of Electrical Engineering and Computer Science in partial fulfillment of the requirements for the degree of

Doctor of Philosophy in Electrical Engineering and Computer Science

at the
MASSACHUSETTS INSTITUTE OF TECHNOLOGY

June 2012

Author .....
Orit A. Shamir
Department of Electrical Engineering and Computer Science
May 25, 2012

Certified by .....
Leslie A. Kolodziejski
Professor of Electrical Engineering and Computer Science
Thesis Supervisor

Accepted by .....
Leslie A. Kolodziejski
Chair, Department Committee on Graduate Students

Broadband Electrooptic Modulators Based on Gallium Arsenide Materials

by

Orit A. Shamir

Submitted to the Department of Electrical Engineering and Computer Science
on May 25, 2012, in partial fulfillment of the
requirements for the degree of
Doctor of Philosophy in Electrical Engineering and Computer Science

Abstract

Optical Arbitrary Waveform Generation (OAWG) combines frequency combs and frequency-by-frequency pulse shapers to synthesize optical waveforms. The OAWG technique has a wide variety of applications, ranging from high resolution imaging, Light Detecting and Ranging (LIDAR) systems for high precision distance measuring, high-speed communication networks, and high capacity transmission systems.

Frequency combs, generated by Ti:Sapphire mode-locked lasers, span the optical spectrum from λ=0.65μm to 1.1μm and necessitate the development of compatible modulator devices which could be based on materials in the III-V semiconductor groups for the construction of an optical arbitrary waveform generation system. An OAWG system in the visible and near-infrared will motivate many novel applications yet to be envisioned, and will allow the transfer of technologies currently operating in the radio frequencies to the optical spectrum.

The design of electrooptic ultra-broadband modulators operating at wavelengths longer than λ=0.65μm is investigated. Novel epitaxial heterostructures lattice-matched to GaAs - a p-i-n structure with a dilute core and a n-i-n Metal Oxide Semiconductor (MOS) heterostructure offering superior mode confinement - are modeled, and grown. The electric field distribution in the n-i-n MOS structure is examined through simulations and capacitance-voltage measurements. A Mach-Zehnder Interferometer modulator design is proposed, employing both multimode interferometers and Y-junctions as power splitters. A self-aligned fabrication mask set and process are developed and demonstrated, verifying the performance of the modulator epitaxial heterostructures through the demonstration of waveguiding and optical power splitting. A mask set is offered for improved processing yield and a fabrication process is designed to enable push-pull operation of the n-i-n MOS modulator.

Thesis Supervisor: Leslie A. Kolodziejski
Title: Professor of Electrical Engineering and Computer Science

Acknowledgments

For the past decade, MIT has been my home. I have been inspired, amazed, confused, and frightened, finding myself drinking from the fire hose on a daily basis. I am so honored to have been a part of the MIT community, and grateful that I will emerge at the same end of the infinite corridor through which I entered in September 2002. There are many people who have offered support and guidance to me throughout the years, and without whom the work I discuss in this thesis would not have been possible.

I want to express my deepest gratitude to my advisor, Professor Leslie Kolodziejski, who has inspired me in more ways than I can count. I am grateful for her patience and humor, for her devotion to the graduate student population at MIT and to the women of the department, and for her unwavering support. Even at the hardest of times, Leslie always had wisdom to share, and could always find the light at the end of the tunnel (or waveguide). She has given me skills that I will carry with me for the rest of my life, and I feel most fortunate to have such a wonderful role model, advisor, and friend.

Dr. Gale Petrich has been a second advisor to me since my first day in the Integrated Photonic Devices and Materials Group. He has taught me to leave no stone unturned, to ask the right questions, and to think outside the box. I rarely let a day go by over the past 6 years without asking Gale a question or running my latest result by him. I am so proud of the work I have accomplished, and I owe much of that to Gale's assistance and creativity.

I am grateful to have had the opportunity to collaborate with my committee members, Professor Erich Ippen and Professor Franz Kärtner, who are two of the most brilliant minds I have come across during my time at MIT. Their patience, curiosity, and willingness to impart their knowledge have made my Ph.D. a wonderful and exciting experience. I am honored to have worked with them, and I will always remember our bi-monthly Optical Arbitrary Waveform Generation project meetings fondly.

I have had several advisors and mentors over the years who have taken an active interest in my academic career and encouraged me to work harder and dream bigger. I am thankful to have the ear of Professor Rafael Reif, who advised me during my time as an undergraduate at MIT, but who continued to offer advice throughout my Ph.D. My graduate academic advisor, Professor Tomas Palacios, was always genuinely interested in my research and always excited to share the latest progress in his field despite his busy schedule. Professor

Yoel Fink has taken me under his wing, and has been a most wonderful mentor, offering his support even moments before my defense. And Professor Arthur Smith, who admitted me to the M.Eng. program, who wrote the recommendation for my Ph.D. application, and who encouraged me to find a balance between work and play.

Jason Plant and Dr. Reuel Swint of Lincoln Laboratories came to my rescue on several occasions, and I greatly appreciate their generosity and efforts. I truly enjoyed the conversations that took place as we waited for processes to finish.

Prof. Marcus Dahlem and Jonathan Morse were instrumental in performing the measurements that are presented in this thesis. I enjoyed working with them each and every night, and their humor and high spirits made this collaboration particularly fun. The many members of the Optical Arbitrary Waveform Generation initiative - Dr. Andrew Benedick, Dr. Hyunil Byun, Dr. Noah Chang, Dr. David Chao, Dr. Jeff Chen, Dr. Ali Motamedi, Dr. Michelle Sander, and Dr. Jason Sickler - exposed me to new areas of research, and were a pleasure to work with. Though we were merely colleagues at first, close friendships have since formed, and I consider myself to be very lucky to have such people of caliber in my life.

The tremendous technical help and levity provided by Jim Daley and Dennis Ward allowed me to push through many obstacles. Their invaluable contributions to the work of so many students, including my own, cannot be overstated, and I can only hope that I have enriched their lives as they have enriched mine.

I have benefited from the use of the NanoStructures Laboratory, led by Professor Henry Smith and Professor Karl Berggren. The members of the laboratory have helped me get my footing, and have passed on to me a wealth of knowledge. I am grateful for the friendship of Dr. Euclid Moon, who has often been called upon to aid in diagnosing the cause of a strange fabrication result. I also wish to thank the entire staff of the Microsystems Technology Laboratories for providing a cheerful work environment, and for keeping the clean room up and running each and every day.

I could not imagine sharing an office with a better friend than Dr. Ta-Ming Shih. Our many, many conversation, few pertaining to research, have been a source of great laughter and joy for me. From our April Fools' blog to our carpet-tearing operation, I believe that we have put an everlasting mark on 36-295. He has been a motivating colleague, a patient sounding board for my research woes, and a trusted friend. After experiencing 6 years of

long days in the clean room and late nights in the office, I am excited that we will also take our final steps at MIT together.

Over the years, I have grown close to Dr. Sheila Nabanja, a smart, ambitious, and humorous member of the group. Her dedication to research and tenacity were awe-inspiring, and I only wish that our projects had overlapped more often. Our 'happy monday' trio with Dr. Michelle Sander may have been short-lived, but has left me with amusing memories.

I want to acknowledge the members of the Integrated Photonic Devices and Materials group who have been my colleagues and friends over the past 6 years: Amy Chi, Dr. Ryan Williams, Dr. Reginald Bryant, Alejandro Grine, Dr. Natalija Jovanovic, and Mohammad Araghchini.

I offer a heartfelt thank you to the members of the Advanced Semiconductor Materials and Devices, particularly Bin Lu, Omair Saadat, and Allen Hsu. The electrical simulations and characterization of the structures discussed in this work were made possible through the help of Bin and Omair. I appreciate the time we have spent together, and look forward to hearing about the many great things that you will all achieve in the future.

I have much appreciation for my remarkable MIT colleagues who have shared many nights and weekends with me in the lab, took coffee breaks with me, or shared a much needed beer after work: Dr. Kerry Cheung, Dr. Nicole DiLello, Dr. Ivan Nausieda, Dr. Amil Patel, Katia Shtyrkova, Dr. Jaime Viegas, and Eric Winokur.

There are many beloved friends, both at and outside of MIT, whose support and encouragement has sustained me over the years. Dr. Pedro Pinto, Tomer Levkov, Arlis Reynolds, Valerie Kuo, Sivan Almog, Evelyn Kapusta, Olympia Banerjee, and many wonderful individuals who could fill several more pages have been my backbone throughout this process. I must also thank my Israeli family abroad - Yaniv and Gila Corem, Yaeko Elmaleh, Yoni Goldberg, Tal Goldenberg, Shay Maymon, Oded Polat, Ofer Shapira, Tal Tchwella, and Itai Turbahn - for making me feel at home here in Boston.

My family has been my greatest cheerleader, and words cannot express the gratitude I have for their presence in my life. I could not wish for more loving brothers, who I have admired since taking my first steps. My grandparents have taught me the value of hard work, and have shown me unconditional love and support that give me strength daily. My parents deserve infinite words of praise for the opportunities and guidance they have selflessly given me. I cannot thank them enough for walking this path with me.

And finally, I am grateful to MIT, for opening its doors to me for a third and final time. It has been an unforgettable adventure.

I dedicate this work to the members of my family - past, present, and future.

Cambridge, 2012 O A S

Contents

List of Figures

List of Tables

Chapter 1

Introduction

The emergence of the solid state laser [3] in 1960 marked the onset of research and development in optical components and devices. Less than two decades later, the optics and communication fields began to overlap as major telecommunication carriers first invested in fiber-optic links at 0.8μm, and later linked continents with transoceanic optical fibers operating at 1.55μm. Today, optical networks continue to thrive due to their bandwidth capability, characteristic high speeds, low losses and cost [4], enabling communication through the encoding of information onto an optical frequency carrier - an integral function known as optical signal modulation.

There are a variety of optical modulator designs, including, but not limited to acousto-optic, electroabsorption, electrooptic, liquid crystal and fiber-optic modulators. Aside from use in telecommunications, optical modulation serves a fundamental function in a wide variety of applications such as optical displays and in measurements. Recently, modulators have found use in optical arbitrary waveform generation (OAWG), a spectral line-by-line pulse shaping technique that produces arbitrary temporal waveforms by phase and amplitude modulation of the spectral lines across an entire bandwidth of a coherent optical frequency comb [5].

The OAWG system, schematically shown in Figure 1-1, is composed of a carrier-envelope phase-stabilized femtosecond oscillator, parallel sets of phase and amplitude modulators, a demultiplexer and multiplexer (often in the form of gratings). The system separates the frequency components of a mode-locked fiber-laser into an optical frequency comb, and employs both broadband phase and amplitude modulators to alter the properties of

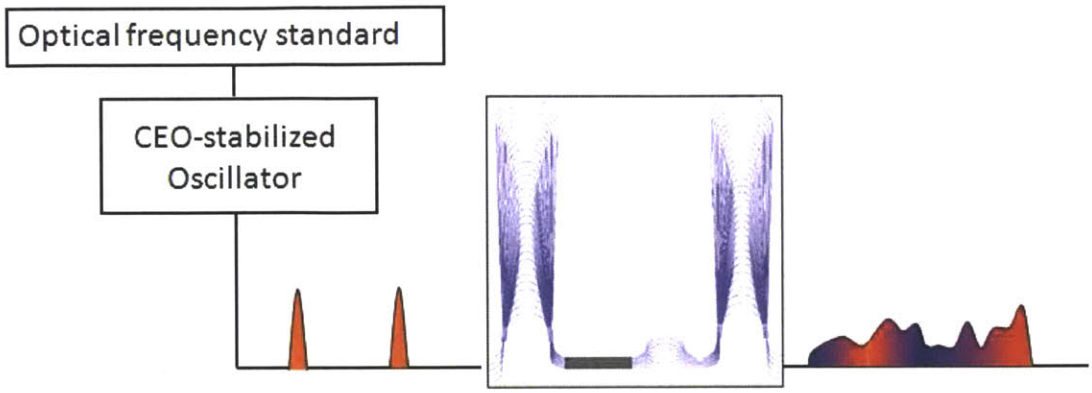

Figure 1-1: Schematic of the optical arbitrary waveform generation (OAWG) system. An optical pulse train that is generated by a mode-locked short pulse laser is passed through a demultiplexer in order to decompose its frequency spectrum. A series of modulators manipulate the phase and amplitude of each frequency component, which are then recombined through a multiplexer at the output to create an optical arbitrary waveform.

individual frequency components. Upon multiplexing (recombination) of the modulated spectrum, the system outputs an altered waveform.

Pulse shaping technology that is based on the InP-InGaAsP material system has been reported at the telecommunication wavelength [6, 7]. These pulse shaping devices are based on mode-locked laser-compatible fabrication processes that encourage the possibility of full system integration, but most current OAWG systems are based on slow reconfigurable elements such as acousto-optic [8] or liquid crystal modulators [9, 10, 11], discrete bulk components that limit performance, stability, scalability and reliability [12]. Integrated photonic optical arbitrary waveform generators will provide high-resolution, monolithic, ultra-compact semiconductor encoder-decoders that support high-speed ($>$ 40 GHz/channel) reconfiguration, scalability and reliability.

The manipulation of broadband frequency combs and the generation of broadband waveforms is made possible by the parallel processing of spatially separated frequency lines. Such high resolution control of femtosecond elements of the electric field enables several technologies. For instance, the performance of carrier-free ultra-wideband (UWB) wireless devices that are commonly used in imaging, biomedical, and surveillance systems are sensitive to the selection of an impulse signal [13]. Such devices would greatly benefit from the freedom of waveform modulation that is granted with OAWG systems. OAWG is also used in optical

code-division multiple-access (OCDMA) and UWB communication systems at 1.55μm [14], high bandwidth radar and high-speed communication networks, high capacity transmission systems [15, 16], and in generating and processing of high bandwidth RF and optical communications signals that require phase and amplitude control [17]. The works of Cundiff et al [18] and Weiner [19] can be consulted for more information on these and additional applications.

1.1 OAWG Based on Ti:Sapphire-Generated Optical Combs

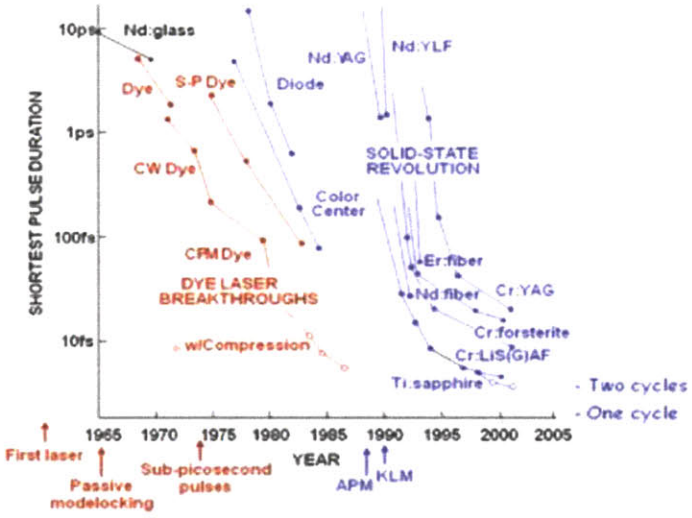

Figure 1-2: Evolution in laser technologies and developments in the generation of short pulses over the past decades [1].

Figure 1-2 displays the progress over the past decades in the development of ultra-short pulse-generating laser. Significant efforts have been made to shorten the duration of pulses, which has in turn produced broader optical spectrums. Lasers that output pulses on the order of a few femtoseconds, such as the Ti:Sapphire laser, first realized by Moulton [20], have spectrums hundreds of nanometers wide. High resolution optical arbitrary waveform generation necessitates optical frequency combs with repetition rates in the GHz range, that are generated by broadband spectrum optical sources. Stabilized optical combs have been demonstrated using both a Ti:Sapphire and fiber laser sources [21, 22, 23]. At λ=1.55μm, optical frequency combs generated by fiber lasers for OAWG applications are pursued due

to the availability of high-speed optical modulators at this wavelength. At λ=0.8μm, the stable, optically broadband, carrier-enveloped offset (CEO) locked titanium-doped sapphire laser (Ti:sapphire being the amplifying medium), generates ultrashort, femtosecond pulses ([24]) and hence frequency combs. The high gain of Ti:Sapphire lasers around λ=0.8μm encourages exploration of ultra broadband modulators in this wavelength regime for the development of a broadband OAWG system for utilization in communications, research and many more applications that have yet to be envisioned.

1.2 Thesis Organization

Chapter 2 examines the theory behind the physical electroabsorption (EA) and electrooptic (EO) effects that contribute to optical signal modulation. The advantage of the electrooptic effect over electroabsorption due to broadband performance capability is explained, and directional coupler and Mach Zehnder Interferometer (MZI) devices that operate on these effects are introduced. The mathematical theory of both devices is provided to support the adoption of low-power MZI modulators.

Chapter 3 provides an overview of past work in the field and the previously pursued ridge waveguide modulator design that is based on a p-i-n configuration. The design and simulation of optical waveguides and power splitters is explored, and a mask set is offered. The subsequent fabrication process and testing results are presented, motivating the development of a novel n-i-n, Metal-Oxide-Semiconductor (MOS) epitaxial heterostructure. The electrical performance of the n-i-n MOS modulator is investigated and the fabrication, design benefits and disadvantages of the heterostructure are highlighted.

Chapter 4 introduces a self-aligned mask set that improves upon the former by offering full power transfer between optical components of the waveguide. The mask set is applied to a specialized fabrication process in the pursuit of a novel n-i-n epitaxial heterostructure-based modulator. Measurements and a thorough analysis of the results are reported, and an optimized fabrication process is detailed and verified through the characterization, providing a significant improvement in waveguide operation and optical losses. Additionally, the modeling of power splitting devices is discussed, and the characterization of fabricated multimode interferometers (MMIs) and Y-splitters is presented and compared to theory, verifying the performance of modulator components that are based on the n-i-n structure.

Chapter 5 concludes the thesis with a summary of the work that was accomplished and offers future directions of research in the effort to construct optical modulators operating at λ=0.8μm. A second generation mask set design is provided, improvements on the n-i-n heterostructure aimed at achieving push-pull operation, and an alternative electrode configuration for improved electrical operation are discussed.

Chapter 2

Optical Signal Modulation

An optical carrier is described by its physical qualities - polarization, amplitude (A_0), phase (ϕ), and frequency (ω). The carrier is expressed as a time-varying electric field of the form

$$E(t) = \hat{e}A_0 cos(\omega_0 t - \phi_0) = Re[\hat{e}A_0 e^{i\phi_0} exp(-i\omega_0 t)] \tag{2.1}$$

where E is the electric field, Re represents the real part, $\hat{e}$ denotes a unit vector and the field polarization. Modulation of these elemental optical signal properties (amplitude, phase, frequency, and polarization) is the foundation of optical communication.

The electric field output of a Light Amplification by Stimulated Emission of Radiation device, or laser, is described by the expression in Equation 2.1, and can be either directly modulated or indirectly modified by external modulator devices. Direct modulation of a semiconductor diode laser is a common procedure that is inherently limited by the properties of the diode itself [25] and the current flow through it, resulting in center frequency shifting (chirping - the ratio of the change in refractive index Δn to the change of the extinction ratio Δk), reduced effective feedback levels, thermal effects and delays [26, 27], and spectral linewidth broadening. These concerns and others that are related to direct modulation present a formidable obstacle to reliable long-haul optical communication systems, limiting transmission speeds and distances [28].

External optical modulators [29] are an alternative to direct modulation, allowing the source to operate independently and improving the accuracy of the frequency control (by eliminating carrier induced frequency variation) and the output power control [30]. Despite the additional 5-7dB of insertion losses [31], external modulators are advantageous due to

their high operational speeds and high extinction ratio, allowing for data rates of up to 50Gb/s [32].

There are several basic types of modulation effects and hence external modulators. This chapter provides an overview of the prevalent electroabsorption and electrooptic effects and offers insight into their application in the construction of optical phase and amplitude modulators.

2.1 Physical Optical Modulation Effects

Materials are characterized by real and imaginary parts, which correspond to the refractive index and absorption coefficient. The refractive index, n, describes the decrease in the phase velocity of light that is traveling through a medium relative to light that is propagating in a vacuum. The absorption coefficient, α, dictates how far light can propagate before it is absorbed by the material. Both the refractive index and the absorption coefficient are wavelength dependent and are related through the Kramers-Kronig relation

$$n(\omega) = \frac{c}{\pi} \int_0^\infty \frac{\alpha(\omega')}{\omega'^2 - \omega^2} d\omega' \tag{2.2}$$

where c is the speed of light, ω is the frequency of interest, and ω' the frequencies over which integration is performed. The relationship clarifies that a modification of the absorption induces a change in the refractive index (or vice versa). Adjustments in the absorption coefficient are associated with amplitude modulation of an optical carrier, while changes in the phase, frequency, and polarization are correlated with the index of refraction.

The two classes of external modulators - absorption and electrooptic - are built upon the Kramers-Kronig relationship. Absorption-based modulators are typically small (on the order of microns in length), and utilize the strong tuning effect of an applied electric field on the absorption edge of quantum wells. Electrooptic modulators (longer devices due to the relatively weaker linear electrooptic coefficient) [28] exploit the electrooptic properties of compound semiconductor structures and their high indices of refraction to produce strong electric fields and efficient index change. While the following sections provide a basic overview of the physical modulation effects that are considered in this work, for completeness, please refer to the discussions in [2].

2.1.1 Absorption Effects

Electroabsorption modulators are key components in optical fiber communication systems. Their main strengths are the possibility of integration with other semiconductor photonic devices such as distributed feedback (DFB) [33] and distributed Bragg reflector (DBR) lasers, low cost [34], low chirp, high speed, and low driving voltages and small device dimensions.

Operation of electroabsorption modulators is based on the Franz-Keldysh effect and the principle that an applied electric field can shift the absorption spectrum and change the amount of light that is absorbed. This type of modulator is implemented with either bulk semiconductors or multiple quantum well (MQW)/quantum dot structures, typically using compound semiconductors. MQW and quantum dot structures apply the quantum-confined Stark effect (QCSE) to achieve a high modulation extinction ratio.

Broadband GaAs/$Al_xGa_{1-x}As$ modulators spanning wavelengths between 905nm and 960nm have been demonstrated using the Franz-Keldysh effect [35]. Despite this and other reported successes, the Franz-Keldysh effect is weak and is enhanced only by millimeter-scale devices and high driving voltages, relative to the stronger QCSE. Therefore, QCSE is the primary effect that is pursued in the design of modulators. Wood et al have demonstrated P-I-N, GaAs/$Al_xGa_{1-x}As$ multiple quantum well (MQW) absorption modulators operating at 860nm [36]. Tobin and Bruno [37] designed a GaAs/AlGaAs triple-quantum-well, P-I-N modulator structure that uses the QCSE for an application operating at 810nm. In this configuration, the coupling between multiple wells (composed of either GaAs or $Al_{0.06}Ga_{0.94}As$ and that are separated by very thin $Al_{0.3}Ga_{0.7}As$ layers) allows the photon transition energy to be tuned to the desired value. Jarrahi et al fabricated velocity-matched, traveling wave Mach-Zehnder modulators at 870nm with multiple $Al_xGa_{1-x}As$ quantum wells on a GaAs substrate. The device displayed a low driving voltage of 0.45V by incorporating both the QCSE and a resulting electro-refractive effect [38].

2.1.2 Linear Electrooptic Effect

The refractive index of a material that experiences a change due to an applied electric field is described by the following power series expansion

$$\Delta\left(\frac{1}{n^2}\right)_{ij} = r_{ijk}E_k + R_{ijkl}E_kE_l + ... \tag{2.3}$$

where E_k is the k^{th} component of the electric field, r_{ijk} is the linear electrooptic coefficient (describing a linear dependence on the applied electric field) and R_{ijkl} is the quadratic electrooptic coefficient. The electrooptic effect, also known as the Pockels effect, is represented by:

$$\begin{pmatrix} \Delta\frac{1}{n_x^2} \\ \Delta\frac{1}{n_y^2} \\ \Delta\frac{1}{n_z^2} \\ \Delta\frac{1}{n_{yz}^2} \\ \Delta\frac{1}{n_{xz}^2} \\ \Delta\frac{1}{n_{xy}^2} \end{pmatrix} = \begin{pmatrix} r_{11} & r_{12} & r_{13} \\ r_{21} & r_{22} & r_{23} \\ r_{31} & r_{32} & r_{33} \\ r_{41} & r_{42} & r_{43} \\ r_{51} & r_{52} & r_{53} \\ r_{61} & r_{62} & r_{63} \end{pmatrix} \begin{pmatrix} E_1 \\ E_2 \\ E_3 \end{pmatrix}$$

For GaAs, an isotropic cubic crystal with four-fold symmetry of group $\bar{4}3$ that lacks inversion symmetry, the electrooptic matrix reduces to

$$\begin{pmatrix} 0 & 0 & 0 \\ 0 & 0 & 0 \\ 0 & 0 & 0 \\ r_{41} & 0 & 0 \\ 0 & r_{52} & 0 \\ 0 & 0 & r_{63} \end{pmatrix}$$

where $r_{41} = r_{52} = r_{63}$ for isotropic materials. For example, a change, Δn, that is produced by a y-directed applied electric field is

$$\Delta\frac{1}{n_{xz}^2} = r_{52}E_y = r_{41}E_y \tag{2.4}$$

In a GaAs-based modulator, the applied electric field induces a change in the refractive index along perpendicular axes, i.e. E_y produces a response in the x and z-directed refractive

indices. However, the electric field also distorts the index ellipsoid from a circle in the xz plane to an ellipsoid rotated by 45^o off the xz plane. Hence, the applied electric field E_y results in modified $n_{x'}$ and $n_{z'}$ (the refractive indices in the x' and z' major axes of the index ellipsoid). An incoming beam that is directed along the z axis has a TE component along the x axis and a TM component along the y axis. The TE mode will be affected by the modified $n_{x'}$, while the TM mode lying on the same axis as the electric field, will not feel the effects of a Δn (consequently, the device's efficiency is reduced as only the TE mode of the beam undergoes modulation [39]). An optical wave propagating along the z' axis and polarized in the x' direction will have the following expression for the change in the index of refraction:

$$\Delta n_{x'} = \frac{1}{2} r_{41} n^3 E_y \tag{2.5}$$

Alternately, an optical wave propagating along the x' axis and polarized in the z' direction will have a change in the index of refraction similarly determined by

$$\Delta n_{z'} = \frac{1}{2} r_{41} n^3 E_y \tag{2.6}$$

The linear electrooptic effect further describes the effects of an applied electric field on the phase of an optical carrier. The total phase shift of a beam traveling along the z axis, that is induced by an electric field that is applied along the y axis, is given by

$$\Delta\phi = k_0 L \Delta n = \frac{2\pi}{\lambda} \frac{L n^3 r_{41} E_y}{2} \tag{2.7}$$

where k_0 is a wavevector equal to $\frac{2\pi}{\lambda}$, L is the modulator length, r_{41} is the y-axis electrooptic coefficient (typically on the order of $1 \cdot 10^{-12}$m/V [30, 40] and varies little with composition and wavelength [41]) and λ is the wavelength of operation. The relationship between the applied voltage and the corresponding electric field is expressed as

$$V = E_y \cdot t_g \tag{2.8}$$

where t_g is the thickness of the active region of the modulator. Therefore, the relationship

between the applied voltage and the phase shift is given by

$$\Delta\phi = \frac{\pi}{\lambda}\frac{Ln^3 r_{41} V}{t_g} \tag{2.9}$$

The phase shift that is shown in Equation 2.9 is an important concept of optical interference, which is illustrated in Figure 2-1. If the crests (or troughs) of two waves meet at the same time and are superimposed, they will combine constructively to form a wave with a magnitude equal to the sum of the individual amplitudes of the two waves (top image). The principle of constructive interference occurs when the difference in phase between the two waves with the same magnitude is an integer multiple of 2π. When the phase difference between the same waves is an odd integer multiple of π (i.e., 3π, 5π, etc.), the crest of one wave will meet the trough of the other wave at the same time. In this scenario, the waves will destructively interfere, and the magnitude of the combined wave will be equal to the difference in amplitude between the two waves (bottom image). In modulators that are based on principles of optical interference, a phase shift of $\phi = \pi$ between two optical signals of equal magnitude yields signal extinction, and requires an applied voltage known as V_π, described by

$$V_\pi = \lambda\frac{t_g}{Ln^3 r_{41}} \tag{2.10}$$

An early example of a modulator that is based on the linear electrooptic, or Pockels, effect is a double heterostructure GaAs/$Al_xGa_{1-x}As$ design [42] and demonstrated a drive voltage of 10V over the 1mm-long device (at λ=1.153μm). The Pockels effect is described as weak in bulk modulators that are composed of III-V materials (i.e. GaAs [40]). Accordingly, these devices require higher applied voltages to achieve signal extinction. In contrast, multiple quantum well (MQW) heterostructures exploit an electrooptic effect with a quadratic dependence on the electric field intensity (i.e. Kerr effect) to construct shorter and lower voltage-length (VL) modulator devices than those created with bulk materials and the corresponding Pockels effect. Despite these benefits, MQW modulators which suffer from higher propagation losses [43] relative to bulk semiconductor devices, typically produce small changes in the refractive index [44], and are limited to narrow operational wavelength and temperature ranges.

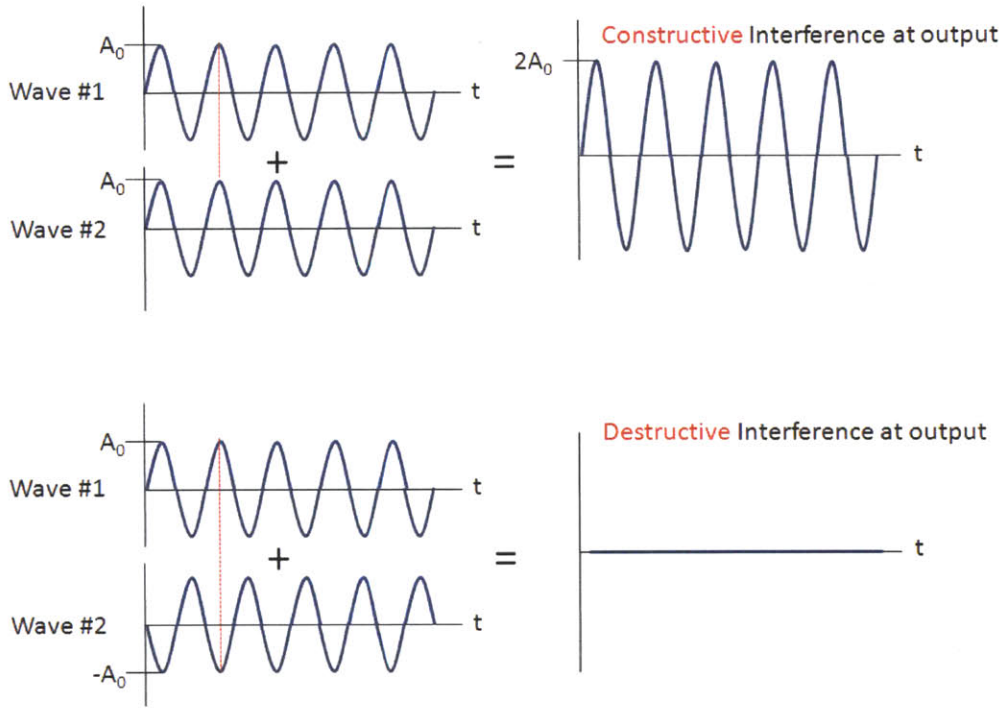

Figure 2-1: Superposition of waves resulting in constructive or destructive interference. The combination of two waves of equal phase and amplitude, A_0, results in constructive interference at the output (top figure). The combination of two waves of equal amplitude but with a relative phase retardation of 180^o between them yields destructive interference of the signals at the output and complete signal extinction (bottom figure).

2.2 Amplitude Modulators

Electrically-induced index or absorption changes in guiding materials are the basis of amplitude modulation. The phase modulation resulting from the varied refractive index is translated into amplitude modulation through devices such as directional couplers and Mach-Zehnder Interferometers that are described in the following sections. For more information on a variety of modulation devices, please consult the works of Dagli [28], Dakin and Brown [30], and Saleh [45].

2.2.1 Directional Coupler

Directional couplers are the building blocks of both optical waveguide switches and intensity modulators. While this section covers the relevant theory on the operation of directional couplers as modulators, information on coupled-mode theory is available in [46, 47, 48].

The directional coupler consists of two parallel waveguides (A and B) in close proximity to each other over a length of L, allowing for evanescent coupling to occur between the waveguides. Optical coupling is controlled by two variables:

1. The coupling coefficient κ, which is adjusted by the application of an electric field over the waveguides which instigates a change in the wavelength and waveguide dimensions, as well as in the refractive index of the propagating mode. The coupling coefficient is related to L, the length at which the optical power shifts completely from one waveguide to the other, by

$$\kappa L = \pi/2 \tag{2.11}$$

2. $\Delta\beta$, the mismatch between the propagation constants of both waveguides [45].

The fundamental mode propagation constant, β, represents the variance in the electromagnetic wave amplitude as it propagates in space, and is defined as the wavenumber multiplied by the refractive index of the waveguide within which it travels, or

$$\beta = n\frac{2\pi}{\lambda_0} \tag{2.12}$$

$\Delta\beta$, the propagation mode mismatch which in turn is designated as

$$\Delta\beta = \beta_1 - \beta_2 = \Delta n\frac{2\pi}{\lambda_0} \tag{2.13}$$

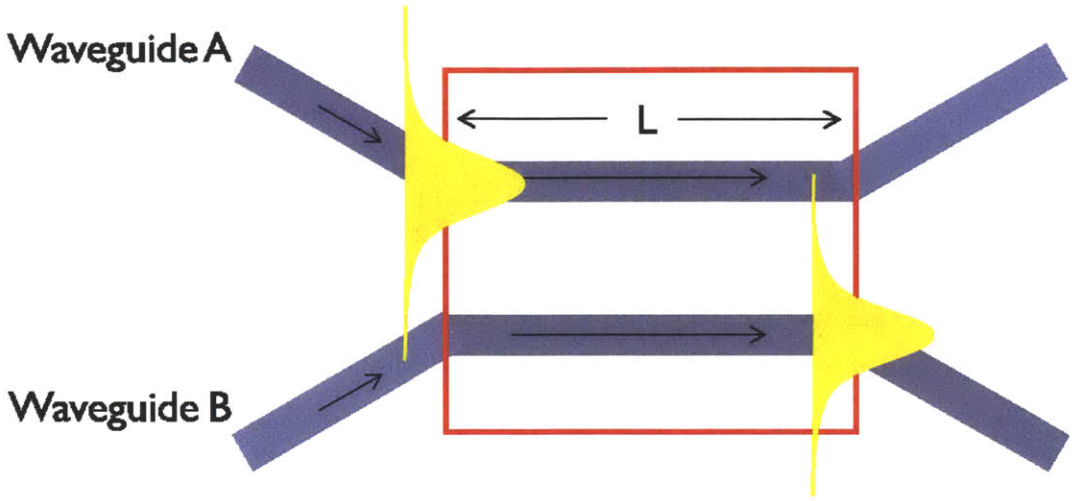

Figure 2-2: The directional coupler consists of two parallel waveguides (A and B) in close proximity to each other over a length of L, allowing for evanescent coupling to occur between the waveguides.

where β_1 and β_2 are the propagation constants corresponding to the two waveguides, and Δn is the difference between their respective indices of refraction. If $\Delta\beta$=0 (the waveguides are equivalent physically) and only one of the waveguides is excited at the input so that A(0)=A_i and B(0)=0, the power from waveguide A will transfer fully to B at the coupling length, L.

To construct a modulator with a directional coupler, the electrodes are positioned over (and parallel to) the waveguides within the coupling region. The electric field that is produced by an applied voltage changes the refractive index and consequently the coupling ratio. A change in the refractive index, n, in response to a time varying external voltage, v(t), is expressed as

$$n(t) = n_0 + \Delta n = n_0 + Kv(t) \tag{2.14}$$

where K is a proportionality constant set by the geometry, the physical effect and the material. Under external perturbation, the effect on the refractive index as described in Equation 2.14 combines with the expression for the propagation constant in Equation 2.12 to produce a β_1 and β_2 of

$$\beta_1 = n_1(t)\frac{2\pi}{\lambda_0} = \beta_0 + \Delta\beta_1 = \frac{2\pi}{\lambda_0}(n_0 + K_1V(t)) \tag{2.15}$$

$$\beta_2 = n_2(t)\frac{2\pi}{\lambda_0} = \beta_0 + \Delta\beta_2 = \frac{2\pi}{\lambda_0}(n_0 + K_2 V(t)) \tag{2.16}$$

The power transfer between the two waveguide is expressed as the ratio, T:

$$T = \frac{P_B(z=L)}{P_A(z=0)} = \left(\frac{\pi}{2}\right)^2 sinc^2\left[\frac{1}{2}\sqrt{\left(1+\left(\frac{\Delta\beta L}{\pi}\right)^2\right)}\right] \tag{2.17}$$

The transfer function is not periodic, and has a maximum for $\Delta\beta$L = 0 and a null for $\Delta\beta$L = $\sqrt{3}\pi$. To switch the modulator from the on state to the off state, a switching voltage, or V_s, is applied. The directional coupler is most often implemented as a switch device, but has also been employed in unison with physical effects to produce intensity modulators. For instance, Khan et al designed an electrooptic directional coupler modulator at λ=0.8μm with propagation losses of 3.4dB/cm [49]. The 3.5mm-long $Al_xGa_{1-x}As$/GaAs ridge waveguide modulator had a corresponding drive voltage of 2V. The ridge design confined the optical mode, allowing a high overlap between the optical and electrical modes and reducing the required applied voltage.

2.2.2 Mach-Zehnder Interferometer

Interferometric devices apply the principle of interference to perform relative measurements. The Mach-Zehnder Interferometer (MZI), that was developed by Ludwig Mach and Ludwig Zehnder, measures the relative phase shift between two optical signals propagating within its two arms [50, 51]. In the MZI, which is shown in Figure 2-3, an input optical wave from

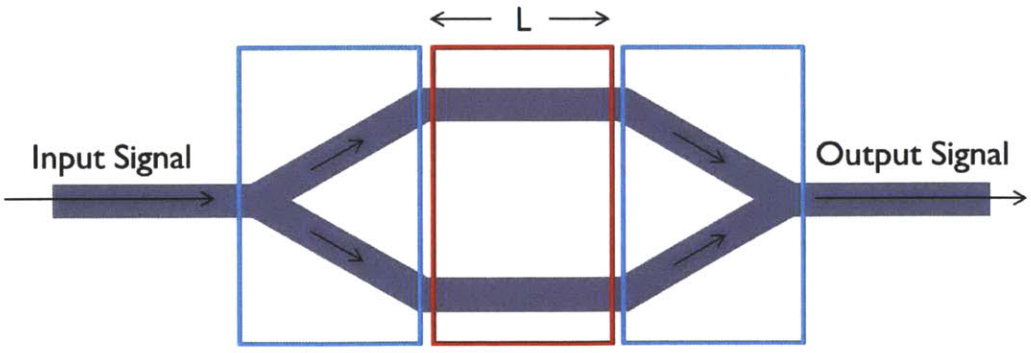

Figure 2-3: The MZI structure is composed of input and output waveguides, Y-junctions (within blue boundary) that split and recombine optical power, and Interferometer arms (within red boundary) of length L.

a coherent optical source is divided equally into two paths (in this case, using a Y-junction device). The split wave propagates through the arms of the interferometer and recombines at a second Y-junction at the opposite end of the arms. At the output of the second Y-junction, the recombined wave - a result of interference - is coupled into a waveguide through which the beam propagates to the device output.

Ideally, the power split to each arm at the Y-junction is equal to half the original power, and is expressed as the power splitting ratio, s^2. However, device processing is often inaccurate and results in uneven pathways. The resulting formula for s^2 includes a factor of ξ that considers fabrication errors that may affect the power split:

$$s^2 = \frac{1}{2} + \xi \tag{2.18}$$

The interferometer arms of the MZI are independent phase modulators of length L, each with propagation constants (β_1 and β_2) associated with their propagating modes, and phase shifts (φ_1 and φ_2) that are in response to the applied electric field. The result of the recombination of phase modulated optical waves is an output signal that has its amplitude modulated relative to the input.

There are two states for the MZI modulator - on and off. When the interferometer arms and the paths traversed by the split optical beams are identical, that is,

$$\beta_1 L = \beta_2 L \tag{2.19}$$

there is constructive interference at the modulator output. As exhibited in Figure 2-4(a), when no voltage is applied to either of the arms, a system that had a single mode signal as the input will similarly output a single mode. However, if the voltage equivalent to V_π is applied to one of the interferometer arms [see Figure 2-4(b)], the phase of the optical signal will shift 180^o relative to the phase of the signal propagating in the other arm, such that

$$(\beta_1 - \beta_2)L = \pi \tag{2.20}$$

At the output, the signals recombine and interfere destructively. As the two beams interfere along the length of the output waveguide, a higher mode with a null in the center is excited. This mode radiates out if the waveguide is single mode, and only if the path is long enough

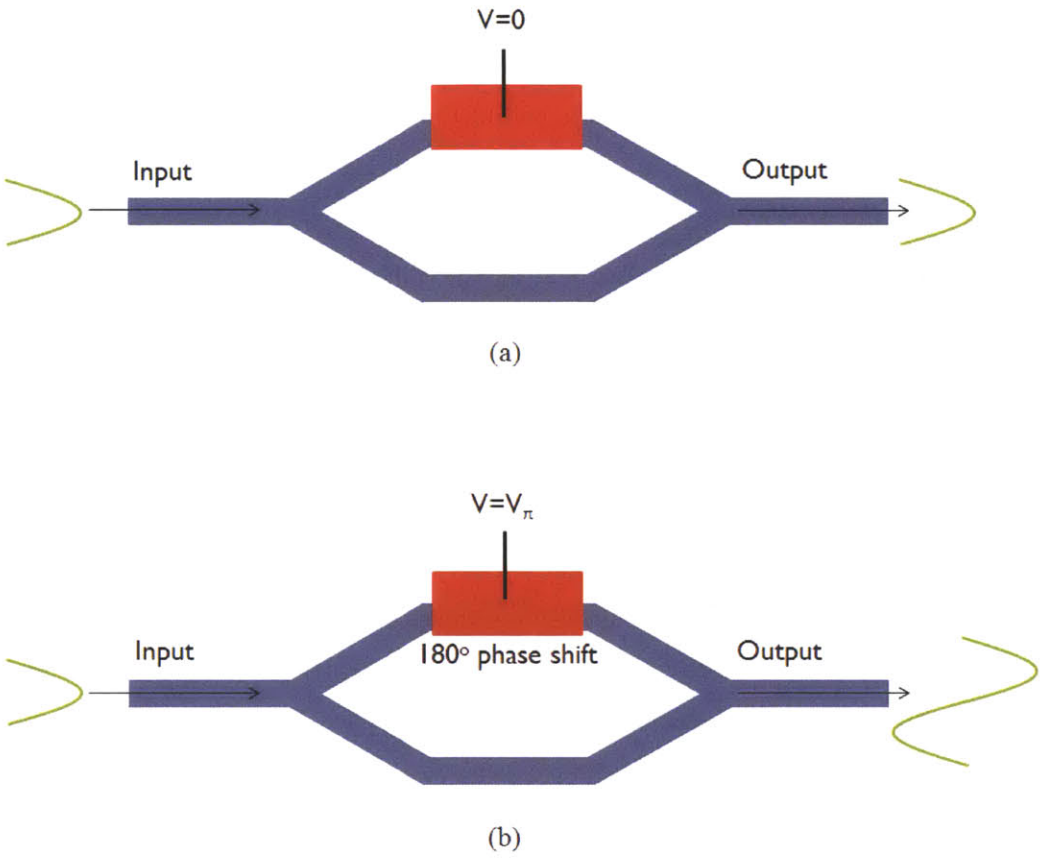

Figure 2-4: The Mach-Zehnder Interferometer (MZI) modulator at the on (a) and off (b) states. For a single mode launched into the modulator input - (a) If no voltage is applied along either arm of the interferometer, there is no difference in phase between the divided optical signals traveling along each arm, and the output signal is a fundamental mode. (b) If a voltage equivalent to V_π is applied to one of the arms, the signal is phase shifted 180^o relative to the other arm and the carriers interfere destructively. If the waveguides support higher order modes, the fundamental mode will be converted to higher order modes at the output.

for the mode to completely radiate away. If the waveguide is not sufficiently long, there will be power present at the output. If the waveguide is not single mode, the fundamental mode will be converted to higher order modes at the output [30].

The amplitude of an optical mode propagating along the z-direction within a waveguide

is generally defined as

$$A(z) = A_0 e^{-j\beta z} \tag{2.21}$$

The amplitude at the MZI output (A_o) is expressed relative to the optical amplitude at the input (A_i) of the MZI as

$$A_o = A_i[s^2 e^{-j(\beta_1 L + 2\varphi_1)} + (1 - s^2)e^{-j(\beta_2 L + 2\varphi_2)}] \tag{2.22}$$

Setting s^2 to its value from Equation 2.18, the output amplitude can be further developed into [30]

$$A_o = A_i[cos(\gamma) - 2j\xi sin(\gamma)]e^{-j\left[\left(\frac{\beta_1+\beta_2}{2}\right)L + (\varphi_1+\varphi_2)\right]} \tag{2.23}$$

where γ is equal to

$$\gamma = \left[\left(\frac{\beta_1 - \beta_2}{2}\right)L + (\varphi_1 - \varphi_2)\right] \tag{2.24}$$

If the pathways are equal such that there is no phase shift between the interferometer arms and the fabrication is ideal (yielding a one-half power split) then Equations 2.15, 2.16, 2.23, and 2.24 simplify to

$$A_o = A_i cos\left(\frac{\pi}{\lambda_0}(K_1 - K_2)LV(t)\right) \tag{2.25}$$

and can be further expressed as a transfer function

$$\frac{|A_o|^2}{|A_i|^2} = cos^2\left(\frac{\pi}{\lambda_0}(K_1 - K_2)LV(t)\right) \tag{2.26}$$

In contrast with the directional coupler modulator, the transfer function of the Mach-Zehnder interferometer modulator is periodic. The voltage that is applied to switch the modulator from the on state to the off state, V_π (explained in Section 2.1.2), is

$$V_{\pi,MZI} = \frac{\lambda_0}{2(K_1 - K_2)L} \tag{2.27}$$

2.3 Summary

Despite the demonstrations of modulators performing in the vicinity of λ=0.8μm, the main limitation of absorption-based modulators within the scope of this work lies in the optical bandwidth capability. Electroabsorption modulators are impeded by the ability to shift the absorption edge sufficiently to form "ultra-broadband" operation over a Ti-Sapphire octave. For an acceptable level of modulation sensitivity, the optical source must be matched to within 40nm of the absorption edge of the structure [52]; therefore, electroabsorption modulators are not appropriate for the purpose of optical arbitrary waveform generation. Moreover, electroabsorption modulators exhibit a tradeoff between drive voltages and insertion losses and are temperature-sensitive (temperature changes affect the material bandgap and shift the absorption edge). Modulators operating on the quadratic electrooptic effect are at a similar disadvantage. The strengths and shortcomings of the mentioned physical effects, summarized in Table 2.1, suggest that for the purposes of an external ultra-broadband modulator with a low voltage, the appropriate design choice is based on the linear electrooptic effect.

Though directional couplers can theoretically provide the same degree of linearity and bandwidth operation as Mach-Zehnder Interferometer-based modulators, their design and fabrication presents a greater difficulty [52], particularly due to the strong performance dependence on the dimensions of the gap between the waveguides in the coupling region and the long interaction lengths (i.e., Alferness et al fabricated a directional coupler switch/modulator at λ=1.32μm with a switching voltage of 4.5V and dimensions of L=14.5mm and a gap of 6.5μm [53]). While directional couplers are preferred for switching purposes, the Mach-Zehnder interferometer configuration is favored as modulator devices.

For the most efficient systems, form must fit the function. For the reasons that are detailed above, and the specified broadband requirement, this work showcases the design of a ridge-waveguide Mach-Zehnder modulator operating on the electrooptic Pockels effect.

Table 2.1: Summary of the benefits and disadvantages of physical modulation effects

Physical Effect	Benefits	Disadvantages
Electroabsorption	Strong effect; shorter device	Limited wavelength, temperature range; tradeoff between insertion losses and drive voltages
Linear Electrooptic (Pockels)	Broadband wavelength capability	Weak effect; longer devices
Quadratic Electrooptic (Kerr)	Strong effect; shorter devices	Limited wavelength, temperature ranges; high propagation losses

Chapter 3

Design and Simulation of the Modulator Device

Integration of optical devices functioning at λ=1.55μm has been driven by the availability of reliable, high-speed modulators that are based on lithium niobate, silicon, or indium phosphide materials. Optical Arbitrary Waveform Generation (OAWG) initiatives at this wavelength are now focused on achieving stable optical comb generators and on-chip integration. The availability of Ti:Sapphire lasers operating at λ=0.8μm prompts the development of complementary modulators based on III-V semiconductor materials lattice-matched to GaAs. This chapter provides insight to past work that has been accomplished in the field as well as research undertaken by the author (see [2]), and examines considerations of material and device design elements to provide an understanding of the development of a broadband modulator.

3.1 Motivation

Modulators are characterized by a set of parameters listed below. These criteria qualify the performance of the modulator, and play a major role in the conception and characterization.

1. Insertion losses (or optical power loss) are measured in decibels and describe the total losses that are present in a system. The insertion loss is defined by the ratio of the maximal output power (the on-state of the modulator) to the input power that is

coupled into the modulator, or

$$\frac{P_{out,Max}}{P_{in}} \tag{3.1}$$

2. Extinction, or contrast ratio, is defined as the ratio of the minimum output power (in the off-state) to the maximal output power (on-state) in decibels. The extinction ratio is given by

$$10log\frac{P_{out,Min}}{P_{out,Max}} \tag{3.2}$$

3. Drive voltage (V_π) is defined as the voltage that is required to turn the modulator off, such that $P_{out} = P_{out,Min}$

4. The 3dB bandwidth, Δf, determined by device capacitance under reverse bias conditions. In long waveguides, the bandwidth is limited by the transit time, τ, of the light through the waveguide and the bandwidth is described by [28]

$$\Delta f = 1.39\pi\tau = \frac{1.39c_0}{\pi n_g L} \tag{3.3}$$

where n_g is the waveguide index of refraction and L is the device length. This property is increasingly more important as fiber optic communications rely on wider bandwidths [48].

5. Polarization Dependence is defined by either transverse electric or transverse magnetic operation.

6. Figure of merit, F, describes the overall performance of the device and is defined by

$$F = \frac{\Delta f \lambda}{V_\pi} \tag{3.4}$$

The following subsections describe the motivations for the modulator epitaxial structures that are introduced later in this chapter. First, the sources of attenuation (an important modulator specification which limits the waveguide structure, dimensions, and materials) are examined and methods of circumventing or minimizing these are offered. III-V material theory will be briefly covered, followed by a fundamental overview of the parameters considered in selecting modulator materials. Finally, related research in the field and reported performance metrics associated with modulator configurations and physical effects will be

discussed, in order to motivate the designs, simulations, and measurements that will be presented in later sections of this work.

3.1.1 Losses in Semiconductor Waveguides

Several mechanisms of waveguide loss drive the heterostructure design and fabrication, namely [54] (1) coupling losses due to mode mismatch, (2) Fresnel reflection losses, (3) propagation losses due to scattering, (4) material absorption losses, (5) radiation losses (typically seen in curved waveguides), and (6) free-carrier absorption losses. A number of these losses deal specifically with fiber-to-chip light transmission (i.e. coupling and fresnel losses that can be controlled with lensed fibers or anti-reflection coatings), while the other losses can be mitigated by careful design and fabrication of the semiconductor heterostructure.

There are two sources of scattering losses - volume scattering that is caused by imperfections or crystalline defects, and surface scattering. Volume scattering is strongly dependent on the dimensions of the imperfections, and is an unlikely concern with optimized molecular beam epitaxy growth conditions. In-plane surface scattering is slightly more significant, as propagating light beams and higher order modes in particular interact continuously with the waveguide surfaces. Fabrication processes also greatly contribute to optical losses (i.e. radiation losses), and their role in modulator performance will be discussed further in Section 3.2.3 of this chapter.

High quality control of deposition thicknesses on the order of angstroms to nanometers during growth of thin semiconductor films has for the most part eliminated concern of surface scattering [26]. While scattering losses dominate in dielectric and amorphous thin films, scattering in semiconductor films is negligible in comparison to absorption losses.

Two kinds of processes are responsible for absorption losses - interband and free-carrier absorption. In interband absorption, photons with an energy that is greater than the bandgap energy of the semiconductor are absorbed, in the process promoting an electron from the valence to the conduction band. The interband absorption effect can be averted by choosing a photon wavelength λ_{light} (wavelength of the light traveling within a waveguide) that is longer than the absorption edge wavelength of the waveguide semiconductor material λ_{edge}. That is,

$$\lambda_{light} > \lambda_{edge} \tag{3.5}$$

In free-carrier absorption, photons are absorbed and their energy is used to promote electrons that are already at the conduction band to higher energy states. Free-carrier absorption is expressed by

$$\alpha_{fc} = \frac{Ne^3}{(m*)^2 n\epsilon_0 \omega^2 \mu c} \tag{3.6}$$

where the free-carrier absorption coefficient α_{fc} is related to N, the free-carrier concentration per cm^{-3}, the dielectric constant ϵ, the mobility μ, the speed of light c, the electron charge e, the effective electron mass m*=0.8·electron mass, and

$$\omega = 2\pi\upsilon \tag{3.7}$$

where υ is frequency. In heavily doped, $N > 10^{18} cm^{-3}$ GaAs devices, free-carrier absorption contributes losses of 1-10 db/cm. This figure can be minimized by discouraging interaction between the optical mode and available free carriers.

3.1.2 The III-V Material System

The III-V material system that is shown in Figure 3-1 [55], consists of binary crystals (i.e. GaAs and InP), engineered ternary compounds (such as $Al_xGa_{1-x}As$ and $In_xGa_{1-x}P$) and quaternary compounds (for instance, $In_xGa_{1-x}Al_yAs_{1-y}$). By combining binary, ternary, and quaternary compound semiconductors, heterosructures can be deposited onto common substrate surfaces such as GaAs or InP. The lattice constants of common substrates is represented in Figure 3-1 by dashed lines. While mismatched materials can be grown, resulting heterostructures contain misfit dislocations that degrade the epitaxial formation electrically and structurally. Consequently, lattice-matched structures with composites such as GaAs and AlAs, or InP and GaP are preferred in devices of electronic purpose. The flexibility afforded by the many possible combinations of materials and the direct bandgap of III-V crystals make these semiconductors a popular choice in optoelectronic applications.

The broadband modulator in this work is tailored to guide a spectrum of signals with wavelengths centered at 800nm, the wavelength at which the peak gain of the Ti:Sapphire laser is observed. The bandgap energy, E, associated with a crystal dictates those wavelengths for which the material is transparent, and those wavelengths that the material

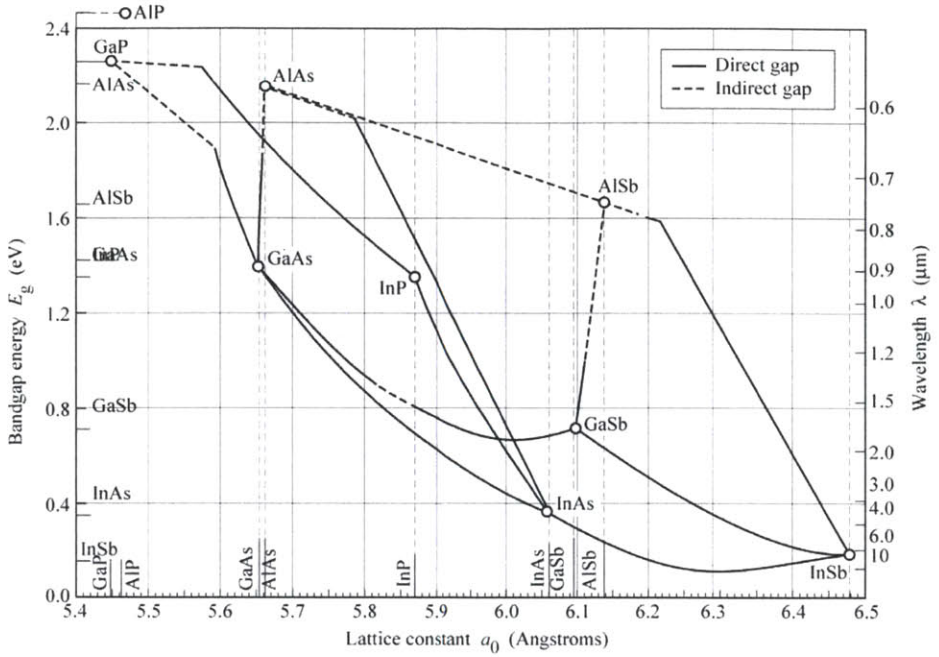

Figure 3-1: Common semiconductor materials in the III-V group and associated bandgap energies, lattice constants and emission wavelengths [55]. The black lines that connect the binary, direct bandgap crystals are associated with ternary compounds, and enclose areas of quaternary compounds.

absorbs through the relationship

$$E = h\upsilon = \frac{hc}{\lambda} \tag{3.8}$$

where h represents Planck's constant and c is the speed of light. In general, materials of the III-V system absorb wavelengths in the visible range and are transparent in the infrared light spectral range. Equation 3.8 indicates that a bandgap energy of around 1.5eV is required for a system that is transparent to 0.8μm wavelength of light. $Al_xGa_{1-x}As$ and $In_xGa_{1-x}P$ materials lattice-matched to GaAs are appropriate waveguiding choices for a broadband system supporting wavelengths of light that are both shorter and longer than λ=0.8μm.

3.1.3 Fundamentals of Modulator Heterostructure Design

Figure 3-2 provides an overview of the general design considerations of the modulator heterostructure. The structure consists of six fundamental components (listed from the bottom

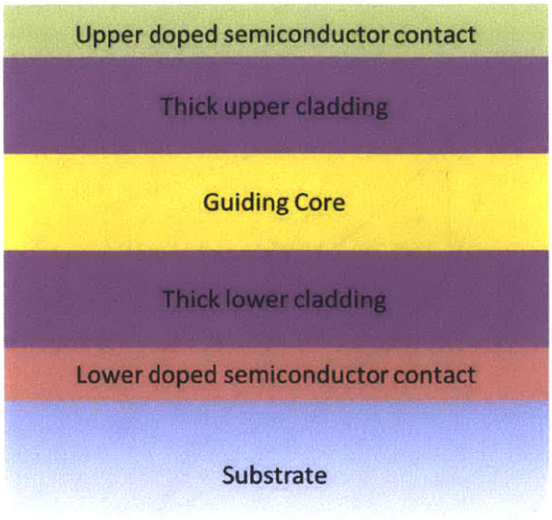

Figure 3-2: Elementary schematic of an optical modulator epitaxial heterostructure. The device structure consists of a substrate, thick upper and lower cladding layers, a core (or active region) in which the optical mode is guided, and upper and lower doped semiconductor contact layers.

layer to top):

1. The substrate
2. Doped lower contacting semiconductor layer
3. Thick lower cladding
4. A guiding core supporting optical mode propagation
5. Thick upper cladding
6. Doped upper contacting semiconductor layer

The GaAs substrate absorbs all wavelengths shorter than 870 nm (see Figure 3-1). If the incoming mode couples into the substrate, the light will certainly be absorbed into the substrate and all power will be lost. Therefore, a thick lower cladding layer, transparent to the wavelengths in the desired optical bandwidth, is imperative for mode isolation. The index of refraction of the guiding layer should be higher relative to surrounding layers in order to confine the optical mode. However the index of refraction of the device active region and surrounding cladding layers should also be as similar as possible in order to minimize

fiber-to-waveguide coupling loss, maximize mode size while still maintaining single-mode operation.

The lower and upper cladding layers prevent interaction between the optical mode in the guiding core and the carriers in the doped semiconductor layer above and below the lower and upper cladding layers, respectively. By increasing the thickness of the upper and lower cladding layers, the overlap between the optical mode and doped regions is minimized and the optical loss due to free-carrier absorption is reduced.

The upper and lower doped contact layers provide a higher carrier concentration that leads to reduced contact resistance and good ohmic contact to the metal contacts that are evaporated on top of, and on the bottom of, the heterostructure. Creating p-i-n, n-i-n, or p-i-p heterostructure configurations is achieved by doping both contact layers with either p- or n-type dopants. The doping structure of the modulator determines aspects of its performance, including device loss, and reverse and forward bias operation.

A set of requirements for the waveguide modulator can be developed from the above discussion. The device should:

- Exhibit low insertion and optical losses
- Support a single optical mode in its guiding core
- Display strong mode confinement
- Operate on low driving voltages

3.1.4 Related Work in III-V-Based Semiconductor Optical Modulators

The p-i-n configuration is common in Mach-Zehnder optical modulators. Landmark work and extensive efforts by Spickermann [56], Sakamoto [57], Dagli [58, 59] and many others [60, 61, 62, 63] have yielded a variety of GaAs/$Al_xGa_{1-x}As$-based modulators. Figure 3-3 summarizes some of the research that has been done on p-i-n optical modulators. The table is not all encompassing, but provides a view of the research landscape and technological progress. Modulation at λ=0.8μm has been accomplished primarily by devices operating on absorption-based effects such as QCSE and the Kerr effect rather than on Pockels-based modulators.

Optical propagation losses are often due to doping levels, and loss increases with concentration of p-type dopants in particular. P-type materials are also characterized by lower

Authors	Material	Effect	Device/ Operation	Wavelength (μm)	Voltage-Length (V-cm)/ Extinction Ratio	Losses (dB/mm)
Cites et al, Lightwave Tech., 12(7) 1992	MQW – GaAs/AlGaAs p-i-n	Kerr Effect	Mach Zehnder;	0.86-0.895	0.3V-cm; 23.8dB extinction	-2.3
Rolland et al, Elec. Lett., 1993	MQW – InP/InGaAsP p-i-n	Electro-absorption	Mach Zehnder; Push-pull	1.56	0.27V-cm; 18.6dB extinction	-8.7
Khan et al, Appl. Phys. Lett., 62, 1993	Bulk – GaAs/AlGaAs p-i-n	Pockels Effect	Directional coupler; ridge waveguide	0.83	0.7V-cm; 13dB extinction	-0.34
Sakamoto et al, Photonics Tech. Lett., 11(10), 1999	Bulk – GaAs/AlGaAs	Pockels Effect	Substrate removed; Mach Zehnder; Push-pull	1.55	8.7V-cm; NA	-0.35
Juodawlkis et. Al, 2003	MQW – InP/InGaAsP p-i-n	Kerr Effect	Mach Zehnder; Push-pull	1.55	0.9V-cm; 14dB extinction	-0.7
Dagli et al, Photonics Tech. Lett., 18(21),2006	Bulk – GaAs/AlGaAs	Pockels Effect	Mach Zehnder; Push-pull	1.55	3.7V-cm; NA	-0.29
Akiyama et al, Lightwave Tech., 26(5), 2008	MQW – InP/InGaAsP p-i-n	Kerr Effect	Mach Zehnder;	1.535	0.24V-cm; 3V-mm/ 14dB extinction	-0.77 to -0.9
Jarrahi et al, Photonics Tech. Lett., 20(7), 2008	MQW – AlGaAs/GaAs p-i-n	Electro-absorption; QCSE	Mach Zehnder;	0.87	0.0675V-cm; 10dB extinction	-0.56
Shin et al, Appl. Phys. Lett., 92, 2008	MQW – AlGaAs/GaAs p-i-n	Kerr Effect	Substrate removed; Mach Zehnder; Push-pull	1.55	0.42V-mm; 3dB extinction	-0.8

Figure 3-3: Summary of reported research on $GaAs/Al_xGa_{1-x}As$ p-i-n optical modulators.

conductivity and higher microwave losses, such that p-i-n devices suffer from optical and electrical losses that are attributed to the p-type cladding. Adopting the n-type dopants

in place of p-type reduces the aforementioned losses and provides higher conductivity for low-loss ohmic contacts [28].

n-i-n traveling-wave Mach-Zehnder Interferometer modulators employ upper and lower n-type cladding layers and eradicate losses caused by p-type materials. InP-based devices produce strong electric fields with low driving voltages [64, 65], and have exhibited 40- and 10-Gb/s large signal operation with peak-to-peak driving voltages of 3.0 and 1.2V, respectively. The MZ p-i-n and n-i-n configurations that are modeled on a Metal Oxide Semiconductor (MOS) structure, also enable push-pull operation with the added benefits of reducing the drive voltage and allowing high-speed chirp adjustment [58, 59]. Research efforts associated with the n-i-n configuration of modulators has been relatively recent, yielding promising results (see Figure 3-4), and encouraging further exploration.

Authors	Material	Effect	Device/ Operation	Wavelength (μm)	Voltage (V); Extinction Ratio	Losses (dB/mm)
Tsuzuki et al, Elec. Lett., 2003	MQW – InGaAlAs/ InAlAs n-i-n	Kerr Effect	Mach Zehnder;	1.55	2.2V (3mm-long); 20dB extinction	N/A
Tsuzuki et al, Photonics Tech. Lett., 2005	MQW – InGaAlAs/ InAlAs n-i-n	Kerr Effect	Mach Zehnder; Push-pull	1.55	1.2V (3mm-long) push-pull; 20dB extinction	N/A

Figure 3-4: Summary of reported research on GaAs/$Al_xGa_{1-x}As$ n-i-n optical modulators.

3.2 p-i-n, Arsenide-Based Heterostructure

The limitations, requirements and structural guidelines that are presented in Section 3.1.3 inspired the development of an arsenide-based, Pockels effect modulator with a p-i-n heterostructure configuration. The molecular beam epitaxy-grown (MBE) structure, shown in Figure 3-6, consists of an intrinsic dilute core of lattice-matched low index 150nm-thick $Al_{0.8}Ga_{0.2}As$ and high index 25nm-thick $In_{0.53}Ga_{0.47}P$ layers that both confines and max-

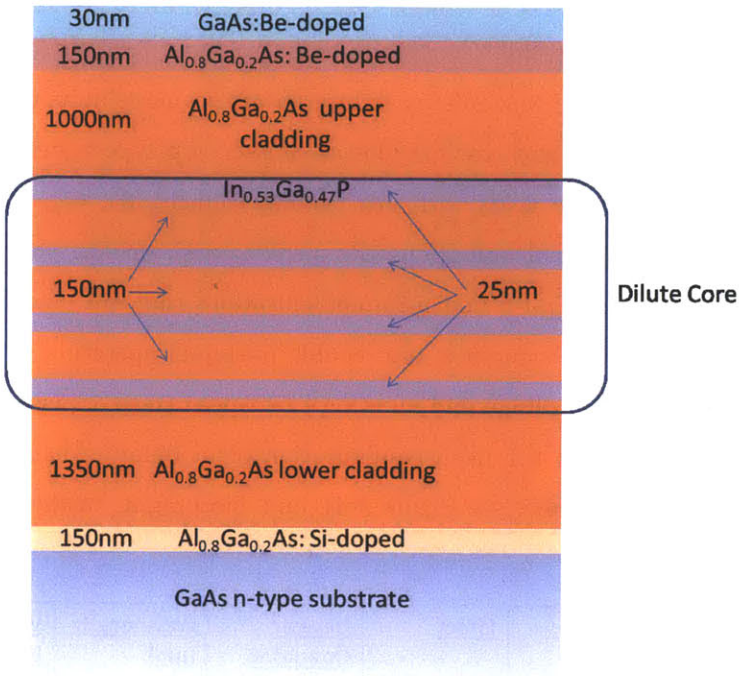

Figure 3-5: The p-i-n As-based modulator heterostructure design. The structure consists of a dilute core comprised of thin alternating $Al_{0.8}Ga_{0.2}As$ and $In_{0.53}Ga_{0.47}P$ layers, thick upper and lower cladding, and p- and n-type top and bottom contacts, respectively.

imizes the optical mode's dimensions. By embedding thin layers of high index material within a material of lower refractive index, an active region with an overall slightly higher effective index (determined by the spacing between high index layers) than that of the cladding layers is constructed. The effective index of the structure is close enough to that of the cladding layers so that low coupling loss is achieved, but high enough to keep the mode centered in the active region.

Thick 1μm upper and 1.35μm lower cladding layers separate the mode from the top $10^{17}cm^{-3}$, Be-doped (p-type) $Al_{0.8}Ga_{0.2}As$ and GaAs capping layer (to protect the $Al_{0.8}Ga_{0.2}As$ from oxidation), and from the bottom $10^{18}cm^{-3}$ Si-doped (n-type) $Al_{0.8}Ga_{0.2}As$, as well as from the absorbing $10^{18}cm^{-3}$, Si-doped GaAs substrate. The refractive indices of aforementioned materials at λ=0.8μm are available in Table 3.1 [66].

Although the use of $Al_xGa_{1-x}As$ as a cladding material minimizes the issue of lattice-matching to the GaAs substrate, the high Al content presents a growth difficulty due to

Table 3.1: Refractive indices of materials in the arsenide-based, p-i-n modulator heterostructure that is designed to operate at λ=0.8μm.

Material	Index at 0.8μm
GaAs	3.664
$Al_{0.8}Ga_{0.2}As$	3.14
$In_{0.53}Ga_{0.47}P$	3.32

the low Al adatom mobility on the surface during epitaxial growth. Grown epitaxial heterostructures have shown weak photoluminescence (PL) emission at λ=0.65μm due to the $In_{0.53}Ga_{0.47}P$ layers. The $Al_{0.8}Ga_{0.2}As$ is an indirect bandgap material and therefore, does not emit. The contribution of the $In_{0.53}Ga_{0.47}P$ material endows this structure with a very large optical bandwidth starting at 0.65μm and continuing into the infrared spectrum.

3.2.1 Design of the Modulator Ridge Waveguide

The heterostructure introduced in Section 3.2 is the foundation for the ridge waveguide optical modulator structure that is shown in Figure 3-6. By etching through the top Be-doped contact layers and dilute core, a 2μm-wide ridge that extends into the lower cladding layer is created, confining the optical mode horizontally. A wider ridge minimizes the interaction of the mode with the etched sidewalls and reduces the optical losses. However, a ridge too wide introduces unwanted higher modes. Beam propagation simulations have determined a 2μm-wide ridge structure to be the widest structure that solely supports first-order modes.

The RSoft BeamPROP-simulated [67] TE and TM mode profiles and the associated calculated indices for the deep-etched p-i-n structure are shown in Figure 3-7. The differing mode indices correspond to a natural birefringence of $n_{TE} - n_{TM} = 4.3 \cdot 10^{-4}$ at λ=0.8μm, indicating comparable TE and TM mode behavior in propagation and modulation. However, as the current modulator design addresses only the TE component of the optical mode, the birefringence is irrelevant to the current operation. Both modes are approximately 1.8 μm x 2.4 μm (WxH) due to the tight horizontal confinement by the etched ridge and vertical positioning of the high-index layers. The confinement afforded by the deep etch of the structure also reduces optical mode loss in waveguide bends.

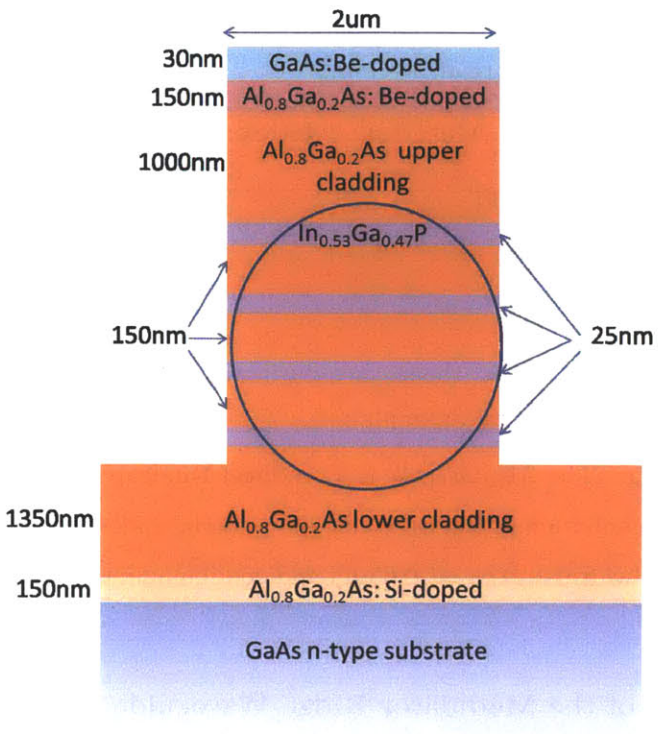

Figure 3-6: Cross-sectional drawing of the p-i-n As-based optical modulator. The optical mode (denoted by a circle) is confined to the dilute core comprised of thin alternating $Al_{0.8}Ga_{0.2}As$ and $In_{0.53}Ga_{0.47}P$ layers.

3.2.2 Applied Voltage Requirements

V_π, the voltage theoretically required to achieve a phase shift of π with an electrooptic modulator, is estimated using Equation 2.10, resulting in a $V_\pi L = 5.74$V-cm. Due to the inversely linear dependence of V_π on MZI arm length, Table 3.2 provides voltage for a variety of lengths. The computations assumed a ridge height (t_g) of 3.23μm, an effective index of refraction (as calculated by RSoft BeamPROP) of n = 3.14, and an electrooptic coefficient of $1.44 \cdot 10^{-12}$ m/V [36, 49]. As expected, longer MZI devices require a lower operating voltage.

Calculating V_π for this modulator structure appears complicated as light is guided by a number of layers of differing Al composition. It may be tempting to draw a comparison to MQW modulator structures and the effects of the thin quantum well layers on modulation voltage. However, phase modulation is a result of induced changes in the effective index of refraction due to a variety of effects - the linear electrooptic effect (LEO), quadratic

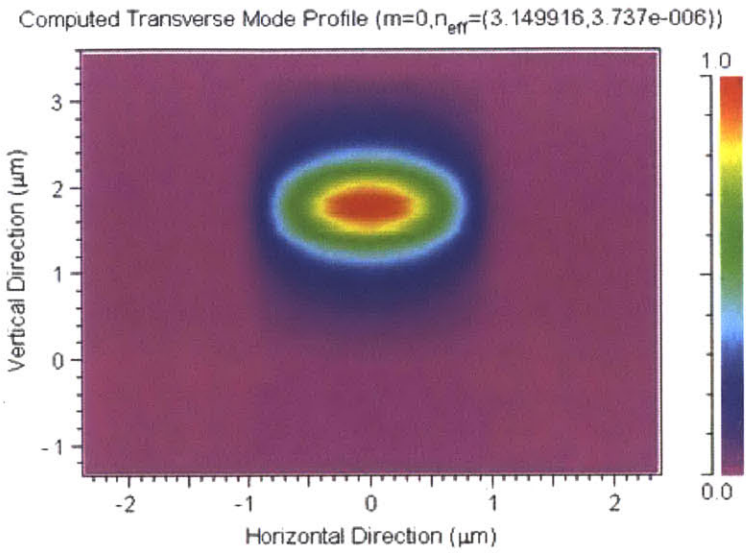

(a)

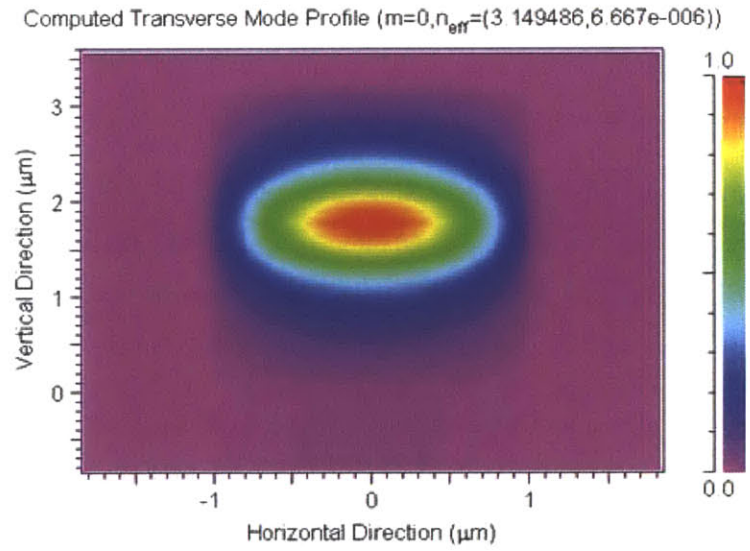

(b)

Figure 3-7: RSoft simulations of the (a) transverse electric and (b) transverse magnetic fundamental modes.

Table 3.2: Calculated values of V_π at λ=0.8μm for $Al_{0.8}Ga_{0.2}As/In_{0.53}Ga_{0.47}P$ devices of various lengths oriented in the $< 011 >$ direction. This calculation assumes an $r_{41} = 1.44 \cdot 10^{-12}$ m/V, corresponding to the behavior of a bulk GaAs semiconductor modulator.

Device Length (mm)	3.0	4.5	6.0	7.5	9.0	10.5
Device Voltage (V)	19.14	12.76	9.57	7.66	6.38	5.47

electrooptic effect (QEO), plasma effect (PL), and bandgap shifting effect (BS). The change in phase, $\Delta\phi$ is expressed as [68, 69, 70]

$$\Delta\phi = \frac{2\pi L}{\lambda}\Delta n_{eff} = \frac{2\pi L}{\lambda}(\Delta n_{LEO} + \Delta n_{QEO} + \Delta n_{PL} + \Delta n_{BS}) \tag{3.9}$$

Therefore if no other effects are present, the effective change in the index of refraction is dominated by the electrooptic effect.

3.2.3 Photolithography Mask Set Layout

With the heterostructure, propagation and mode solver simulations, optical, material, and electrical properties in mind, a photolithography mask set was developed. The layout consists of four mask layers:

1. The first mask defines the 2μm-wide ridge waveguide Mach-Zehnder Interferometer arms, which vary from 3mm to 10.5mm in length. As the effective index of refraction and electrooptic coefficients of the heterostructure are not precisely known at λ=0.8μm, a variety of MZI arm lengths were included in the design.

2. The second mask is an image reversal layer that defines passive 2μm-wide waveguides that lead to and from the MZI arms, and also defines the power splitters by surrounding these areas with 26μm-wide trenches. The trenches merely provide an alternative to etching the full wafer. Full wafer etching increases micromasking and reduces etch rates and anisotropy.

3. The third mask of the set establishes openings called vias during the etching of a planarizing layer; the vias also aid in the placement of metal contact pads.

4. The fourth mask defines openings for the top side metal contacts over the MZI arms.

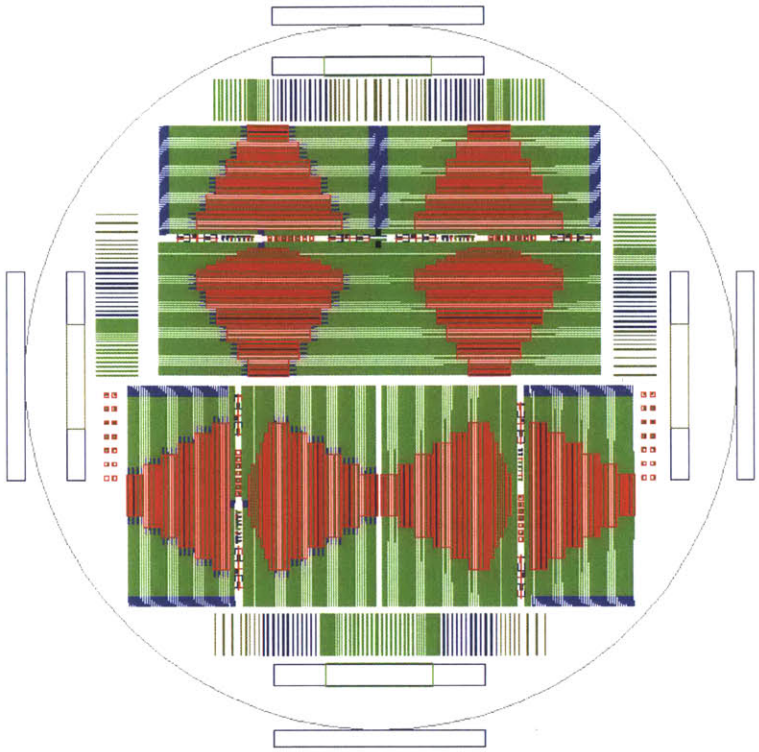

Figure 3-8: Four-layer mask set used in the fabrication of ultra-broadband modulators.

The full modulator mask layout, displayed in Figure 3-8, is composed of passive waveguides (in green) that lead to power two types of power splitters - multimode interferometers (MMIs) or Y-splitters (in dark blue). The splitters divide the input optical power evenly across the Mach Zehnder interferometer, over which the contact pads are evaporated (in red). An inverted power splitter recombines the optical power after phase modulation and transfers the signal by another passive waveguide to the output. A complete optical modulator on the mask set is 15.75mm in length. To maximize efficiency, modulators are oriented 45^o off from the top surface <100> direction. As the electric field is applied along the <001> plane, devices are oriented along the <011> and <$01\bar{1}$ > cleave directions. For more information on crystal orientation and device efficiency, [2] may be consulted. There are eight die on the mask with every combination of power splitters, crystal orientation and angled or straight input/output waveguides (to aid with facet reflections).

Power Splitters

Modulation of the phase of an optical signal is accomplished by inducing a change in material refractive index through an applied electric field. Amplitude signal modulation integrates phase modulators and power splitters. A beamsplitter ahead of the MZI input divides the optical beam into two components, and a second inverted beamsplitter (hence, a combiner) at the MZI output allows the components to recombine and interfere [71].

Several classes of beamsplitters have been theorized and constructed in GaAs-based materials, including multimode interferometers (MMIs) [72, 73], Y-junctions [74, 75], two-guide optical couplers [76, 77, 78] and three-guide couplers [79, 80]. Each power splitting device has benefits and drawbacks, and as such, two-guide and three-guide optical couplers - structures that overcome the bending loss issue of Y-junctions but demand coupling lengths that increase greatly with shorter wavelengths [81] - were not pursued. In this work, the power of an input optical beam is divided using either a multimode interferometer or a Y-junction, and beam propagation simulations of both types of power splitters were carried out to determine the device's ideal dimensions and performance. Though both MMIs and Y-junctions execute the same task, their operational methods are quite different and have distinct advantages and disadvantages.

Multimode couplers are optical devices that are designed on the self-imaging property of multimode waveguide propagation [82]. The device structure itself is engineered to support many eigenmodes, and these are excited by an incident field at the MMI input. As the modes propagate through the structure, they interfere constructively and destructively, producing a pattern of maxima and minima power distributions. At the output, the pattern is described by the difference in the phases of the fundamental mode and a higher mode, m [83]:

$$(\beta_m - \beta_0)L = -\frac{\pi m(m+2)L}{3L_\pi} \tag{3.10}$$

where L is the MMI length and L_π, the beat spacing between the two lowest order modes, is defined as

$$L_\pi = \frac{\pi}{\beta_1 - \beta_0} \approx \frac{4nW^2}{3\lambda} \tag{3.11}$$

for the MMI width W, operational wavelength λ, and the index of refraction, n. An MxN MMI has M inputs and N outputs. An MMI with one input and N output waveguides, 1xN,

will display N number of images at an MMI length of

$$L = \frac{3L_\pi}{4N} \tag{3.12}$$

This brand of imaging is symmetrical and places the input waveguide at the middle of the MMI coupler width, while the output waveguides are at a distance of W/2N from the MMI edges, and all other output waveguides in between spaced W/N apart. In the development of broadband modulators, 1x2 and 2x1 MMIs are adopted as passive waveguide splitters and combiners respectively.

MMI-based devices tout several benefits [84]:

- Polarization independence
- Low propagation losses
- Low sensitivity to etch depth relative to other couplers
- Greater tolerance to device dimensions and fabrication process

However, the advantages come at the expense of strong dependence of the MMI dimensions on wavelength and index of refraction, which often lead to large device dimensions on the order of millimeters.

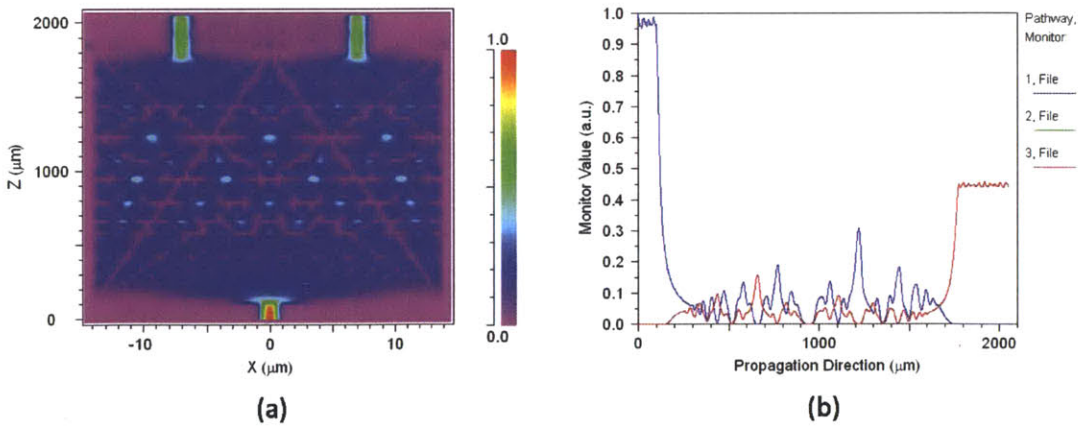

Figure 3-9: RSoft BeamPROP simulations of (a) self-imaging in a 28μm-wide and 1680μm-long multimode interferometer (MMI) and (b) simulated power in the input and output waveguides of the multimode interferometer.

The 28μm-wide MMI that is shown in Figure 3-9 is designed with the p-i-n heterostructure and operating at λ=0.8μm. The output waveguides of the MMI are located 14μm apart, center-to-center, a distance that facilitates fabrication yet, maintains a reasonable MMI length. OptiBPM 6.0 [85] and RSoft BeamPROP propagation simulations were used to determine the optimal MMI length. To account for the sensitivity of MMI devices to optical properties, MMIs of lengths 1650, 1700, 1750 and 1800μm were incorporated into the mask set. The interference pattern of a 1680μm-long MMI simulated by the RSoft calculations and the power transmission from input waveguide (blue curve) to the two output waveguides (green and overlaying red curve - with approximately 47% transmission in each) is displayed in Figures 3-9(a) and (b), respectively.

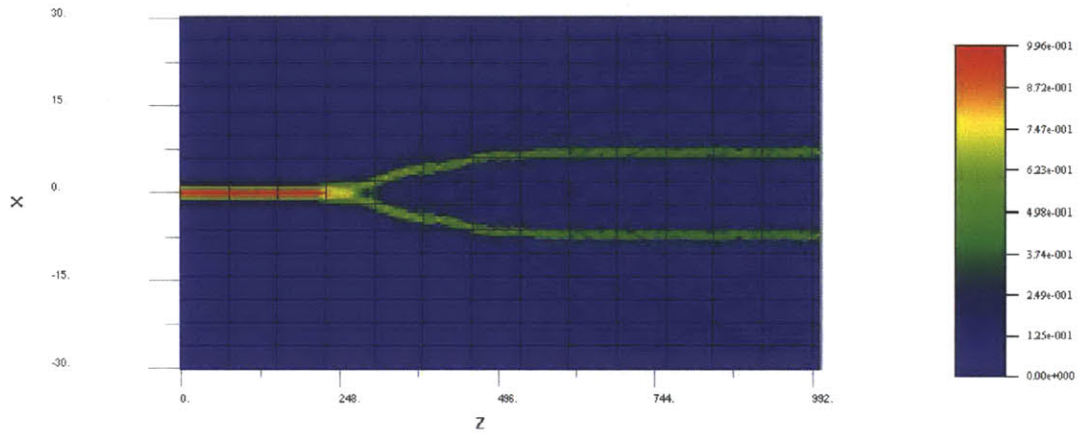

Figure 3-10: OptiBPM simulations of a 500μm Y-splitter with an 8.93mm radius of curvature. The simulated device exhibits even splitting and low bending loss.

Unlike MMIs, Y-junctions (also known as Y-splitters) use symmetric branches that bend away from the input waveguide to achieve a split of $\xi = \frac{1}{2}$. Figure 3-10 is an Optiwave OptiBPM 6.0 simulation result of a 500μm-long Y-splitter included in the mask set. As the splitting ratio relies on device symmetry, a 3dB ratio is achieved simply by designing symmetric branches. As the power split employs bends to divide and recombine optical beams, the device is characterized by bending loss. Though Y-splitters have no dependence on indices of refraction or wavelength of operation, the device is sensitive to fabrication processes due to the tight dimensions.

To determine the appropriate bending radii that are associated with minimal losses in the Y-splitter, a Matlab program that was developed by Dr. Milos Popovic of MIT

was employed. The computation assumed weak confinement of the optical mode by a shallow ridge p-i-n structure, and indicated that a 250μm radius was sufficient for low loss splitting. For simpler integration in the mask layout, the Y-splitters lead to outputs of the same separation distance of 14μm. A 500μm device length was chosen, translating to an extremely gradual bend with a radius of curvature of 8.93mm.

3.2.4 Fabrication of the p-i-n Modulator

This section provides an overview of the processing steps that were undertaken in the fabrication of the p-i-n arsenide-based modulators. For more information about the processing technologies consult Appendix A.

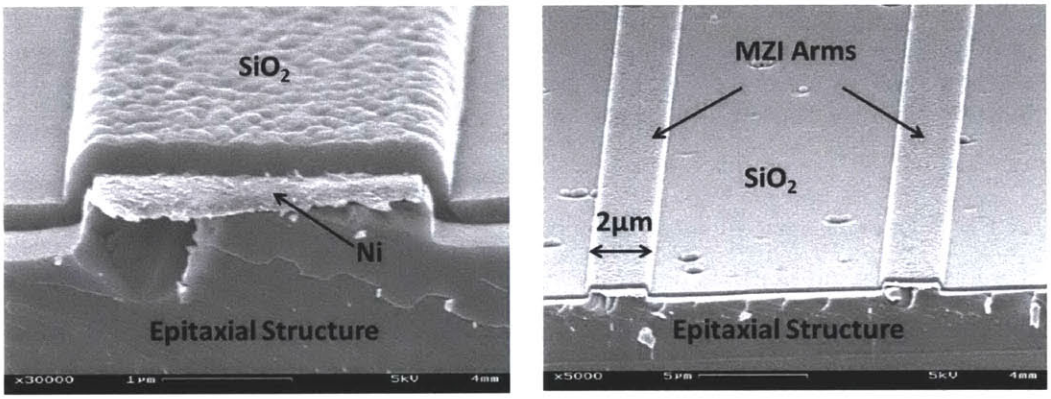

Figure 3-11: Scanning electron micrograph images of (a) an etched MZI ridge covered with a 100nm Ni protective mask and sputtered oxide and (b) view of the wafer topography following the first photolithography, etch, and deposition steps.

Fabrication of the modulator devices commences with image reversal photolithography, evaporation of a 100nm-thick film of Ni, and lift-off in acetone to define 2μm-wide lines in Ni. The Ni hard mask protects the MZI ridge area from etching during a subsequent low-pressure, high-bias voltage BCl_3-based reactive ion etch (RIE) to remove the top doped contact layers from all passive device areas. The doped semiconductor material must be etched away completely in regions outside the MZI ridges to prevent the electrical shorting of devices on the wafer.

In preparation for a second semiconductor etch, a 250nm-thick film of SiO_2 is deposited

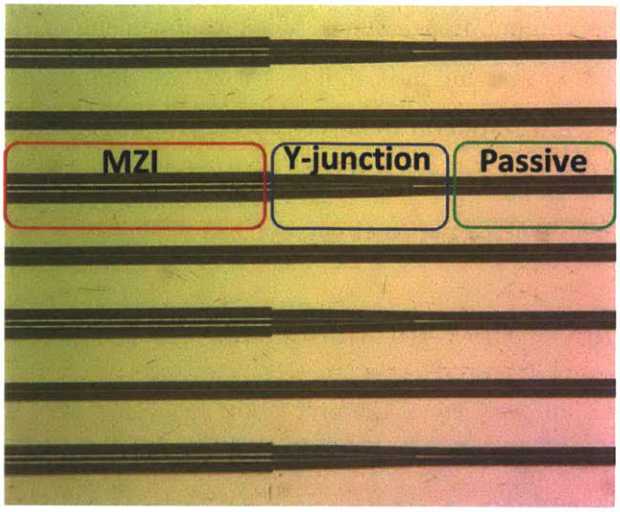

Figure 3-12: Microscope image of broadband modulator device following the second photolithography and RIE of SiO_2 hard mask, defining beamsplitters and passive waveguides prior to III-V RIE. The critical alignment between the MZI arms (red box) defined in the first lithography process and the beamsplitters (blue) and passive waveguides (green) established in the second lithography step is a difficult endeavor.

by PECVD, or plasma-enhanced chemical vapor deposition. Unlike evaporation, which is a directional method of deposition, PECVD is conformal and successfully covers uneven and difficult topography (sidewalls, trenches, etc). This oxide layer serves as the hard mask in the deep, ridge-defining RIE of the III-V materials, and is therefore thicker and applied at a high frequency for a denser film. The MZI arms, covered by the thin Ni layer and thicker SiO_2, are visible in Figure 3-11.

The second lithography step (Figure 3-12) is particularly difficult, requiring alignments of 2μm-wide features over distances on the order of centimeters. Accuracy in this alignment is essential in preventing power loss between passive and active areas. After a short ash step consisting of a He/O_2 reactive ion etch to smooth the resist sidewalls, the resist pattern is transferred to the deposited SiO_2 film by a 30nm/min CF_4 RIE process developed by Ryan Williams [86]. Once the upper $Al_{0.8}Ga_{0.2}As$ layer is exposed, a second BCl_3 RIE defines the power splitters and passive waveguides and determines the ridge height.

Evaporation of top-side metal contacts necessitates a relatively flat surface attained by a planarization. A spin-on dielectric coats the sample, filling in the trenches and burying the ridges to create a uniform topography. A flowable oxide, Hydrogen SilsesQuioxane (HSQ) (Figure 3-13) is spun and cured with a high temperature bake, and then etched back

to expose the nickel-covered MZI arms to which the top-side metal must make contact. The third lithography mask may be used to protect areas during the etch-back, but is not essential.

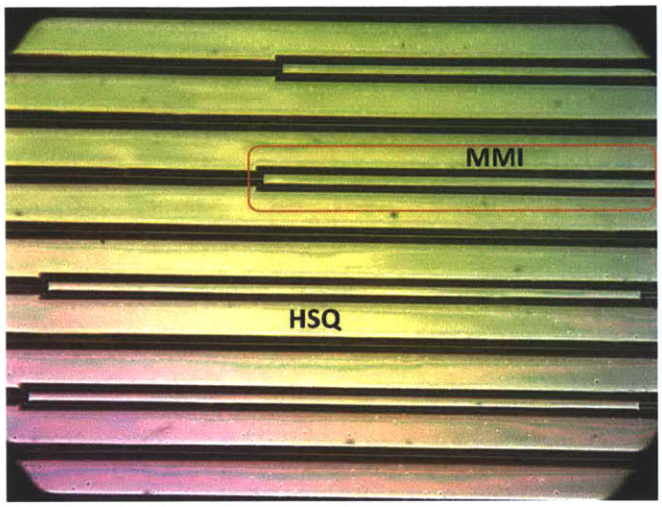

Figure 3-13: Multimode Interferometer devices (orange box) and passive waveguides planarized by spin-on hydrogen silsesquioxane (HSQ).

The final mask in the set creates the top side metal contacts with an image reversal, deposition, and lift off process. Ti/Pt/Au films of thicknesses 300 Å, 200 Å, and 2000 Å respectively, are sequentially evaporated onto the sample to form large p-type ohmic contact pads that power the modulators. The back-end processing involves thinning of the substrate from a thickness of 350μm to approximately 175μm for improved facet cleaving (a procedure developed by Dr. Sheila Nabanja of the Integrated Photonic Devices and Materials Group). Once thinned, n-type ohmic backside contacts of Ge/Au/Ni/Au of thicknesses 300 Å, 600 Å, 300 Å, and 2000 Å are evaporated and the metal is annealed. Lastly, the dies are cleaved and mounted on copper blocks for testing.

3.2.5 Optical Characterization

To gauge the quality of the fabrication and mask layout, as well as the heterostructure performance as an optically guiding structure, passive optical characterization measurements were performed. Passive measurements are primarily used to ascertain device propagation losses (or power transmission losses), an important metric of modulator operation. The

characterization setup, illustrated in Figure 3-14[2] includes a laser source that generates an optical beam with sufficient input power and operates at a wavelength appropriate for the broadband modulator. The laser beam is passed through a polarizer to remove the TM polarization that cannot be modulated with this type of electrode configuration (see Section 2.1.2). The beam is coupled in and out of the device using a lensed fiber that is

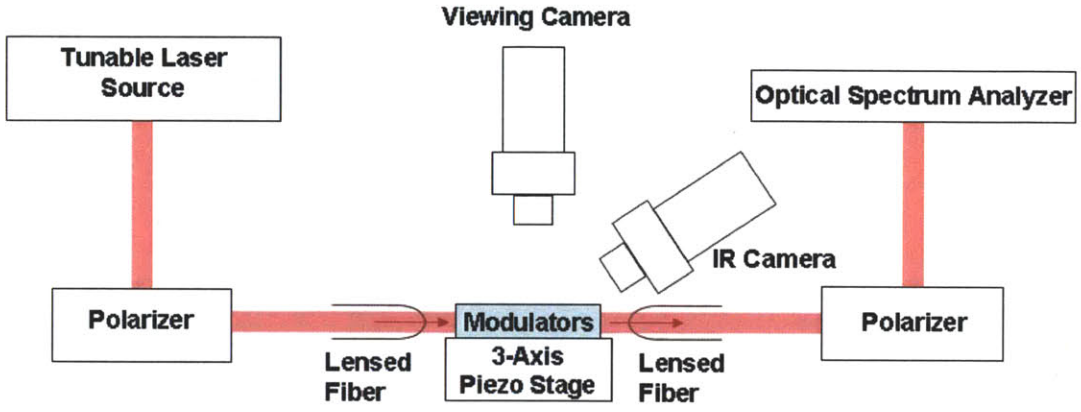

Figure 3-14: Schematic of the passive optical characterization setup. A polarizer filters the TM polarization of an optical beam generated by a laser source. Lensed fibers couple the beam to the waveguide modulator input and from its output. The collected light is analyzed with a second polarizer and optical spectrum analyzer [2].

positioned on a 3-axis piezo stage. Top view cameras aid in aligning the lensed fibers to the waveguide input and output facets. An infrared camera is placed at the waveguide output, providing images of light dispersion along the full length of the device. At the output, the beam is coupled to a second polarizer, and is transmitted to an optical spectrum analyzer (OSA) synchronized to the laser source in order to measure the optical transmission across the ridge waveguide as a function of wavelength.

Measurements of this device were carried out by Dr. Marcus Dahlem of the Optics and Quantum Electronics Group at MIT. A 980nm laser beam was coupled into a 2.5mm-long cleaved MZI-portion of the modulator (propagation losses in the structure were too high to propagate light across the full 15.75mm die). The top and end-view cameras (as seen in Figure 3-15) observed the light along the output and top of the waveguide.

Despite the visibility of light at the end of the 2.5mm device, the optical intensity at the output was weak and could not be coupled in and measured by the OSA. Propagation losses were instead estimated by images that were taken by an overhead camera that show

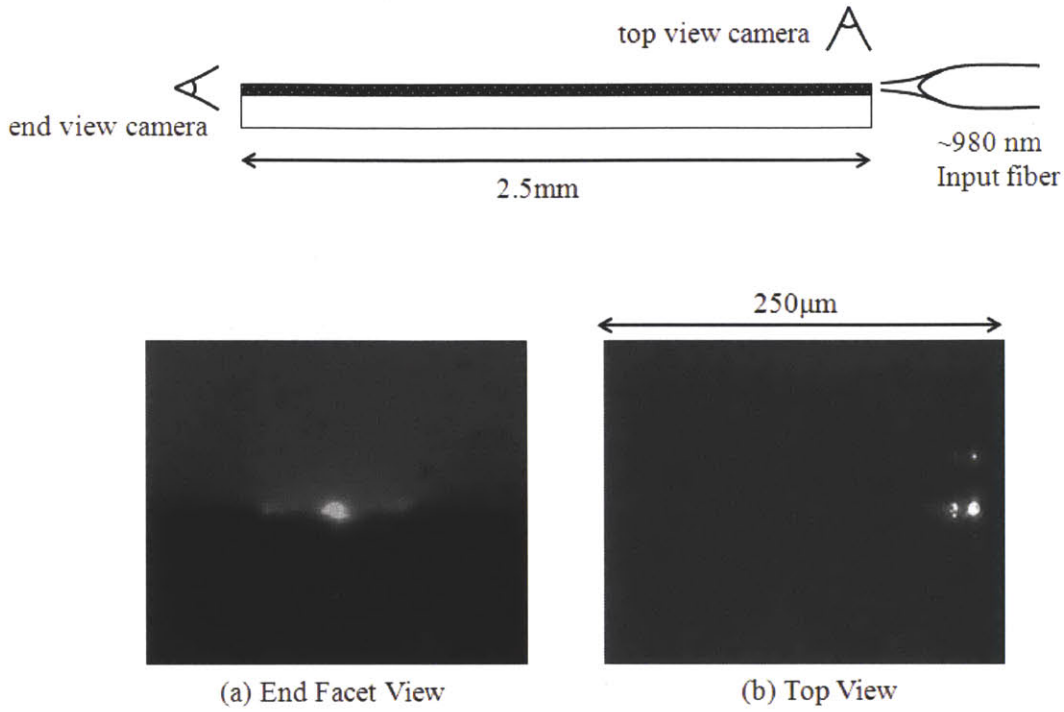

Figure 3-15: End facet (a) and top view (b) images of light propagating through a 2.5mm-long waveguide modulator. While light was visible at the output, the intensity was too close to the noise floor. Losses of 120dB/cm were estimated using images captured by an infrared camera.

light dissipation of approximately 3dB over 250μm of waveguide length, corresponding to losses of 120dB/cm.

The primary source of loss can be deduced from Figure 3-16. The roughness of the HSQ mirrors the roughness of the wafer surface, suggesting that during the RIE process there was some difficulty in removing the $In_{0.53}Ga_{0.47}P$ semiconductor layers, which require a high temperature etch. In the absence of a chemical etch, the $In_{0.53}Ga_{0.47}P$ layers were primarily removed by physical means, or sputtering, giving way to extremely uneven topography. The ridge waveguide sidewalls were affected as well and the consequences are visible in the broadening of the ridge width from its peak to base. The sidewall roughness contributed to substantial scattering losses of the optical mode, explaining the propagation loss estimates that were indicated by optical characterization images.

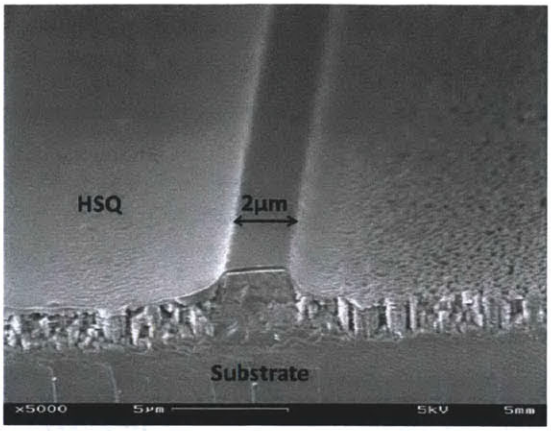

Figure 3-16: Scanning electron microscope image of a passive input waveguide that was planarized by HSQ. The roughness of the HSQ mirrors the roughness of the wafer surface as a result of the difficulty in removing $In_{0.53}Ga_{0.47}P$ material in the BCl_3 RIE.

3.3 n-i-n MOS-Based Heterostructure

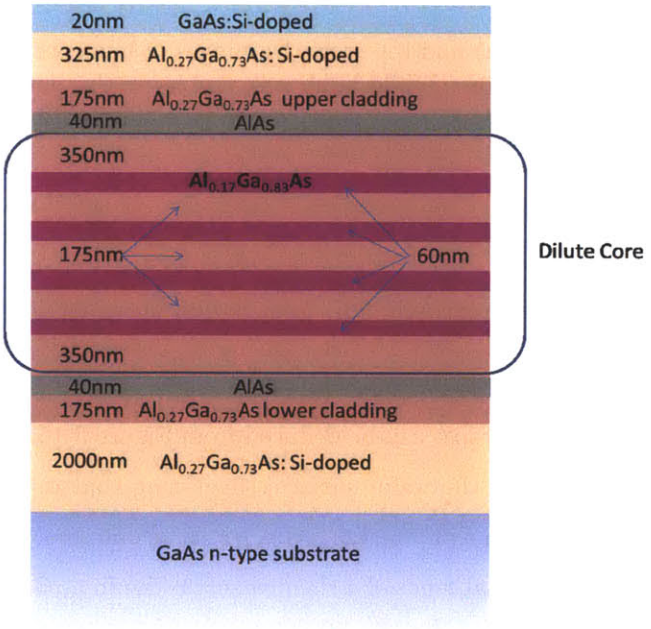

Figure 3-17: The n-i-n Metal-Oxide-Semiconductor (MOS) modulator heterostructure. The optical mode (denoted by a circle) is confined to the dilute core comprised of thin alternating $Al_{0.27}Ga_{0.73}As$ and $Al_{0.17}Ga_{0.83}As$ layers. Oxidizable AlAs layers have been added to enhance the vertical confinement of the optical mode.

In response to the results obtained from the fabricated p-i-n structure, an n-i-n Metal-Oxide-Semiconductor (MOS) structure (Figure 3-17) was designed and grown by MBE. The structure consists entirely of GaAs, $Al_xGa_{1-x}As$, and AlAs films - material systems that are lattice-matched and behave similarly when processed.

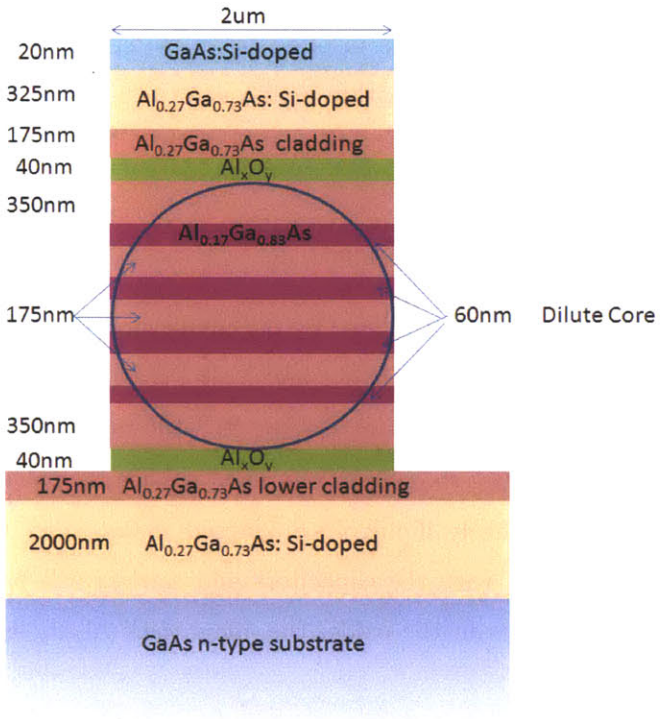

Figure 3-18: The n-i-n MOS ridge waveguide modulator epitaxial structure. The optical mode (denoted by a circle) is strongly confined by oxidizable 40nm-thick AlAs layers.

Certain design elements of the p-i-n design have been borrowed and integrated into the novel heterostructure. Thick lower and upper $Al_{0.27}Ga_{0.73}As$ cladding layers isolate the mode from the substrate and electrical contacts, respectively. As in the p-i-n structure, the new design includes a dilute core composed of repeating 175nm-thick, low-index $Al_{0.27}Ga_{0.73}As$ and 60nm-thick, high-index $Al_{0.17}Ga_{0.83}As$ layers. The resultant active region has an index of refraction only slightly higher than its surroundings, reducing fiber-to-waveguide coupling losses yet providing adequate mode confinement. Additionally, the upper and lower Si-doped (n-type) GaAs and $Al_{0.27}Ga_{0.73}As$ epitaxial layers have a lower bandgap to aid in making contact to evaporated metal layers. The elimination of p-type

materials in the modulator structure is also expected to lower electrical and optical losses [65]

Two AlAs layers surrounding the dilute core have been added to the original heterostructure. After the ridge-defining etch, the exposed AlAs films can be thermally oxidized to form Al_xO_y layers that strongly confine the optical mode in the dilute core as shown in Figure 3-18. This structure was inspired by Si modulator designs that embed a metal-oxide-semiconductor capacitor within a silicon waveguide structure to achieve high-speed phase modulation [87, 88].

3.3.1 Electrical Performance

The n-i-n heterostructure is described by the circuit model shown in Figure 3-19. While the top and bottom doped semiconductor layers are expected to conduct current and operate as resistors, the near-intrinsic (likely n-type 10^{14}-10^{15}cm^{-3}) $Al_{0.27}Ga_{0.73}As$ core and upper and lower cladding layers should deplete when voltage is applied, and can be modeled as capacitors. Though unlikely, if pinholes are present in the oxides, the oxide layers will behave as resistors in parallel with the capacitors and carriers will pass through the structure. If there are no pinholes in the oxide, the 40nm-thick Al_xO_y layers will perform as ideal capacitors.

To verify the circuit model and to determine that there is indeed an electric field in the core - a requirement for optical modulation with this structure - two approaches were pursued. First, the heterostructure was simulated on Silvaco's Atlas software [89] using the parameters listed in Table 3.3, to better understand the behavior of the epitaxial structure in response to an applied voltage. Voltages were applied to the topside metal, while the backside metal was grounded.

Figure 3-20 exhibits the potential, conduction band energy, and electron Fermi levels when no voltage is applied across the structure. The potential is obtained by solving Poisson's equation, which relates variations in electrostatic potential to local charge densities, given by

$$div(\varepsilon \Delta \psi) = -\rho \tag{3.13}$$

where ε is the permittivity, ψ is the electrostatic potential, and ρ is the space charge density.

Due to the high doping at the boundary between the doped $Al_{0.27}Ga_{0.73}As$ and the

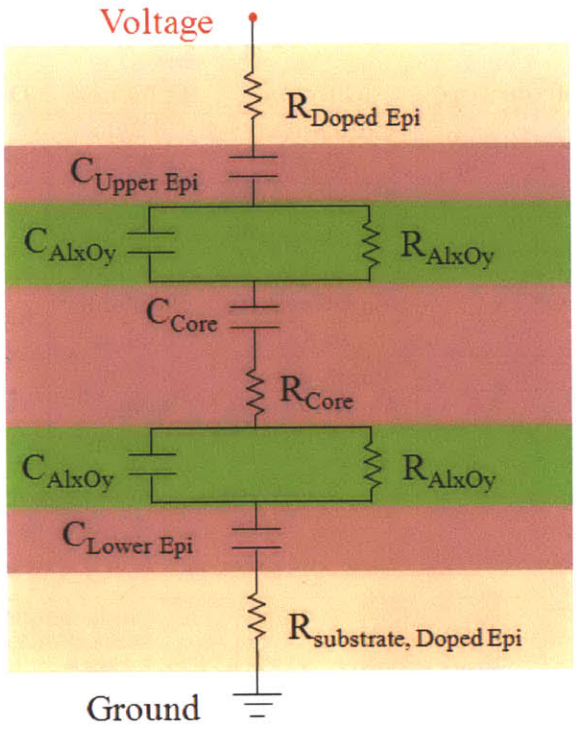

Figure 3-19: A circuit model representation of the n-i-n MOS heterostructure. In the presence of possible pinholes, the oxide will behave as a parallel resistor/capacitor rather than as an ideal capacitor. The presence of pinholes in the oxide will allow carriers to flow into the core of the structure. The capacitance of the near-intrinsic (n-type 10^{14}-10^{15} cm^{-3}) semiconductor regions is dependent upon the depletion region that forms upon the application of a voltage across the structure.

upper cladding, and similarly at the boundary between the doped $Al_{0.27}Ga_{0.73}As$ and the lower cladding, the conduction bands bend toward the Al_xO_y interface. In response to the band bending in the cladding layers, band bending is also seen at the edges of the core by the Al_xO_y layers. Despite the observance of depletion regions at the Al_xO_y interfaces, there is no significant depletion seen in the core of the heterostructure.

When the applied voltage is increased to 1V, as shown in Figure 3-21(a), the upper cladding layer is quickly depleted of electrons due to the low doping of the layer, and holes accumulate at the Al_xO_y interface. As a result, electrons accumulate at the opposite interface within the core of the structure, causing comparable bending of the conduction

Table 3.3: Material thickness and doping values that were used in simulating the electrical behavior of the n-i-n MOS heterostructure.

Layer number (from top)	**Material**	**Thickness**	**Doping (n-type in cm^{-3})**
1	Aluminum	$0.2\mu m$	10^{20}
2	GaAs	$0.02\mu m$	10^{18}
3	$Al_{0.27}Ga_{0.73}As$	$0.325\mu m$	10^{18}
4	$Al_{0.27}Ga_{0.73}As$	$0.175\mu m$	10^{15}
5	Al_xO_y	$0.04\mu m$	insulator
6	$Al_{0.27}Ga_{0.73}As$	$1.465\mu m$	10^{15}
7	Al_xO_y	$0.04\mu m$	insulator
8	$Al_{0.27}Ga_{0.73}As$	$0.175\mu m$	10^{15}
9	$Al_{0.27}Ga_{0.73}As$	$2.00\mu m$	10^{18}
10	GaAs	$5.00\mu m$	10^{18}
11	Aluminum	$0.2\mu m$	10^{20}

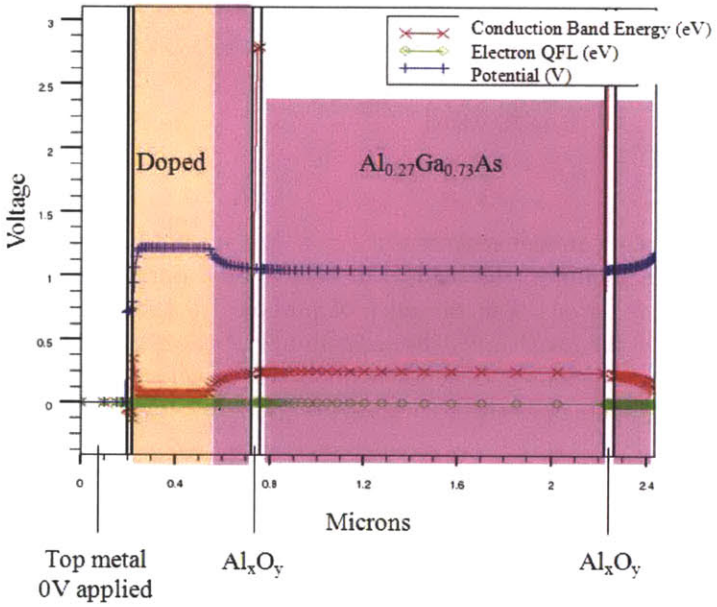

Figure 3-20: Atlas simulation of the conduction band energy, potential, and electron Fermi levels at 0V applied voltage. There is no significant potential across the core of the structure at this voltage, though there is slight band bending at the oxide interfaces. Orange-shaded areas represent the doped semiconductor materials, while the near-intrinsic materials are shaded in pink.

energy band in the lower cladding layer. A potential of approximately 0.25V is seen across the core, and the potential continues to increase with the applied voltage. At an applied voltage of 3V [Figure 3-21(b)], the potential across the core is approximately 1.5V and the layer is nearly depleted, as suggested by the proximity of the conduction band energy and the electron Fermi level. Increasing the voltage brings the potential across the core to a maximum value of around 1.75V, corresponding to the bandgap of the $Al_{0.27}Ga_{0.73}As$. At this value, the $Al_{0.27}Ga_{0.73}As$ is fully depleted and the electron Fermi level and the conduction band meet at the upper Al_xO_y interface.

When a voltage is applied, the charge carriers diffuse away from each other, creating a depletion region between them. The end-result resembles a parallel-plate capacitor, which consists of two conductors that are separated by an insulating material. Capacitance, C, describes the charge-storing ability of a body. The capacitance of a parallel-plate capacitor is given by

$$C = \frac{\epsilon_r \epsilon_0 A}{t} \tag{3.14}$$

where ϵ_r is the relative permittivity of the material between the conductors, ϵ_0=$8.85 * 10^{-12}$ F/m is the vacuum permittivity, A is the area in which the two conductors overlap, and t is the thickness of the insulating material in between the conductors.

As the layers in the heterostructure deplete, they display the behavior of capacitors. When positive voltage is applied, the upper cladding layer and the core exhibit significant depletion according to the simulation, and can hence be thought of as capacitors in series. The oxides inherently perform as capacitors until breakdown. While there is some depletion in the lower cladding layer, the contribution to the capacitance of the heterostructure is very small in comparison to contributions from the upper cladding, oxides, and the core, and is not taken into account under a positive applied voltage. The total contribution of the primary capacitors (the two oxides, core, and upper cladding layer) can be assessed by calculating the capacitance of each and adding them in series in the following manner:

$$C_{heterostructure} = \frac{1}{\frac{1}{C_{Al_xO_y}} + \frac{1}{C_{Al_xO_y}} + \frac{1}{C_{UpperCladding}} + \frac{1}{C_{Core}}} \tag{3.15}$$

The permittivity of $Al_xGa_{1-x}As$ materials is determined for Al concentrations under static conditions by

$$\epsilon_r = 12.90 - 2.84x \tag{3.16}$$

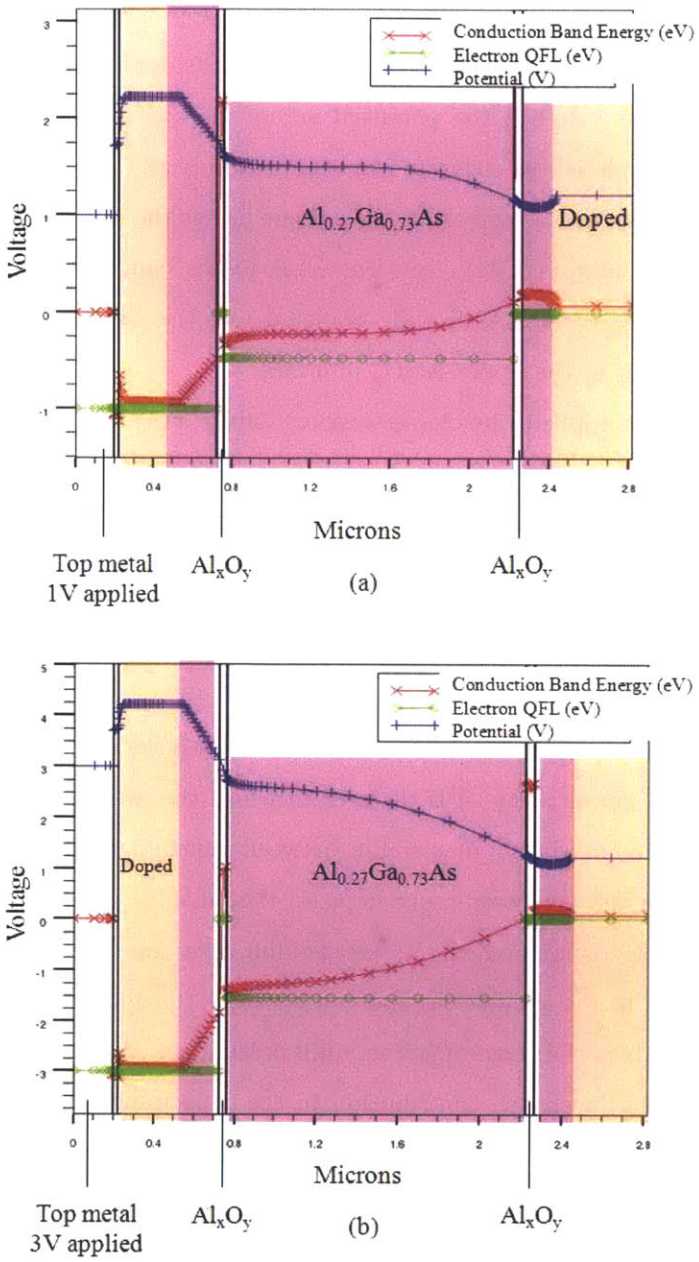

Figure 3-21: Atlas simulation of the conduction band energy, potential, and electron Fermi levels at (a) 1V and (b) 3V applied voltage. (a) At 1V, the potential across the core is 0.25V. (b) At 3V, the potential across the core is 1.5V, already close to the maximal value of 1.75 corresponding to the bandgap of the $Al_{0.27}Ga_{0.73}As$. Orange-shaded areas represent the doped semiconductor materials, while the near-intrinsic materials are shaded in pink.

The permittivities for the $Al_{0.27}Ga_{0.73}As$ and Al_xO_y materials are provided at static frequency in Table 3.4 below.

Table 3.4: Relative permittivities of the Al_xO_y and $Al_xGa_{1-x}As$ materials

Material	Static Permittivity
Al_xO_y	8.3 [90]
$Al_{0.27}Ga_{0.73}As$	12.1

Table 3.5: Calculated area-normalized capacitances at low frequency of the Al_xO_y and upper cladding layers.

Layer	Capacitance/Area
Al_xO_y	$6.12 * 10^{-4}$ F/m^2
$Al_{0.27}Ga_{0.73}As$ Upper Cladding	$1.84 * 10^{-3}$ F/m^2

The upper low-doped cladding depletes almost immediately upon the application of voltage. The contribution of that layer, as well as that of the two oxides, will essentially be unchanged as voltage increases, so they may be treated as constants. The calculated capacitances per area for the oxide and upper cladding layers is provided in Table 3.5, assuming relative permittivity values at low frequency. The depletion region in the core increases with applied voltage, ideally reaching a thickness of 1.465μm, the thickness of the dilute core. Figure 3-22 presents the expected area-normalized capacitance of the heterostructure as a function of the increasing depletion region thickness in the core at low frequency. If the depletion region extends across the full height of the core, the total capacitance of the structure is $6.1 * 10^{-5}$ F/m^2 at low frequency. From the simulations, the core is expected to be fully depleted by an applied voltage of 10V, at which point these capacitance values are expected to be reached.

When a negative voltage is applied (by probing the back electrode and grounding the top electrode), the simulated electrical behavior of the structure differs from the operation under positive applied voltage. As the negative voltage is applied, the lower cladding layer depletes quickly. The conduction and valence bands in the core region begin to bend upward primarily at the interface between the core and the upper Al_xO_y, however this effect progresses far slower than under positive applied voltages. Figures 3-23(a) and (b) exhibit the simulated effects of applied voltages of -10V and -20V, respectively. When -10V

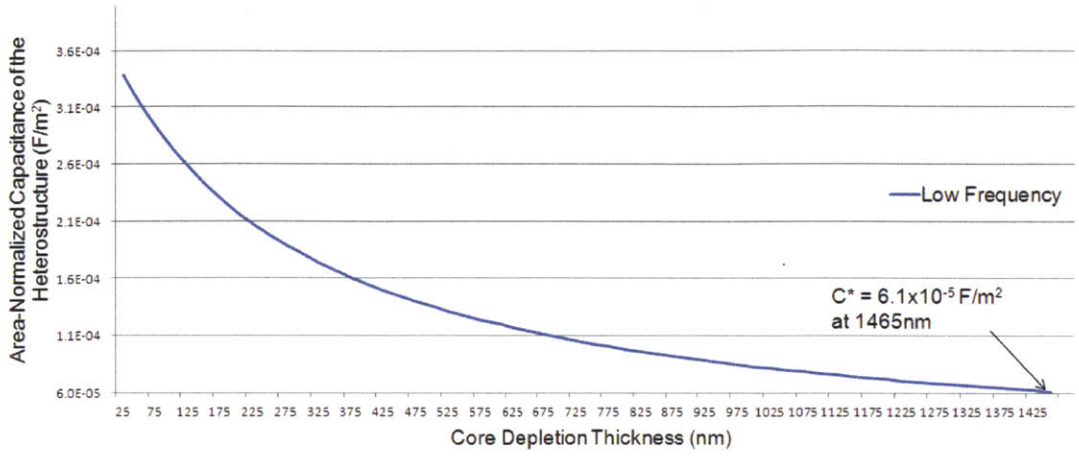

Figure 3-22: Area-normalized capacitance of the heterostructure as a function of the thickness of the depletion region of the core at low frequency. Contribution in capacitance from the two oxide layers and a single low-doped cladding layer are considered.

is applied to the top electrode, the potential across the core is approximately 0.3V and the depletion region thickness in the core appears to be in the vicinity of 600nm. However, as the voltage is increased to -20V, the core appear to be nearly fully depleted. As in the scenario of positive applied voltage, the contributors to the capacitance are the lower cladding layer, the two oxides, and the slowly depleting core. From the simulations, the capacitance is expected to remain relatively unchanged as the voltage is varied between 0V and -10V, and to drop down to the lowest capacitance value, observed when the core is fully depleted, around -20V.

The electrical behavior of the heterostructure can be further assessed by measuring the capacitance-voltage (C-V) response of the epitaxial structure. An MBE-grown sample was prepared for the C-V measurements with a photolithography step and lift-off of a metal stack consisting of 30nm Ge/60nm Au/30nm Ni/60nm Pt. A lithography mask was used to pattern 13μm-wide rectangles which vary in length from 3mm to 10.5mm. An identical metal stack was also deposited on the backside of the sample. The topside metal was used as a protective etch mask during a III-V etch of the semiconductor materials, which formed ridges of the dimensions of the lithography patterns. The AlAs layers were oxidized in a wet oxidation step at 420°C for 15min, a high temperature process that annealed the electrical contacts at the same time. The sample was probed on the backside contact and grounded

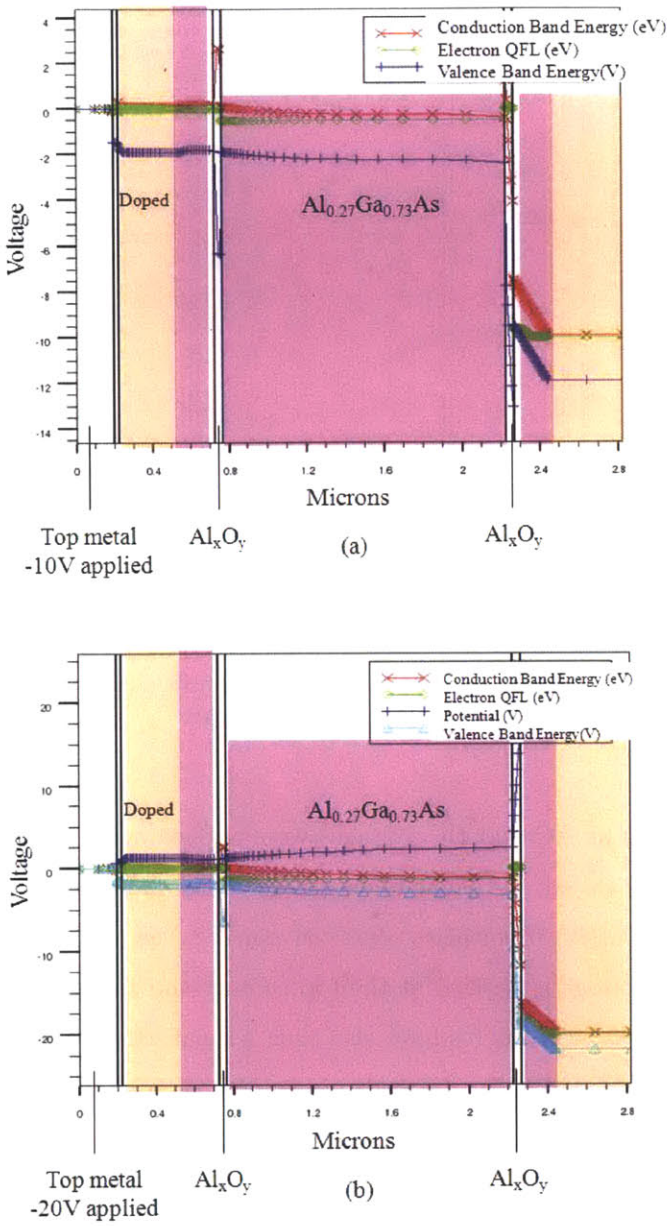

Figure 3-23: Atlas simulation of the conduction band energy, valence band energy, potential, and electron Fermi levels at (a) -10V and (b) -20V applied voltage. (a) At -10V, the lower cladding layer is depleted and the core sees a drop in potential of 0.3V. (b) At -20V, the core is nearly fully depleted, as indicated by the proximity between the conduction band and the electron Fermi level at the lower oxide interface. Orange-shaded areas represent the doped semiconductor materials, while the near-intrinsic materials are shaded in pink.

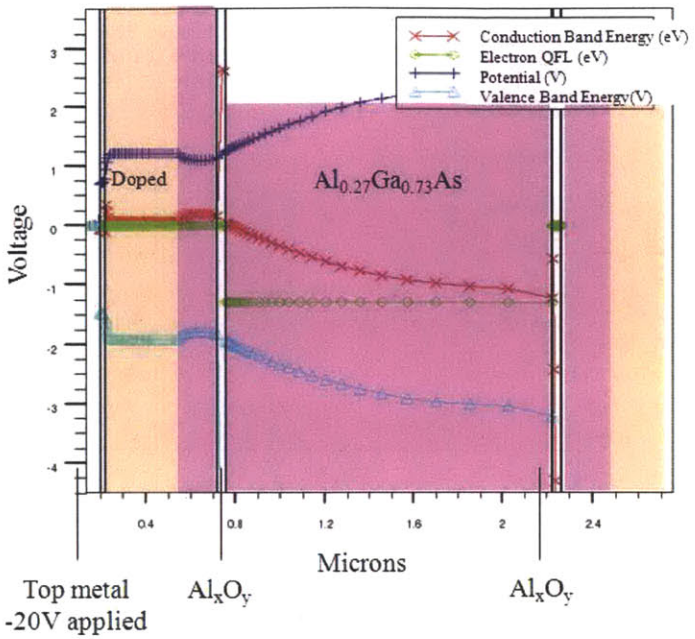

Figure 3-24: Magnified image of the Atlas simulation of the conduction band energy, valence band energy, potential, and electron Fermi levels at -20V.

on the top contacts as AC and DC voltages were applied across the heterostructure. As the DC voltage was varied, the capacitance was recorded and plotted in Figure 3-25 at low (1kHz) and high (1MHz) frequencies. For convenience, the plots were reversed to reflect the case where a voltage is applied at the top contact and the bottom contact grounded, similar to simulations. The curves have also been normalized to the area of the devices, to provide the capacitance in units of Farads per square meter.

As the voltage is increased positively, the core begins to deplete, reaching full depletion at approximately 10V, at which point the capacitance curve flattens. In both 1kHz and 1MHz frequency measurements, the capacitance reaches a value of $6 * 10^{-5}$ F/m^2, a value that is close to the $6.1 * 10^{-5}$ F/m^2 capacitance value that was calculated using the information from the simulations. As the voltage is increased in the negative direction, the core depletes and reaches full depletion around -20V, and a capacitance value of the heterostructure of $6*10^{-5}$ F/m^2 is recorded. As expected from the simulations, the voltage required to deplete the core is not equal under positive and negative bias. There are several reasons for this occurrence, including the asymmetry of the structure due to the 360μm-thick substrate and the 2μm-thick doped $Al_{0.23}Ga_{0.73}As$ layer, and the possibility of trapped charge in the oxide

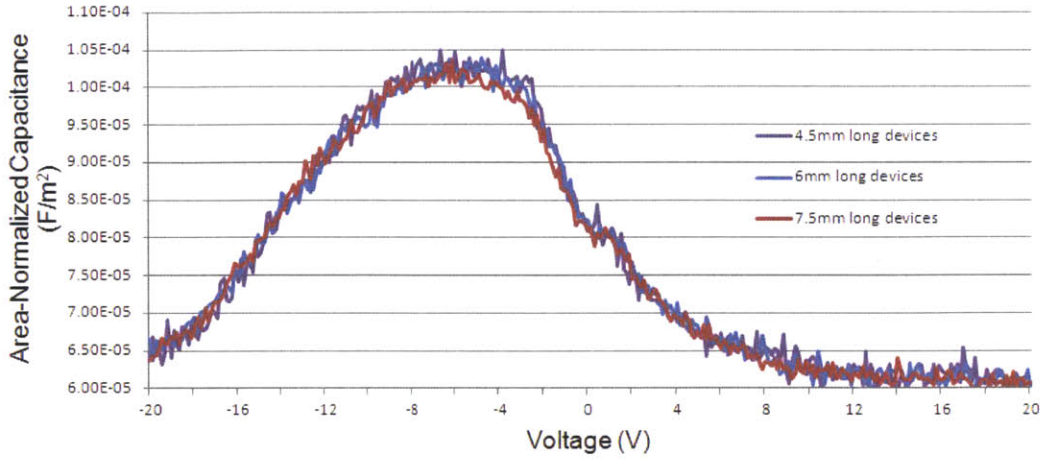

(a) Capacitance measurements at 1kHz

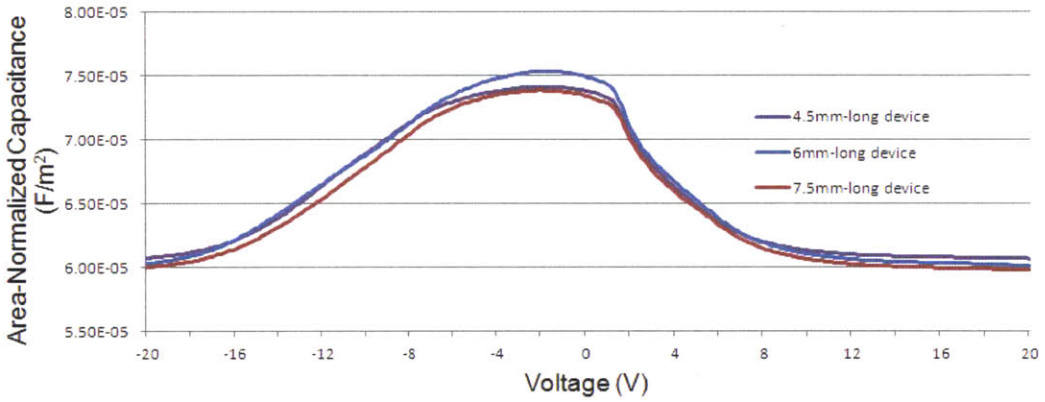

(b) Capacitance measurements at 1MHz

Figure 3-25: Area-normalized capacitance-voltage measurements obtained from three rectangular structures that are 13μm-wide and 4.5mm, 6mm, and 7.5mm-long at (a) 1kHz and at (b) 1MHz.

and at the oxide interface resulting from the wet thermal oxidation of the AlAs layers.

While there is a disparity between operation under positive and negative bias that is applied to the top electrode, the simulations and C-V measurements indicate that there is indeed a field across the core, and that the core fully depletes as the voltage is increased (in absolute terms). Hence, there will be an overlap, Γ, between the optical mode and the applied electric field, equal to 1 as expected. When Γ is less than 1, the voltage that is

required to achieve signal extinction during modulation would increase, as described by the expression:

$$V_\pi = \lambda \frac{t_g}{L n^3 r_{41}} \frac{1}{\Gamma} \tag{3.17}$$

3.3.2 Disadvantages of the n-i-n MOS Structure

Despite the many benefits of the all $Al_xGa_{1-x}As$/GaAs heterostructure, there are also drawbacks to the design. The difficulties encountered in the course of the design and simulation of the epitaxial and ridge waveguide structure, and during the development of fabrication techniques, are discussed in this section.

Semiconductor Epitaxial Structure

The refractive indices of materials that are included in the heterostructure are provided in Tables 3.6 and 3.7 [66]. There is some ambiguity surrounding the precise indices of refraction of $Al_xGa_{1-x}As$ materials at λ=0.8μm. There are two methods of calculating n, namely the Adachi Method [91], which does not take temperature into consideration, and the Gehrsitz Algorithm [92], which is more recent and takes temperature into account. Results calculated by the Gehrsitz Algorithm are very close to measured results in the 950-1600 nm range, but beyond that wavelength range, errors may arise.

Table 3.6: Refractive indices at λ=0.8μm of $Al_xGa_{1-x}As$ materials composing the n-i-n MOS modulator heterostructure.

Material	Gehrsitz Index at 0.8μm	Adachi Index at 0.8μm
$Al_{0.17}Ga_{0.83}As$	3.531	3.585
$Al_{0.27}Ga_{0.73}As$	3.441	3.491

Table 3.7: Refractive indices at λ=0.8μm of GaAs, AlAs and Al_xO_y materials composing the n-i-n MOS modulator heterostructure.

Material	Refractive Index at 0.8μm
GaAs	3.664
AlAs	3.004
Al_xO_y	1.79

The obscurity of essential electro-optic properties at $\lambda = 0.8\mu$m presents a problem in laying out the devices, namely MMIs, as simulations can only provide results that are as accurate as the numbers that are provided. In this work, calculations based upon both the Adachi and Gehrsitz methodologies will be provided. Such variations do not affect the performance of Y-junctions, but do slightly alter the TE and TM mode indices of refraction as calculated by the Gehrsitz and Adachi methods.

Optical Bandwidth

The materials adopted in the design of the n-i-n modulator reduce the optical bandwidth of the heterostructure from 650nm$< \lambda$ (p-i-n structure) to around $750< \lambda$. Despite the reduction, this bandwidth is sufficient for the purposes of this work. However, if supporting capabilities that reach further into the infrared and visible light spectrums are desired, it is possible to adopt other compositions of $Al_xGa_{1-x}As$ and $In_xGa_{1-x}P$ materials, at the expense of more difficult epitaxial growth and fabrication processes.

Device Processing

The adoption of a $Al_xGa_{1-x}As$/GaAs/AlAs heterostructure simplifies the reactive ion etching process but has ramifications for the etch selectivity between the semiconductor materials. High selectivities of GaAs materials to $Al_xGa_{1-x}As$ (> 200:1) have been achieved by careful selection of gas flows and chemistries, etch pressures and powers [93, 94], but the strong selectivity does not easily extend to differentiated etches between AlAs and low Al content $Al_xGa_{1-x}As$. Chemistries employed to remove $Al_xGa_{1-x}As$ materials react similarly with AlAs, making it difficult to design a selective etch. The heterostructure material design compensates for this occurrence by including a thick upper cladding layer that does not serve as an "etch stop" but as an "etch stopping window" - providing a range of depths in which to terminate the etch.

Oxidation of the AlAs layers during the device fabrication process raises concerns of alterations of device design/performance. In strained $In_xGa_{1-x}As$/GaAs superlattices, the oxidation of an underlying AlAs layer promotes the relaxation of strain by producing misfit dislocations, and subsequently reducing photoluminescence intensity of the single $In_xGa_{1-x}As$ quantum well [95, 96]. This occurrence is unlikely in the n-i-n MOS structure, as the design is closely lattice-matched. However, the oxidation may produce a rougher

$Al_xGa_{1-x}As/Al_xO_y$ interface that could contribute to optical scattering. This is a common issue in distributed Bragg reflectors (DBRs), non-absorbing cavities that experience reduced reflectivity correlated with a rise in surface roughness at Al_xO_y interfaces. Due to the magnitude of the uneven surface morphology (on the scale of nanometers [97]), and the minimal optical mode presence at the interface, surface roughness is not expected to impede device performance. However, the hypothesis must be experimentally verified (see Section 4.2.3).

3.3.3 Advantages of the n-i-n MOS Structure

The novel modulator heterostructure design that is introduced in this section improves upon the p-i-n based structure in several aspects. An overview of the advantages of the n-i-n design, processing, and performance is provided in the following section.

Mode Confinement

Two AlAs layers have been added to the original p-i-n heterostructure. The AlAs layers can be thermally oxidized to form Al_xO_y layers, as shown in Figure 3-18, that strongly confine the optical mode vertically, and centers the mode within the dilute core.

Figures 3-26(a-d) display the mode solver simulations of the Gehrsitz algorithm and Adachi method transverse electric and magnetic fundamental modes that are supported by the n-i-n heterostructure design. Designs of smaller radius of curvature Y-splitters are made possible by the stronger mode confinement.

Applied Voltage Requirements

The V_π of the n-i-n Al_xO_y modulator structure is listed in Table 3.8. The high index of refraction and tight mode confinement are responsible for the nearly threefold improvement in driving voltages over those presented for the p-i-n structure, resulting in a $V_\pi L = 1.98$V-cm for the n-i-n MOS structure. The strong mode confinement reduces the ridge height, t_g, comparably lowering the applied voltage. The calculated values assume that the optical mode and the applied electric field completely overlap, that is Γ=1.

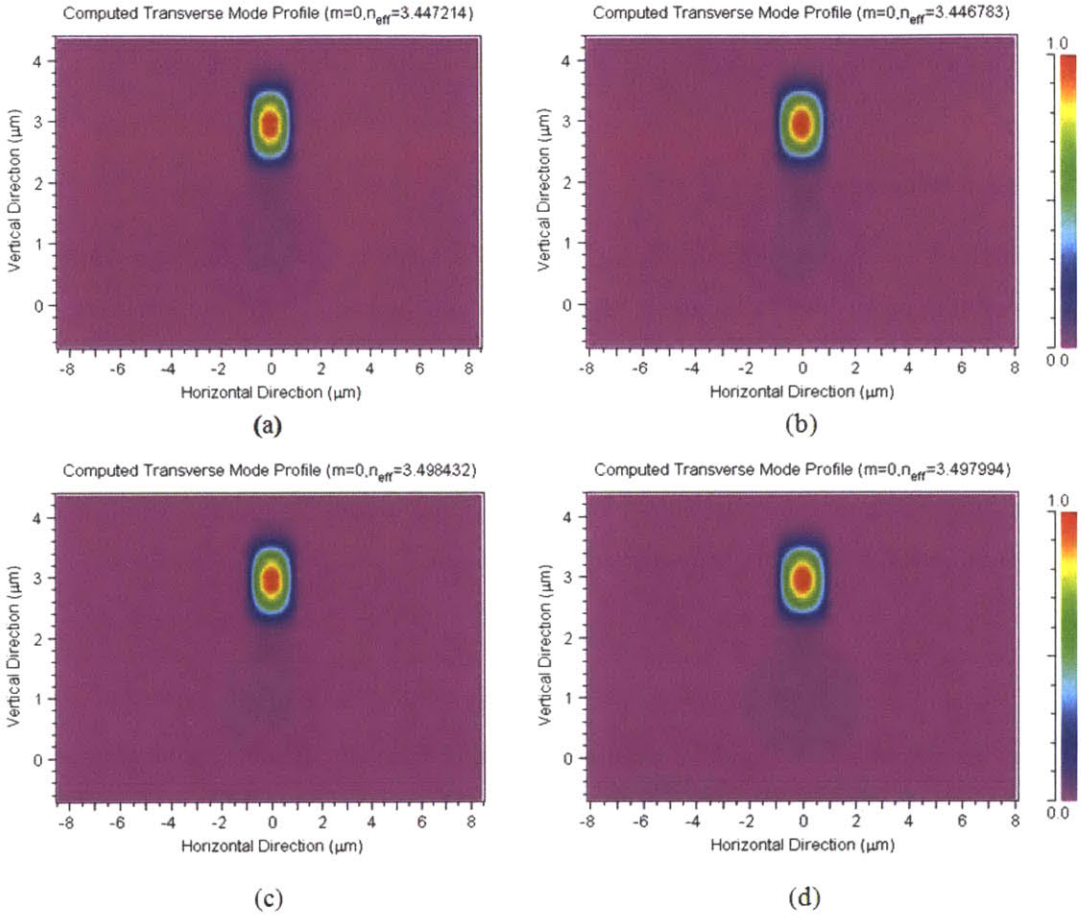

Figure 3-26: (a)Transverse electric and (b) transverse magnetic fundamental mode RSoft BeamPROP simulations based on the Gehrsitz algorithm, and (c) transverse electric and (d) transverse magnetic fundamental mode RSoft BeamPROP simulations based on the Adachi method.

Table 3.8: Calculated values of V_π at λ=0.8μm for the $Al_{0.17}Ga_{0.83}As/Al_{0.27}Ga_{0.73}As$ MOS devices of various Mach-Zehnder arm lengths oriented in the $< 011 >$ direction. This calculation assumes an $r_{41} = 1.44 \cdot 10^{-12}$ m/V, corresponding to the behavior of a bulk GaAs semiconductor modulator. Theoretical values are provided for both Gehrsitz and Adachi index of refraction calculations 3.3.2.

Device Length (mm)	3.0	4.5	6.0	7.5	9.0	10.5
Device Voltage - Gehrsitz n = 3.447 (V)	6.62	4.42	3.31	2.65	2.21	1.89
Device Voltage - Adachi n = 3.498 (V)	6.34	4.23	3.17	2.54	2.11	1.81

Device Processing

Growth of low Al content $Al_xGa_{1-x}As$ layers by MBE is simpler than the deposition of a combination of high Al content $Al_xGa_{1-x}As$ and $In_xGa_{1-x}P$ layers. Furthermore, the near-uniform material composition of the active region eases the RIE process, whereas $Al_{0.8}Ga_{0.2}As$ and $In_{0.53}Ga_{0.47}P$ were found to etch at different rates. While the oxidized AlAs layers confine the vertical movement of the optical mode, the 2.175μm lower cladding layer was made considerably thicker than in previous designs as an additional precaution, preventing the mode from coupling to the substrate.

3.4 Summary

The benefits of strong mode confinement, ease of fabrication, and elimination of p-type related optical losses offered by the novel n-i-n heterostructure motivate its adoption over the p-i-n heterostructure. The electrical performance of the n-i-n MOS structure has been verified by simulating the conduction band and potential response of the structure to applied voltages and comparing the results to measured capacitance-voltage values. As the voltage applied across the heterostructure is increased, the near-intrinsic dilute core depletes and a field across the core is observed.

The mask set developed for the $In_{0.47}Ga_{0.53}P/Al_{0.8}Ga_{0.2}As$ structure accommodates the n-i-n heterostructure design as well with the exception of the MMI power splitters. The modulator fabrication process remains identical for both epitaxial structures with the exception of an added oxidation step after the second semiconductor etch and prior to planarization. While the n-i-n design improves over the p-i-n device operation, fabrication processes play an equally large role in the success of device development. To achieve

optimal device performance, adequate processing methodologies that are compatible with the heterostructure and device design must also be created and assessed through optical measurements of fabricated devices.

Chapter 4

Fabrication and Process Development

The fabrication of broadband modulators at λ=0.8μm necessitates the development of specialized processes. This chapter discusses the creation of a self-aligned mask set, a significant advancement over the previous mask design, that leads to an improvement in the performance of optical modulators that are formed in GaAs/$Al_xGa_{1-x}As$ materials. The fabrication of a generation of MOS, n-i-n modulators is described, and the optical characterization and analysis of the results are offered. Based on observations during testing, changes in the fabrication process were implemented to improve the device performance. While some aspects of the processing methodologies are provided in this chapter, a more detailed explanation of the general fabrication methods and of the process flows that were designed for the creation of broadband modulators are available in Appendices A and B respectively.

4.1 Generation of a Self-Aligned Fabrication Mask Set

The power at the output of an ideal and lossless waveguide is equivalent to the input power, such that:

$$P_{in} = P_{out} \tag{4.1}$$

However, waveguides are typically not ideal and not lossless. Light traveling within the waveguide experiences a degree of attenuation, and for that reason, care must be taken in

creating a fabrication process that does not enhance or further contribute to optical losses (see Section 3.1.1 for an overview of optical losses).

Producing low-loss waveguide modulators with the mask set proposed in Section 3.2.3 is problematic for a variety of reasons. First and foremost, the Mach-Zehnder arms that were defined in the first mask step must be aligned separately to power splitters and straight passive waveguides in a second photolithography process. Even slight misalignment of the MZI and power splitter components, as demonstrated in Figure 4-1, leads to significant optical transmission losses and an unsuccessful fabrication process. Unfortunately, perfect global alignment (in which devices in all areas of the wafer are aligned) is very difficult to achieve with standard microscope objectives and degrees of freedom of x, y, and θ. Therefore misalignment is an inevitability, rather than a possibility, and calls for higher resolution lithography tools and objectives, or a creative solution.

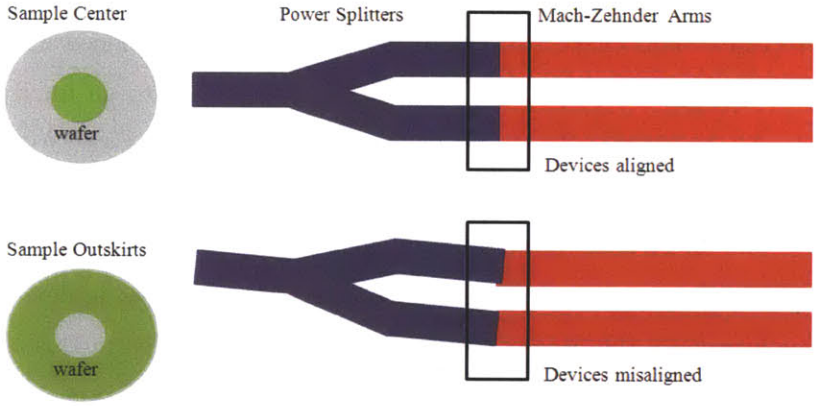

Figure 4-1: An illustration of the challenges associated with component alignment. While components may appear to be locally aligned, global alignment in all degrees of freedom - x, y, and θ - is limited by the sensitivity of the optical aligner and resolution of the objectives, and is much harder to achieve.

A self-aligned fabrication process and mask set was developed to minimize coupling losses at the passive/active coupling intersections. By defining the passive waveguide components and power splitters, as well as the powered MZI arms in the same photolithography step, critical alignments over the full length of the wafer (5.2cm) and optimal coupling of the optical mode throughout the length of the modulator are guaranteed. The initial pho-

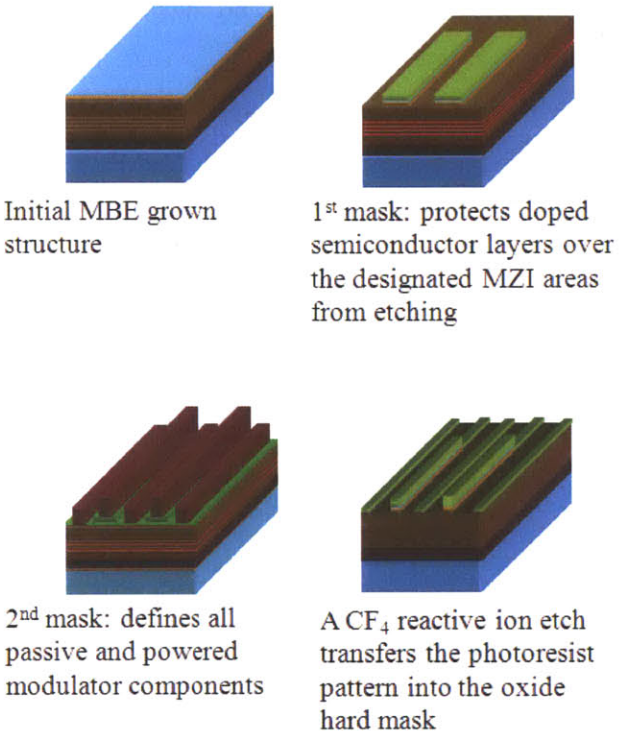

Figure 4-2: Illustration of the self-aligned fabrication process. The first lithography process defines large rectangular shapes that protect the MZI doped semiconductor areas from etching. The second photolithography step forms all modulator device components. Alignment between the large rectangular areas and the devices is far more tolerant than a sensitive alignment between two independent sets of devices, resulting in a more reproducible process.

tolithography step, exhibited as an illustration in Figure 4-2, forms large protective hard mask rectangles (13μm in width, 3mm-10.5mm in length) over the areas of doped semiconductor where the modulator arms will be defined by the following lithography mask. An etch removes all uncovered doped material, and a subsequent lithography process establishes all of the passive and active modulator components simultaneously, making the alignment between the large rectangular areas and the devices far more tolerant than a sensitive alignment between two independent sets of devices. The self-aligned process results in a more reproducible photolithography process.

The rectangle dimensions are designed to provide an error margin of 3μm in aligning. Moreover, the self-aligned mask set improves the device's top-metal contact quality by protecting the doped semiconductor layers and preserving their integrity until the final metalization takes place.

4.2 Preliminary Fabrication of n-i-n Modulators

With the creation of a second (Generation 2) mask set, a novel, complementary fabrication process was developed that addresses the disadvantages and difficulties that were observed in the processing of the $Al_{0.8}Ga_{0.2}As/In_{0.53}Ga_{0.47}P$ modulators. A first set of MOS, n-i-n waveguide modulators were produced and characterized. The fabrication techniques, measurement results and subsequent analysis are detailed in the following section.

4.2.1 Fabrication

Processing of the first generation of n-i-n modulators commenced with the deposition of a high-frequency, 200nm-thick SiO_2 etch-mask by PECVD on the 2" MBE grown wafer. The deposition was followed by a positive photolithography step using AZ5214 resist to define the large rectangles. A CF_4 reactive ion etch removed the exposed areas of the SiO_2 layer, resulting in 13μm-wide rectangles of oxide ranging in length from 3mm to 10.5mm that protect the areas that are designated for the MZI arms. After stripping the photoresist, an optimized HBr RIE removed the top doped semiconductor layers above the exposed passive waveguide areas at a rate of approximately 400nm/min.

A second PECVD 300nm-thick layer of SiO_2 was deposited as a hard-mask in preparation for the second photolithography step. The next, negative lithography step establishes

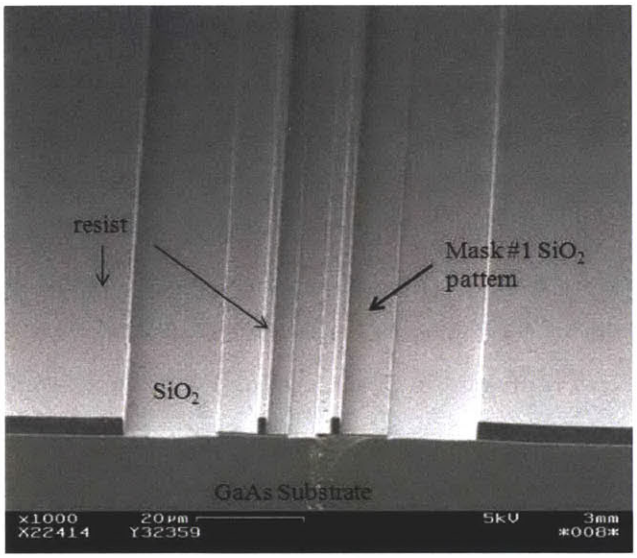

(a)

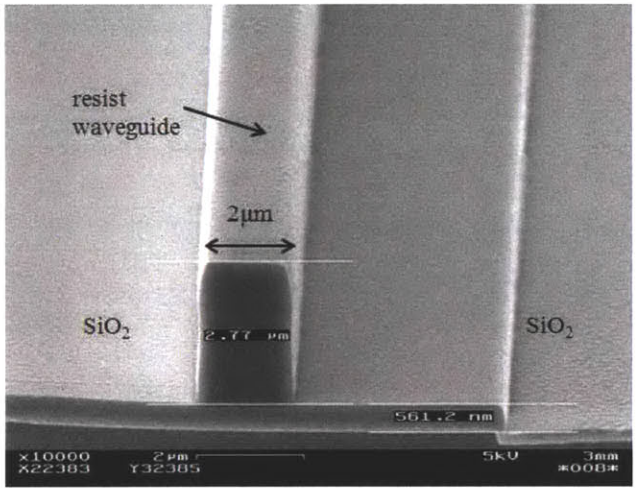

(b)

Figure 4-3: Cross-sectional scanning electron micrograph (SEM) of (a) MZI arms defined in photoresist and (b) of a magnified view of a MZI photoresist pattern. The pattern is aligned to SiO_2 rectangles that were defined during the first photolithography process.

all modulator components and is challenging due to both the varying topography across the wafer, and to the diversity in component construction and dimension. NR7-3000P, a 3μm-thick, RIE-resistant, negative photoresist was used to minimize the sidewall roughness in subsequent pattern transfer steps. The unusual thickness of the resist is desired both for etch resistance as well as to reduce errors in lithography resulting from uneven topography, gaps between the mask and wafer, and other non idealities [98]. The NR7-3000P photoresist was baked at 150^{o}C for 60sec, exposed with a high dosage and then baked a second time at 100^{o}C for 60sec prior to development in resist developer RD6. SEM Figures 4-3(a) and (b) display the pattern of MZI arms in photoresist on top of the oxide rectangles.

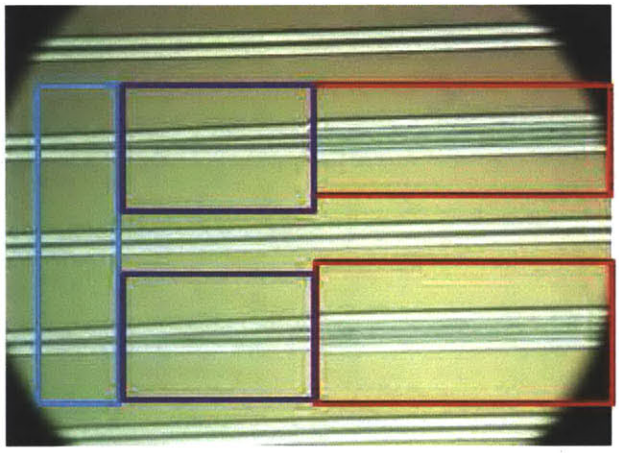

Figure 4-4: Microscope image of modulator devices after the oxide RIE. Passive waveguides (blue box) lead into a Y-splitter (purple box) which evenly divides the power between two MZI arms (red box). As the components are defined simultaneously, they are perfectly aligned with each other.

Pattern transfer into the oxide proceeded with an oxide RIE at 10mT and 15 sccm of CF_4. The microscope image in Figure 4-4 offers a top view of the photoresist modulator components after the oxide etch. The resist was removed by an ultrasonic bath in acetone and 20 min in 100^{o}C resist remover RR4. A 3μm-deep, anisotropic III-V inductively-

coupled plasma reactive ion etch (ICP-RIE) formed the waveguide ridge. An anisotropic, or directional, etch is desired in creating straight, smooth, consistently-wide waveguide sidewalls. To achieve anisotropy, the wafer was etched with $Cl_2/SiCl_4/Ar$ at flows of 0.5 sccm/10 sccm/50 sccm, a pressure of 3mT, and a plate temperature of 100°C. Once the ridge is formed and the AlAs layers exposed, the AlAs films within the ridge were oxidized in a 435°C wet steam ambient at a lateral oxidation rate of 1.6μm/min.

The spin-on dielectric, Hydrogen SilsesQuioxane (HSQ), utilized in the passivation of the p-i-n modulators was insufficiently thick and could not be built up with multiple spin due to stress in the layers. While the HSQ filled the semiconductor trenches, it could not create a planarized surface. Instead, the uneven topography of the n-i-n modulator devices on the wafer was planarized with 3022-46 BenzoCycloButene (BCB), a spin-on insulator with a low dielectric constant that is composed of carbon and silicon. The 3μm-thick layer is spun on at 2500 rpm for 25 seconds and hard-cured in a N_2 ambient at 250°C for one hour. To encourage an even RIE of the BCB, the fourth lithography mask, which patterns 50μm-wide rectangular areas over the MZ arms for the evaporation of contacts, was employed. A 1μm-thick SiO_2 layer was deposited by PECVD over the BCB, and photolithography was performed with the fourth lithography mask. After development of the photoresist, the pattern was transferred into the SiO_2, which in turn was used as a hardmask to protect outlying areas of BCB that are not necessary to etch. The BCB was etched back [Figure 4-5(a)] to expose the MZI arm ridges at a rate of 120nm/min with a CF_4/O_2 RIE with flows set at 16 sccm/8 sccm and at a pressure of 15mTorr. Once exposed, the SiO_2 hard-mask atop the ridges was stripped using a dip in hydrofluoric acid [Figure 4-5(b)] in preparation for the deposition of metal contacts.

The fourth lithography process employed NR7-1500PY image reversal resist that is characterized by a negative angle in the photoresist structure after development. Following the evaporation of the n-type Ge/Au/Ni/Au ohmic contact stack of thicknesses 30nm/60nm/30nm/300nm, the specialized lift-off resist was dissolved in acetone, leaving behind 128μm-wide top electrodes.

Backside processing of the wafer involved thinning, or lapping, of the substrate to a thickness of about 160-180μm to encourage a clean cleave and straight facets. Once lapped, the wafer backside was metalized with an ohmic contact stack of Ge/Au/Ni/Au with thicknesses of 30nm/60nm/30nm/200nm. The front and backside contacts were annealed at

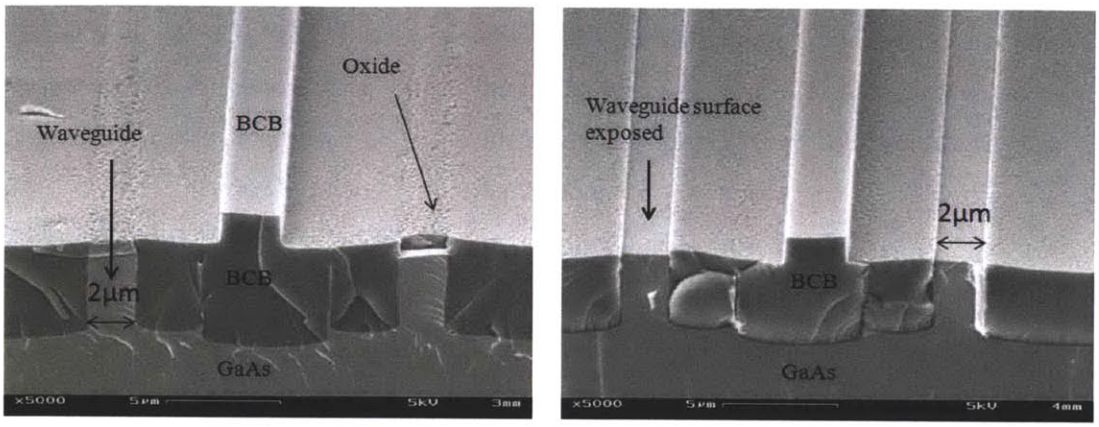

(a) (b)

Figure 4-5: Cross-sectional SEMs of (a) a sample following the etch-back of the passivating BCB, exposing the oxide hard mask on top of the MZI arms, and (b) a sample following a hydrofluoric acid wet etch that removes the oxide hard mask from the MZI arms. In this condition, the ridge waveguide is ready for top metalization.

390^{o}C for 5 minutes in an annealing furnace and devices were thereafter cleaved to produce approximately 15mm long dies that were mounted with a film of indium onto a small copper block for testing.

4.2.2 Optical Characterization

Characterization of the modulators, carried out with the setup that was introduced in Section 3.2.5, involved both passive and powered operation of the modulators. To passively measure the devices, a 780nm diode laser source was passed through a polarizer to remove the transverse magnetic (TM) polarization before being coupled into the device. The TE light was coupled in and out of the modulator device using lensed fibers, and the output of the device was measured with an infrared camera or an OSA depending on the measurement. Using a lensed fiber, collected light was directed to an optical spectrum analyzer (OSA) that was synchronized to the laser source, so that the optical transmission as a function of wavelength could be measured.

A scanning electron microscope image of the output waveguides of a Y-splitter is pre-

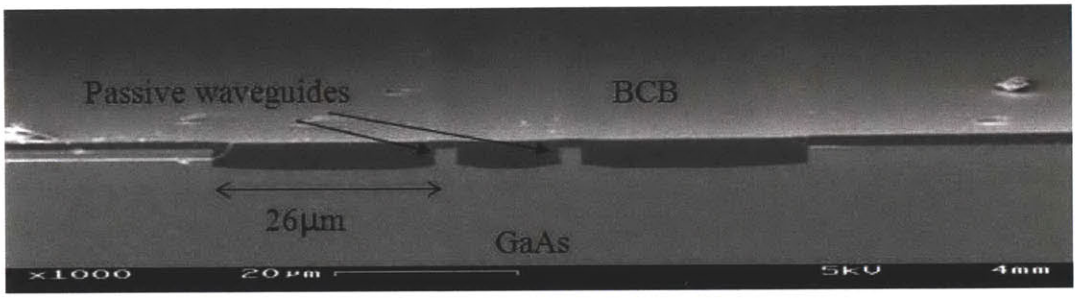

(a)

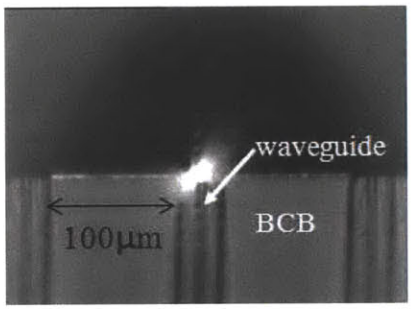

(b)

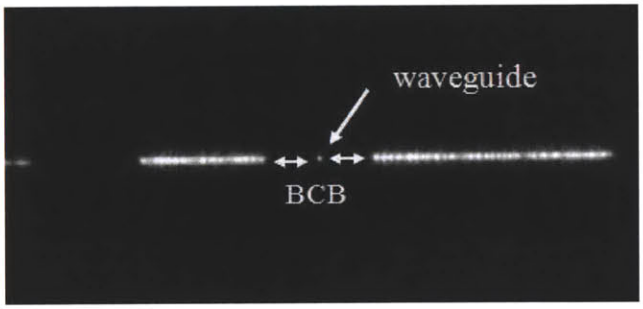

(c)

Figure 4-6: Fabrication and passive testing of an ultra-broadband modulator. In (a) passive waveguides of an open-ended y-splitter are visible. (b) and (c) present the top end and facet end views, respectively. Coupling of light into the waveguide from the laser is not ideal as light is guided in semiconductor areas adjacent to the waveguide.

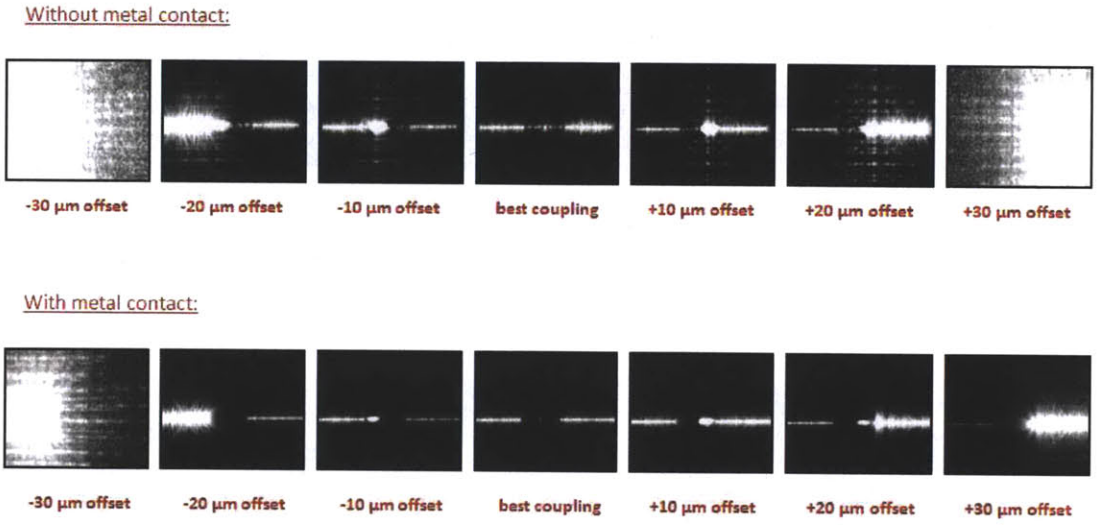

Figure 4-7: Captured images of the output facet of straight waveguides with and without overlaying metal contacts. The images also demonstrate coupling of light into areas adjacent to the ridge waveguide, and simultaneous guidance of light in several semiconductor regions.

sented in Figure 4-6(a). Test devices - straight waveguides and single Y-junctions - were included in the mask set to aid in determining the quality of the fabrication. Testing of the straight waveguides on the fabricated wafer exhibited successful guided light across the 15mm-long device, as shown in the output facet views of Figures 4-6(b) and (c). In addition, light was coupled into a variety of waveguides, both active (equipped with metal contacts) and passive (without metal contacts) to determine if the presence of metal enhances optical losses. Figure 4-7 demonstrates the results of optical testing on both types of waveguides. Though the metal contacts did not interfere with optical mode propagation, the light undesirably coupled into and was guided by the semiconductor areas adjacent to the waveguide despite optimization of coupling between the input fiber and the waveguide.

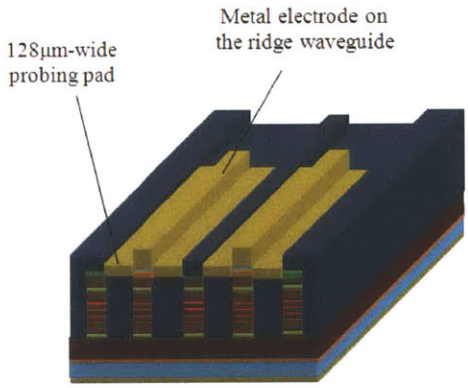

Figure 4-8: Illustration of a fabricated n-i-n MOS modulator. The top side electrodes extend across the ridge waveguide, and are tested by probing the metal at both sides of the waveguide and identifying the associated resistance.

Despite achieving light guidance over a 15mm-long waveguide and determining that the optical mode and metal contacts do not interact, optical losses of -60dB were significant, and led to output power levels too close to the noise floor to be quantified. Powered, or active, testing involving the application of voltage to the device metal contacts, was impeded by the high losses. While modulator operation through destructive or constructive interference could not be qualified, metal connectivity across the electrode was examined by probing the metal pads on either side of the ridge waveguide, as portrayed in Figure 4-8. The electrodes were not connected across the waveguide, and a visual inspection revealed a tear in the metal layer at the waveguide/trench junctions not observed before backside processing.

4.2.3 Analysis of Measurement Results

Three areas of concern have been identified with regard to the optical power loss that was observed in testing:

- Light propagation within the BCB and coupling into adjacent semiconductor areas
- Optical power loss of the optical mode during propagation
- Potential scattering losses at the $Al_{0.27}Ga_{0.73}As/Al_xO_y$ interfaces

The issues that have contributed or led to the prevalence of these losses are presented and discussed in this section.

BCB-Related Losses

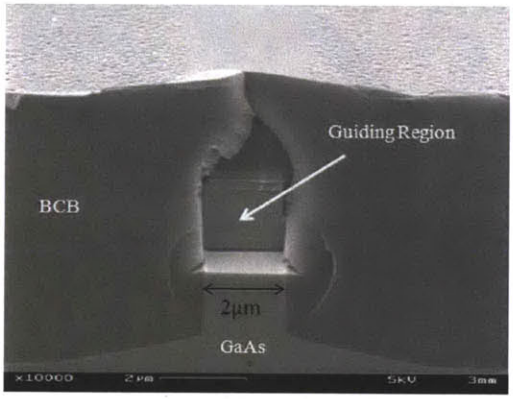

Figure 4-9: Facet view scanning electron micrograph of a ridge waveguide surrounded by BCB. The recessed facet hinders optical coupling, causing light to scatter into the BCB and propagate to other areas on the sample.

The SEM in Figure 4-9 provides a facet view of a straight, non-metalized waveguide from the tested wafer. The BCB-passivated waveguide has broken off at the lower Al_xO_y interface, and while the lower portion of the ridge waveguide remains intact, the guiding core is recessed. Though not all of the waveguides displayed the same damage (see Figure 4-6), the occurrence was prevalent.

The inflicted damage took place during the cleaving process, hence it was inferred that the cleaving-induced stress in the surrounding thick BCB (up to 3μm above the ridge in most areas of the wafer) was transferred to the weakest point in the ridge waveguide - the Al_xO_y interface.

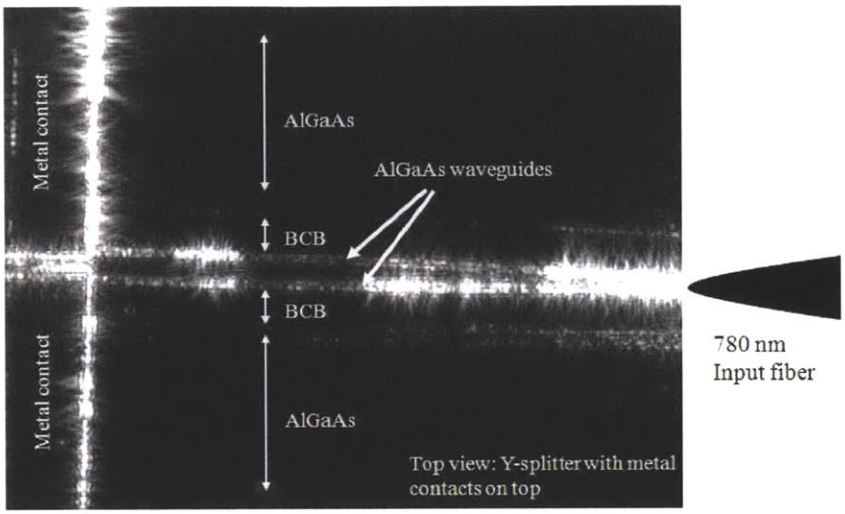

Figure 4-10: Top view of the scattering losses in a Y-splitter and MZI arms that are covered by metal contacts.

The 780nm lensed fiber has an associated depth of focus of 7μm for the 2μm optical mode. The recessed core is an obstacle to successful coupling of light into the waveguide as it increases the distance that is required in focusing the light into the waveguide. Beyond the focal point, the light scatters in this instance, into the surrounding BCB layers. The BCB propagates the light until encountering adjacent semiconductor areas, at which point some or all of the optical power (depending upon the angle of incidence) is transmitted into, and is guided within, the outlying semiconductor regions around the waveguide.

Along with optical guidance by the BCB and coupling of light into adjacent semiconductor regions, irregular scattering was observed along the waveguide. The scattering that is visible in Figure 4-10, could be a result of sidewall roughness, or also of a mode that is excited and guided above the waveguide core. An OptiBPM Simulation (Figure 4-11) of the waveguide structure with a 235nm thick upper cladding of $Al_{0.27}Ga_{0.73}As$ on top of a 40nm

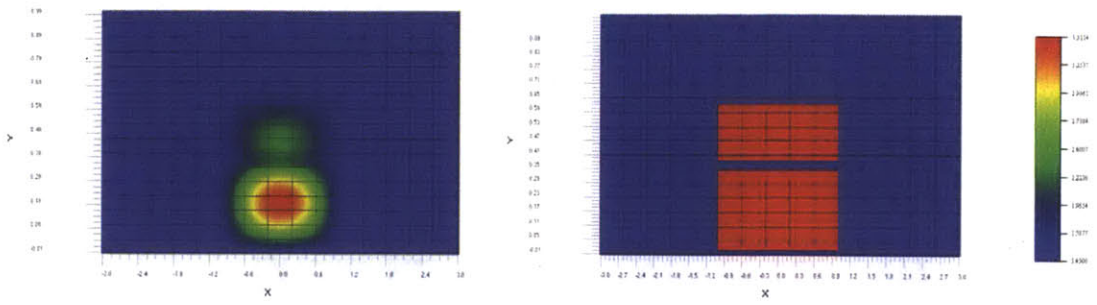

Figure 4-11: OptiBPM simulation of modes supported in both the dilute core and in the upper cladding layer.

thick Al_xO_y layer, capped with an SiO_2 mask layer and surrounded with BCB indicates that a mode can propagate within the region of the upper cladding layer. The light coupled into this smaller waveguide by the same mechanism with which the mode coupled into the BCB and propagated through it and other semiconductor regions nearby. Without contending with the damage that is caused by the cleaving of BCB, which constitutes a significant loss detrimental to the operation of the modulator, achieving optimal fiber-to-waveguide coupling is not possible.

Fabrication-Related Losses

Scattering due to sidewall roughness is a common source of power loss in semiconductor waveguides. The issue is even more pronounced in curved features, such as Y-splitters and ring resonators, as the modal field shifts outwards within the waveguide as the radius of curvature is decreased [99]. Sidewall morphology is determined by pattern transfer and RIE quality, but can also be a result of hard mask degradation [100]. SEM images in Figure 4-13 reveal that the erosion of the SiO_2 hard mask during the ICP-RIE process step led to the unwanted removal of an area approximately 150nm x 600nm (WxH) in size off the side of the guiding dilute core. A defect of these dimensions can be responsible for significant power loss, and detrimental if present over the full length of the light propagation path.

Erosion of the hard mask can be minimized by adjusting the ICP-RIE voltage, but such an approach comes at the expense of directionality and anisotropy. Instead, the thickness of the hard mask can be increased to ensure that a sufficient protective layer remains by

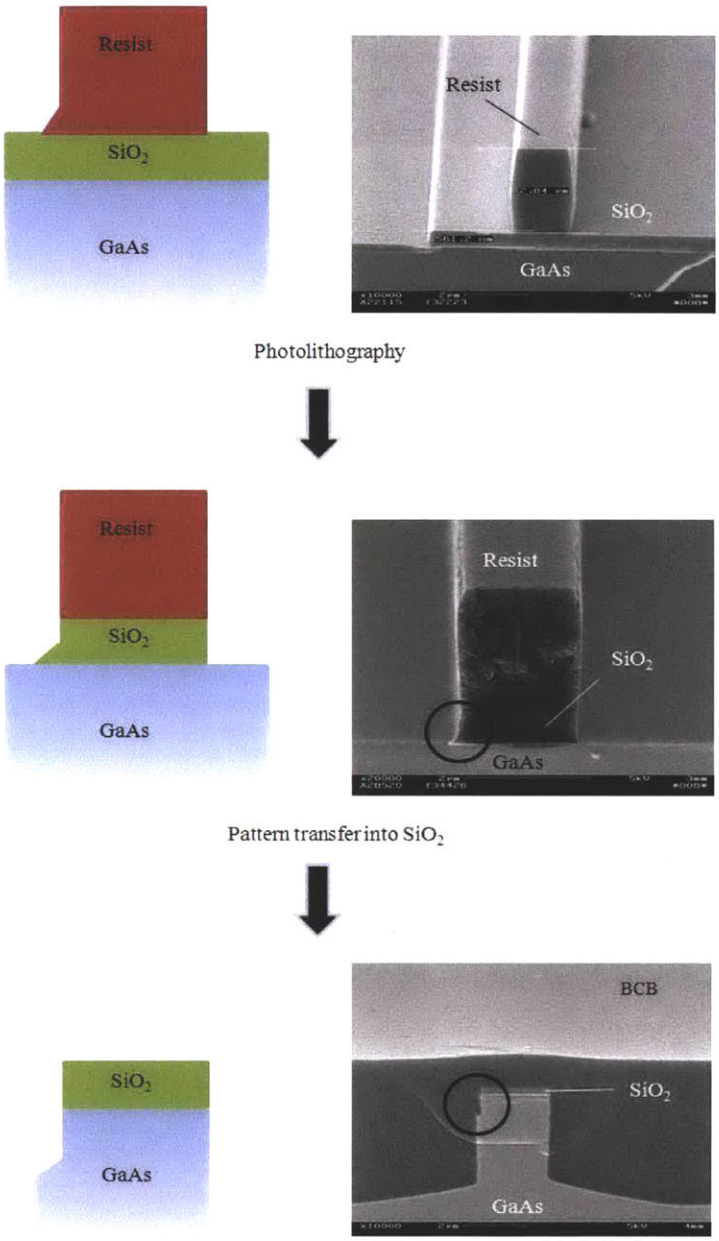

Figure 4-12: Illustration of the hard mask erosion process during pattern transfer by the inductively-coupled plasma reactive ion etch (ICP-RIE). A gap between the mask and wafer creates an uneven pattern in the waveguide, which then masks an area of the oxide in the course of a CF_4 RIE. As the III-V material is removed, the thin oxide film erodes, leaving behind a deformation in the waveguide.

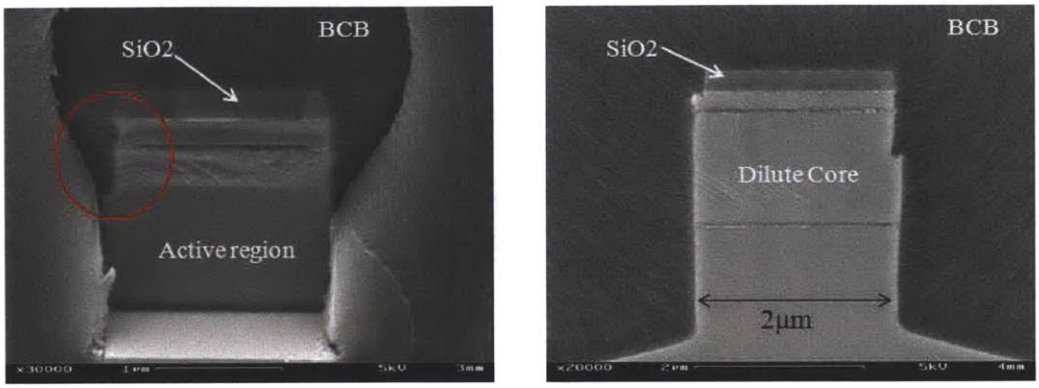

Figure 4-13: Scanning electron microscope images of the ridge waveguide and sidewall defect (outlined in red) caused by the erosion of a thin oxide hard mask during the ICP-RIE process. If present along the waveguide, the defect can be detrimental to the waveguide operation.

the end of the etch. Figure 4-13 indicates that the mask was sufficiently thick and that the selectivity between the semiconductor and the dielectric, at approximately 27:1, is very good. The affected area was likely protected by a very thin layer of SiO_2 that was removed over the course of the semiconductor stack etch and produced by poor pattern transfer from the photoresist mask. The process described above is illustrated in Figure 4-12 schematically and through captured SEM images.

Photoresist patterns are characterized by either vertical or sloped sidewalls. The former is most desirable for pattern transfer purposes as the thinner portions of the sloped profile will be etched away early in the process and not protect underlying areas from the etching procedure [101]. As the SiO_2 film is etched during the CF_4 RIE step, the photoresist mask is also sputtered, even more so in thin areas. In this manner, a tail in the photoresist is transferred into the SiO_2 layer, and into the semiconductor layers thereafter, ultimately producing the rough, uneven edges and deformations seen in the waveguide core and responsible for reduction in optical efficiency.

Discussion of Oxidation-Related Losses

Another potential source of the scattering losses visible over the waveguide in Figure 4-10 is surface roughness at the oxidized AlAs interfaces. Tien developed an expression for the scattering loss, α, of symmetric planar guides [102]:

$$\alpha = \frac{\sigma^2 k_0^2 h}{\beta} \frac{E_s^2 \delta n^2}{\int E^2 dx} \tag{4.2}$$

where σ is the surface roughness, k_0 is the free-space wavenumber, δn^2 is the difference in indices squared between the guiding and cladding layers, and h is the transverse propagation constant in the guide layer. According to Equation 4.2.3, epitaxial scattering loss increases with surface roughness (σ^2) and with index difference $(n_1\text{-}n_2)^2$ between the guiding core and cladding, and is proportional to the normalized optical intensity at the guiding core-cladding interface [103]. Due to the strong dependence of losses on surface roughness, the roughness associated with the AlAs oxidation should be examined and quantified.

4.3 Optimization of Fabrication-Induced Propagation Losses

Fabrication of modulator components for passive characterization measurements (with the exclusion of top or bottom metal electrodes) was pursued. Several modifications were made to the fabrication process in order to reduce the BCB and fabrication-related losses, and to assess any effects that the oxidized AlAs and BCB passivation layers may have on attenuation of the optical mode power. The contribution of the BCB and oxidation to the severe optical losses would be assessed by an experiment (illustrated by Figure 4-14) devised to process a wafer as follows:

- One quarter of the wafer would not undergo oxidation of the AlAs layer, and would not be planarized with BCB
- One quarter of the wafer would not undergo oxidation of the AlAs layer, but would be planarized with BCB
- One quarter of the wafer would undergo oxidation of the AlAs layer, but would not be planarized with BCB

- One quarter of the wafer would undergo both oxidation of the AlAs layer and planarization with BCB

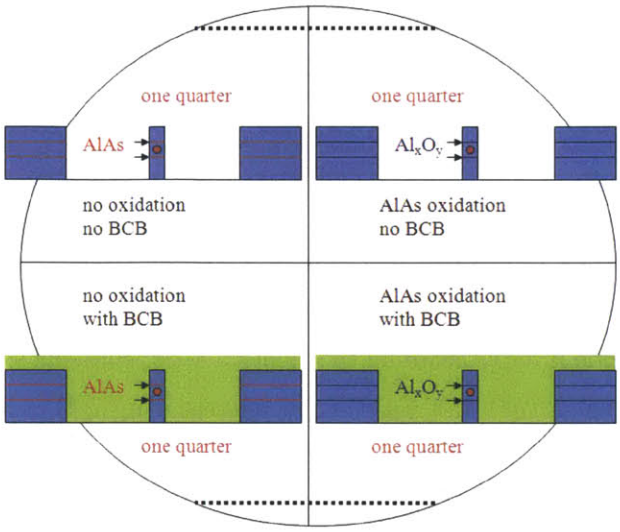

Figure 4-14: Description of the experiment to assess the contribution of AlAs oxidation and BCB planarization to optical losses. Samples are fabricated with all combinations of planarized/unplanarized and oxidized/unoxidized waveguide components.

Testing of the different samples would determine what effects, if any, the BCB and Al_xO_y have on scattering losses and surface roughness. This round of processing addresses the photolithography and cleaving difficulties that were discussed previously, and describes the improvement undertaken to minimize optical losses in the waveguide structure. Results of the optical characterization are provided and examined in detail.

4.3.1 Fabrication of Modulator Components for Passive Testing

Fabrication involved only the first two masks of the self-aligned mask set. Again, the top doped semiconductor layers were removed by a process of SiO_2 deposition, photolithography, RIE of the oxide layer and pattern transfer into the semiconductor. A H_2SO_4:H_2O_2:H_2O (1:1:40) wet-etch removed the top doped semiconductor layers over the exposed passive waveguide areas at a rate of approximately 120nm/min, and the wafer was then covered with a high frequency, PECVD layer of SiO_2. The wet etchant was adopted instead of the RIE or ICP-RIE processes that were previously employed due to the slower etch rate and the non-critical nature of the etch step.

The second mask lithography process, defining all modulator devices, was significantly altered. The patterning of 14.5mm-long, 2μm-wide waveguides is extremely challenging due to:

- Uneven topography (both vertically and horizontally along the wafer)
- Contact lithography leading to variations in exposure quality
- Maintaining the 2μm ridge width throughout the length of the waveguides
- Achieving a 3dB power split with Y-splitter devices
- Component diversity in construction and dimension

Thick, NR7-3000P photoresist was once again chosen, but the process was greatly modified and diverges significantly from the factory specifications. The soft bake was adjusted to 80^{o}C for 3min and the cross-linking bake was set at 110^{o}C for 70sec.

Table 4.1: Modified NR7-3000P negative photoresist process

Step	Original Recipe	Reworked Recipe
Adhesion promoter application	No	No
Spin application photoresist	3 krpm, 40 sec	3 krpm, 40 sec
Hot plate bake	150°C, 1:00 min	80°C, 3:00 min
Exposure dosage	680mJ/cm^2	280mJ/cm^2
Hot plate bake	100°C, 1:00 min	110°C, 1:10 min
Development in RD6	18 sec	13 sec

The exposure dosage was reduced to account for the changes in the bakes. The lower temperature and longer first bake allowed the photoresist to retain more solvent that re-flowed during the second bake. The abundance of solvent led to enhanced contact between the mask and the wafer, which in turn produced more uniform waveguide widths of 2μm along the 15.75mm device with a variation +/- 50nm across 26mm of adjacent waveguides (widths were verified by SEM images of waveguide cross sections). A reduction in sidewall roughness of the photoresist pattern, provided in Figure 4-15, was also attributed to the reflowing of the resist following the exposure step. The ensuing RIE into the underlying SiO_2 film produced a layer without the problematic footing encountered previously (see Section 4.2.3). The lower temperature bakes also eased the resist stripping process, despite the use of the photoresist as an RIE mask material.

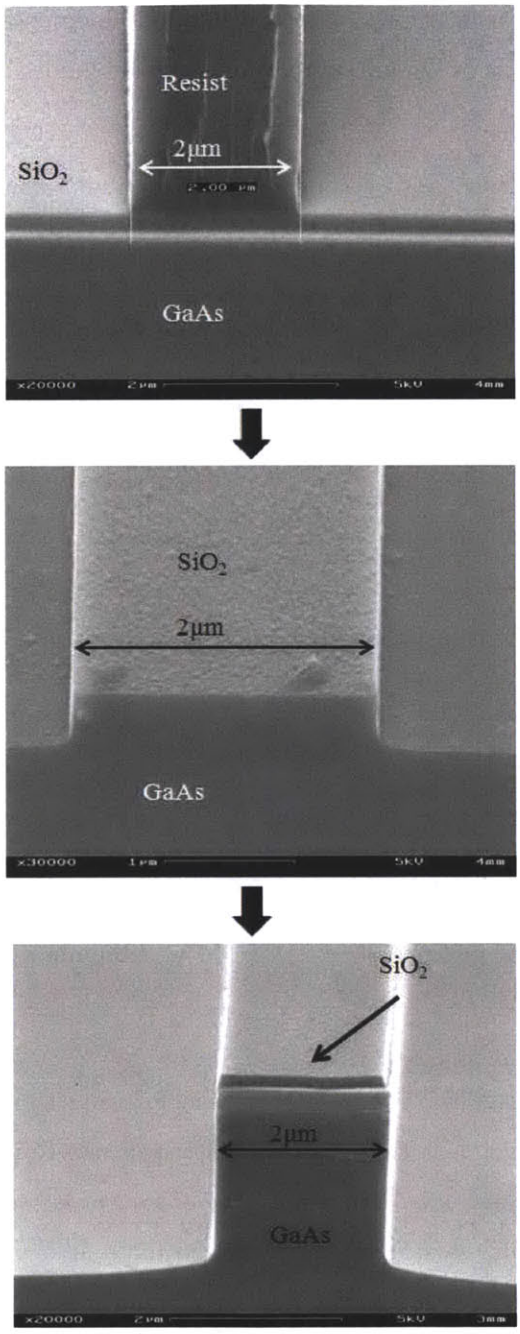

Figure 4-15: Pattern transfer process from the modified-process photoresist to the oxide by RIE, and from the oxide hard mask to the III-V semiconductor stack by ICP-RIE.

After III-V pattern transfer and wet oxidation, the wafer quarters were planarized with BCB and annealed. For the purpose of passive device testing, etch-back of the BCB layer

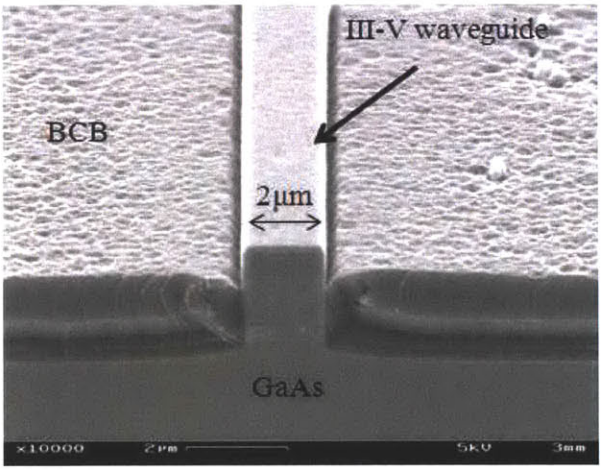

Figure 4-16: Cross-sectional SEM image of a fabricated ridge waveguide device planarized by BCB. Etching of the BCB over the ridge relieves stress during the facet cleave, improving the facet quality and preventing damage to the ridge.

over the MZI arms was unnecessary. Instead, an additional photolithography mask was employed to define the areas over the waveguide facet cleave where BCB will be removed. In the past, cleaves were associated with significant damage to the input and output facet waveguides and created serious difficulty in coupling light to and from the waveguides. Investigations (Section 4.2.3) indicated that the BCB layer residing on the top of the waveguide prior to cleaving caused stress that led to deformation of the waveguide structure during the cleaving process. An additional photolithography mask was designed and used in conjunction with a negative photoresist to expose only the facet-cleave areas to a CF_4/O_2 RIE of the BCB layer. Cleaving of the facets proceeded smoothly, yielding undamaged facets presented in Figure 4-16 to enhance optical coupling. Finally, the wafer was thinned to a thickness of 160μm, the facets were cleaved, and 14.5mm-long dies were placed on copper mounts for testing.

4.3.2 Optical Characterization

Optical testing of the four fabricated quarters was carried out using the apparatus that was detailed in Section 3.2.5. The unoxidized, unplanarized, mounted devices were measured first. An example of the power transmission data that was collected from a straight,

unoxidized, unplanarized waveguide is shown in Figure 4-17. A fiber-to-fiber coupling loss (typically between 7-8dB) was also measured for comparison and completeness. Losses

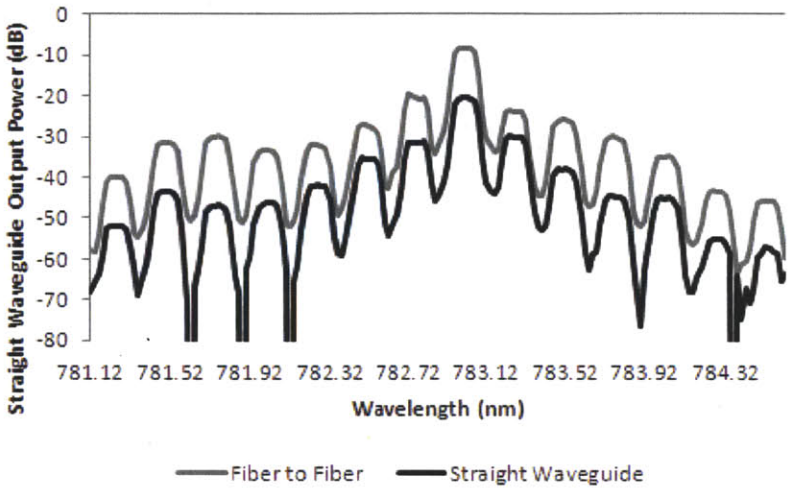

Figure 4-17: Optical power transmission through an unoxidized, unplanarized straight waveguide as a function of the laser wavelength spectrum (in grey) and fiber-to-fiber coupling power (in black).

over the 14.5mm-long sample were measured at -20dB. Excluding 8dB of coupling loss, the optical loss figure for the unoxidized, unplanarized waveguides was 0.827dB/mm.

Next, light was coupled into devices atop the oxidized and BCB-planarized quarter of the wafer. Losses of -21dB were measured by coupling light into a 14.5mm-long straight waveguide and collecting the output power (Figure 4-18). Excluding 7.5dB of fiber-to-fiber losses, the propagation losses of the planarized, oxidized structure is 0.93dB/mm. Light coupled into the waveguide remained tightly confined within and guided solely by the structure due to the exposed facets of the waveguide.

The design and fabrication of the Y-splitter devices were verified by coupling light at the input of a single Y-splitter, such as the one shown in Figure 4-19(a). The power was split into two waveguides by the splitter, and was collected at the output of each arm, yielding a successful 3dB power split and -30dB of optical losses along the individual waveguides. The

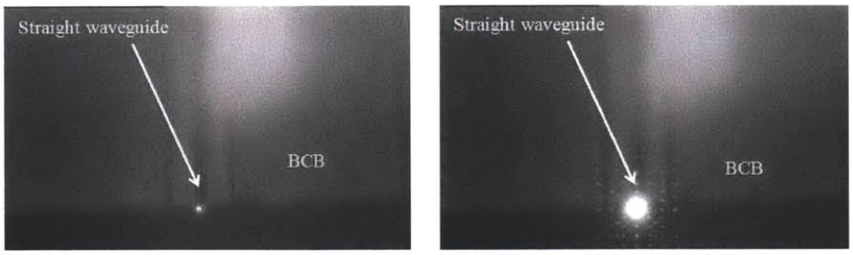

Figure 4-18: Top output facet views of power coupled into a planarized and oxidized straight waveguide. Light is coupled into and being guided only by the waveguide.

recombination of the split signals was further demonstrated by the coupling of light into a full waveguide modulator configuration - a splitter, followed by a straight waveguide section and an inverted Y-splitter, or combiner. Figure 4-19(b) is a top facet view of the output of the passive modulator structure exhibiting the recombined light at the output. Power transmission of -40dB was measured at the output of this device configuration. Finally, the removal of BCB from the input facets prevented the coupling of light into multiple areas of the sample at one time. As shown in Figure 4-20, light is successfully guided only in the section to which it was coupled.

The optical losses that were measured from over 40 straight waveguides on each of the quarters and summarized in Table 4.2 indicate that any roughness in the Al_xO_y layer is largely insignificant and that the BCB planarization process does not significantly and detrimentally affect the optical power. While the remaining fabricated quarters - unoxidized and planarized, and oxidized and unplanarized samples - did not provide an improvement in the optical propagation losses as compared to the other two samples, the respective losses of -26dB and -24dB in the quarters are comparable. Damaged chrome on the second photolithography mask from frequent use, inaccuracies along a hand-cleaved-facet, and defects and difficulties incurred due to the length of these devices hampered characterization of several of the waveguide and splitter devices, and have likely contributed to the measured optical losses. Additionally, while the transmitted power is strong enough for modulation and the fabrication process of the straight waveguide has been successful, the small Y-junction dimensions (down to 200nm at the tip) are not only difficult to replicate with contact lithography but even difficult to define on the mask itself. A less than sharp tip can have a number of adverse effects on the power split, from uneven splitting to additional

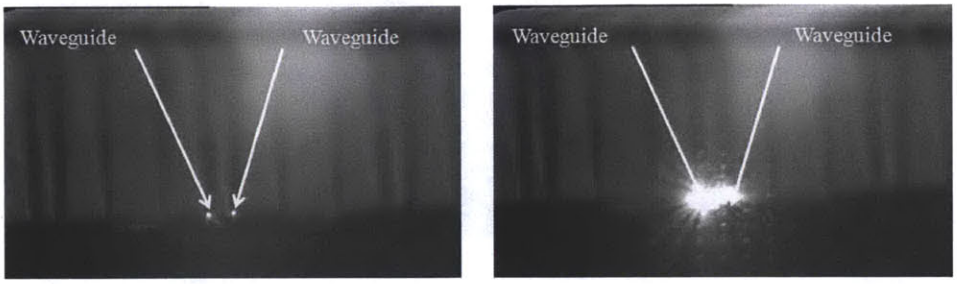

(a)

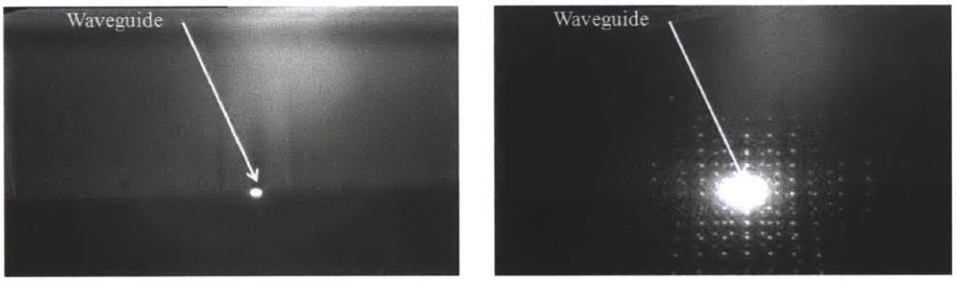

(b)

Figure 4-19: Top facet views of the output of (a) a power splitter device and of (b) a full modulator consisting of a Y-junction splitter and combiner. In (a), low input (left) and high input (right) power is coupled into a planarized and oxidized open-ended Y-splitter. The Y-splitter exhibits a successful 50:50 split between the two output waveguides. In (b), low input (left) and high input (right) power is coupled into a planarized and oxidized Y-splitter followed by non-metalized Mach Zehnder Interferometer arms and a recombining Y-splitter.

power losses in the waveguide. The measurement results in Table 4.2 reflect that the Y-splitters contribute to optical losses if defined by contact photolithography.

Table 4.2: Summary of measured optical power transmission

Sample	Device	Transmitted Power (dB)
Unoxidized, unplanarized	Straight Waveguide	-20
Unoxidized, planarized	Straight Waveguide	-26
Oxidized, unplanarized	Straight Waveguide	-24
Oxidized, planarized	Straight Waveguide	-21
Oxidized, planarized	Y-Splitter Arms	-30 each
Oxidized, planarized	Full Modulator	-40

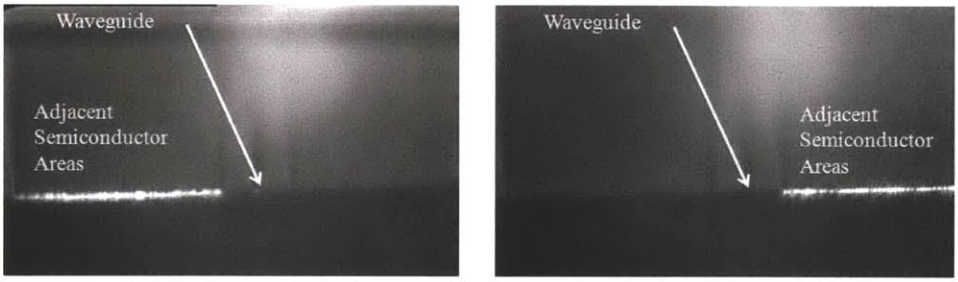

Figure 4-20: Top output facet view of light coupled into the semiconductor areas adjacent to the waveguide modulator. Power is well-confined to the area into which the light is coupled.

4.4 MMIs Based on the MOS n-i-n Epitaxial Structure

The fabrication of passive components verified the capability of the n-i-n metal-oxide-semiconductor design in supporting and propagating an optical mode. However, the small dimensions of the Y-splitter components were difficult to fabricate on both the mask and on the wafer, and were responsible for losses of more than 10dB across the device. This section details the design, simulation and fabrication of 1x2 multimode interferometers that are based on the n-i-n MOS heterostructure.

The deciding factor in MMI design is the length, which can span millimeters in length depending on the index of refraction of the structure and the wavelength of operation. To limit the 1x2 MMI to reasonable dimensions of length and center-to-center distances between the output waveguides, MMI widths of 12μm and 16μm were modeled using the RSoft BeamPROP software package. Simulations performed at λ=0.78μm, shown in Figure

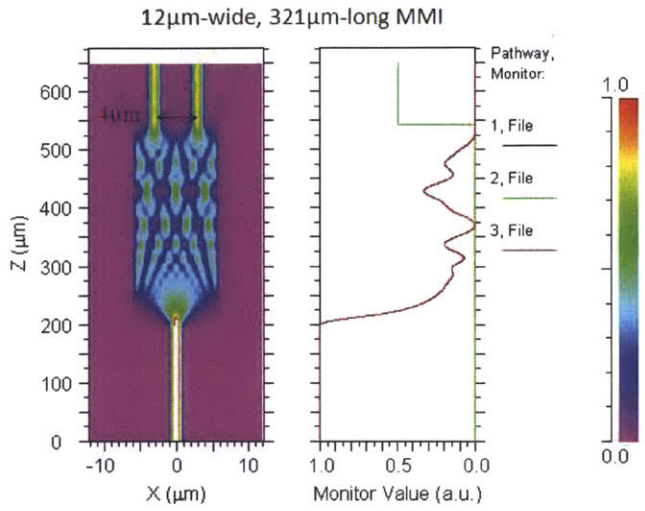

Figure 4-21: BeamPROP-simulated performance of (a) 12μm-wide and (b) 16μm-wide 1x2 MMIs designed to operate at λ=0.78μm. The propagation simulation and the adjacent graph of the power transmitted to the two output waveguides (monitored as Files 1 and 2) indicate that a 3dB split is achieved with a 321μm-long MMI for the former and a 569μm-long device for the later. The center-to-center distance between the waveguides in the shorter and longer MMIs is 6μm and 8μm, respectively.

4-21, determined that a 3dB split between two waveguides is achieved with a 321μm-long device for the 12μm-wide MMI, and with a 569μm-long device for the 16μm-wide MMI.

Table 4.3: Summary of the 12μm-wide MMI theoretical calculations for varying wavelengths of operation, and calculated for both Adachi and Gehrsitz indices of refraction at these wavelengths

Wavelength	Adachi Method MMI Length	Gehrsitz Algorithm MMI Length
λ=0.78μm	326μm	321μm
λ=0.785μm	323μm	318μm

Table 4.4: Summary of the 16μm-wide MMI theoretical calculations for varying wavelengths of operation, and calculated for both Adachi and Gehrsitz indices of refraction at these wavelengths

Wavelength	Adachi Method MMI Length	Gehrsitz Algorithm MMI Length
λ=0.78μm	579μm	569μm
λ=0.785μm	574μm	567μm

Calculations of the MMI length using the equations that are introduced in Section 3.2.3 show sensitivity to the wavelength of operation and refractive indices of the heterostructure materials. The equations yield maximal transmission values at MMI lengths of 321μm and 569μm for the 12μm-wide and 16μm-wide MMIs, respectively, based on the index of refraction of the core as obtained from the Gehrsitz Algorithm. Due to the strong dependence of MMI performance on length, a mask was designed and fabricated to verify the simulations and the theoretical calculations, and to determine the optimal length of multimode interferometers for a 3dB split.

A simulation tracking the power at the two output waveguides of a 16μm-wide MMI as a function of the MMI length is shown in Figure 4-22.

4.4.1 Mask Design

The MMI mask consists of two negative lithography layers, the first layer that is positioned in the bottom half, and the second mask layer that is positioned in the top half of Figure 4-23. The first mask layer defines a variety of components on two identical sets of two die

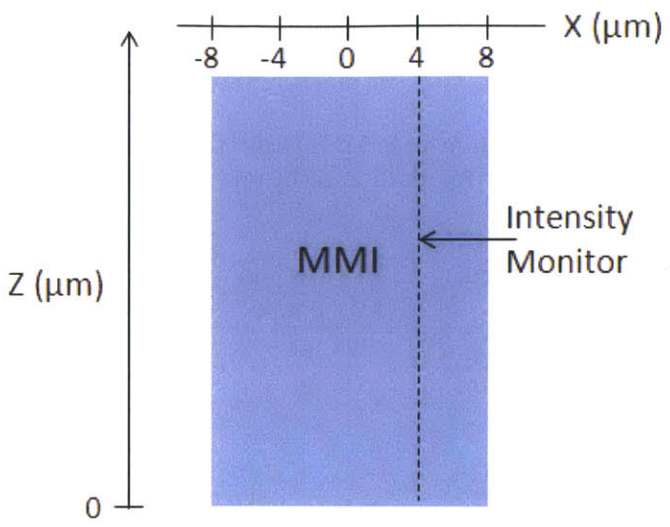

(a)

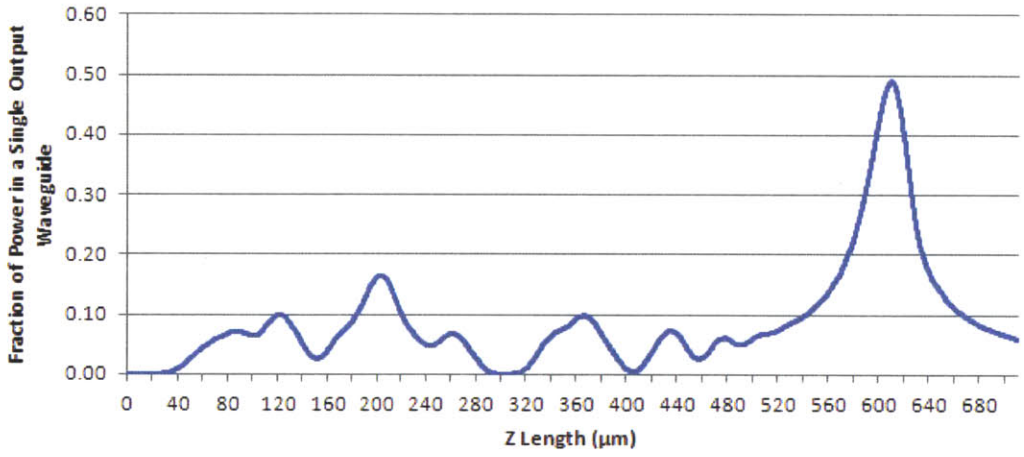

(b)

Figure 4-22: Images of the (a) MMI simulation schematic and the placement of the intensity monitor, and (b) the RSoft BeamPROP simulation of the fraction of power at the output waveguide of a 16μm-wide MMI as a function of the simulation length, z, in μm, as monitored throughout the MMI. According to the simulation, maximal output power is achieved with an MMI length of 569μm.

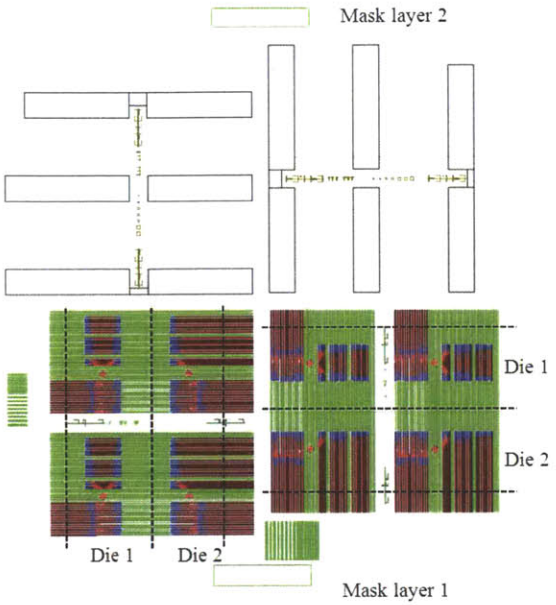

Figure 4-23: MMI Mask consisting of two negative lithography mask layers. The first mask layer (bottom) holds a variety of MMI test structures in two identical sets of two die types, and the second mask layer (top) establishes the area for the BCB facet etch. The die facet cleaves are marked by a dashed line.

types (marked by cleave lines in Figure 4-23) as follows:

- 1x2 MMIs of lengths varying from 293μm-393μm for the 12μm-wide MMI, and from 560μm-660μm for the 16μm-wide interferometers.
- 1x2 MMIs that lead to 2x1 MMIs, of lengths varying from 293μm-393μm for the 12μm-wide MMI, and from 560μm-660μm for the 16μm-wide interferometers.
- Curves of lengths of 300μm and 650μm, corresponding to radii of curvatures of 2.78mm and 6mm respectively, were included to test the ease of fabrication and the effect of the bends on the optical losses.
- 1x2 MMIs with outputs that couple into curves of lengths of 300μm and 650μm, which in turn couple to straight waveguides. The waveguides lead back to 2x1 MMIs through another set of curves.
- 1x2 MMIs of different lengths, cascaded to achieve splitting ratios at the output, designed to more accurately ascertain the optimal MMI lengths.

A magnified view of the dies is provided in Figure B-5 in Appendix B.

The second MMI mask layer shown at the top half of Figure 4-23 is composed simply of alignment marks and large patterns that expose the facets to a BCB etch to facilitate the facet cleave.

4.4.2 Fabrication Process

The fabrication of the MMI components is similar to the process that was described in the fabrication of straight waveguides and Y-splitters outlined in Section 4.3. Processing commences with the deposition of a 300nm-thick dielectric film and a photolithography step using the first mask layer with NR7-3000P photoresist. The pattern defined in the photoresist is transferred into the dielectric hard mask with a CF_4 RIE. An adjustment was made in the RIE process, as the photoresist appeared to sputter off during the RIE, masking the dielectric beyond the dimensions of the previously-formed photoresist pattern (visible in the left image in Figure 4-24), and creating a footing in the dielectric that is problematic for the upcoming ICP-RIE pattern transfer into the III-V stack. While low ratios of 3:17 O_2:CF_4 removed the sputtered photoresist, the etch also caused considerable damage to the dielectric (see middle image in Figure 4-24). Instead, the RIE process cycled between 3-4 minute long etches in CF_4 and short, 15 second bursts of He/O_2 ashing. The small addition of oxygen into the chamber removed sputtered photoresist, preventing the formation of any outlying dielectric footing.

After the ICP-RIE, the AlAs layers were oxidized at 420°C, and the sample was covered in spin-on BCB. Instead of the 3022-46 Cyclotene formulation that was used in previous rounds of fabrication, which spins to thicknesses of 2.4μm-5.8μm, a thicker 3022-57 formulation that spins to 5.7μm-16.9μm was adopted. The BCB formulation was changed because the planarization of previous modulator devices was insufficient and led to uneven surfaces that were difficult to metalize. The planarization ratio, P, a measure of effectiveness in smoothing uneven topology, is defined as

$$P = 1 - \frac{d}{b} \tag{4.3}$$

where b is the height of the feature that is planarized (i.e. a waveguide) and d is the step height over the feature following planarization [104]. Ideally, a planarization ratio of

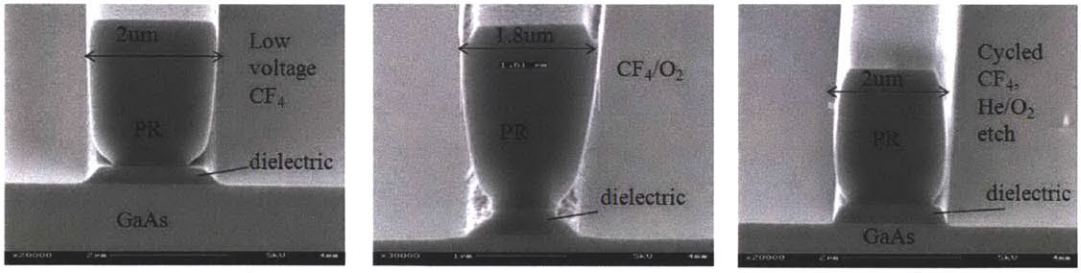

Figure 4-24: Dielectric etches in low voltage CF_4 RIE (left), in O_2/CF_4 RIE with flows of 3sccm/17sccm (middle), and cycling between CF_4 RIE and 15 second bursts of He/O_2 (right). The CF_4 etch sputtered photoresist onto the sample, protecting outlying areas of dielectric and producing a footing. The addition of oxygen was detrimental to the dielectric, resulting in a rough dielectric surface and highly uneven sidewalls. A small amount of oxygen provided by brief ashing steps in between CF_4 etches removed sputtered photoresist from the edges of the feature and eliminated the dielectric footing.

1 is desired, and is highly dependent on feature dimensions and the aspect ratio between the feature height and the BCB spin thickness. According to research by Stokich et al [105], optimal planarization (P>0.9) for features up to 100μm in width is achieved with a polymer-to-feature aspect ratio of 2:1, and there are no benefits beyond such a ratio. With a feature height of approximately 3μm, the waveguides are well-planarized, displaying a planarization ratio of approximately 0.97 with a single spin at 3 krpm or 4 krpm of the thick, 3022-57 BCB formulation.

The BCB annealing process was also altered. Soak steps at temperatures of 100^{o}C and 150^{o}C were introduced to encourage reflowing in the BCB layer prior to full curing. By slowly raising the temperature and holding the sample at lower temperatures, the viscosity of the film is reduced and the film reflows prior to the cure, leading to improved planarization, particularly for wider structures that are often problematic to planarize evenly [105]. Table 4.5 provides details of the original BCB cure and the modified film cure discussed here.

A second photolithography process employing the second mask layer on the MMI mask formed large openings over the facet cleaving areas of the MMI devices. The MMI devices themselves were covered by a 3μm-thick layer of NR7-3000P photoresist. The BCB that was exposed in the facet regions was etched with a CF_4/O_2 RIE with flows set at 16 sccm/8 sccm respectively and at a pressure of 15mTorr. The BCB was removed from the top of

Table 4.5: Modified BCB annealing process

Original Annealing Process	Revised Annealing Process
Flow N_2 >20 scfh for 30 min	Flow N_2 >20 scfh for 30 min
Reduce N_2 flow to 5 scfh	Reduce N_2 flow to 5 scfh
Ramp temperature to 250^{o}C, hold for 60 min	Ramp temperature up to 100^{o}C, hold for 10 min Ramp temperature up to 150^{o}C, hold for 20 min Ramp temperature up to 200^{o}C, hold for 10 min Ramp temperature up to 250^{o}C, hold for 120 min

the input waveguides, and etched down until approximately half the waveguide height was exposed in order to facilitate the facet cleave. After removal of the photoresist in 100^{o}C RR4 resist remover, the sample was mounted for backside processing and lapped to a thickness of 180μm. After wafer thinning, the dies were cleaved, and the samples mounted on copper mounts in preparation for testing. The cleaved output facets of (a) a cascaded MMI device and of (b) a straight waveguide that leads to an MMI are shown in Figure 4-25.

4.4.3 Optical Characterization

Optical characterization of the multimode interferometers was carried out on the optical setup that was detailed in Section 3.2.5. Light that is coupled out of the output waveguides of the MMIs was compared to the output from the straight waveguides both for calibration purposes in determining the losses of the MMI, and to assess the quality of the fabrication and the uniformity of the facet cleave along the sample. Figures 4-26(a) and (b) display the top facet views of the outputs of a 1x2, 16μm-wide, 560μm-long MMI and of a 12μm-wide, 336μm-long MMI with one straight output waveguide and with another output waveguide that leads to a second 1x2 12μm-wide, 343μm-long MMI, resulting in three waveguides at the output.

Measurements that were obtained from the 16μm-wide MMIs are presented in Figure 4-27 (in blue), overlaid on top of the theoretically-calculated curve of the fraction of output power per output waveguide as a function of MMI length (in grey). The theoretical curve assumes an index of refraction of $n = 3.48$ (calculated at a wavelength of λ=0.785μm) and operation at a wavelength of λ=0.785μm, the operation of the laser employed in the characterization of the MMIs. Despite two outlying points that are likely the result of

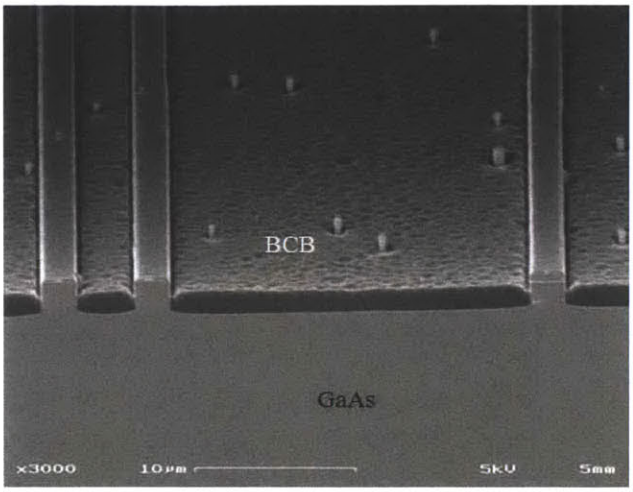

(a)

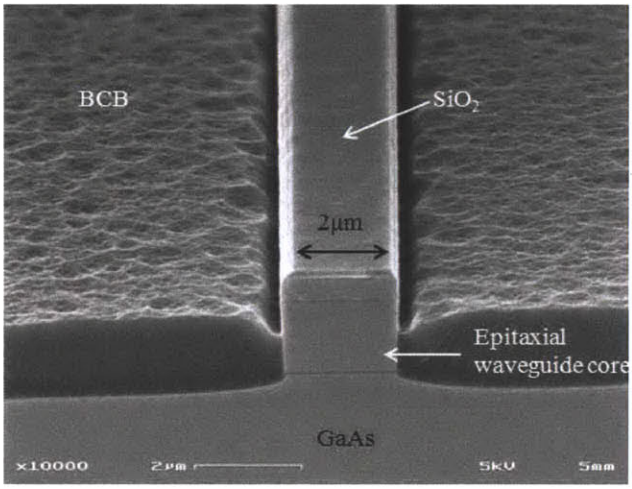

(b)

Figure 4-25: Scanning electron micrograph images of (a) the output waveguide facets of a 1x2 MMI with one output waveguide that leads to another 1x2 MMI (resulting in three output waveguides in total) and (b) magnified facet view of an output waveguide of a 1x2 MMI.

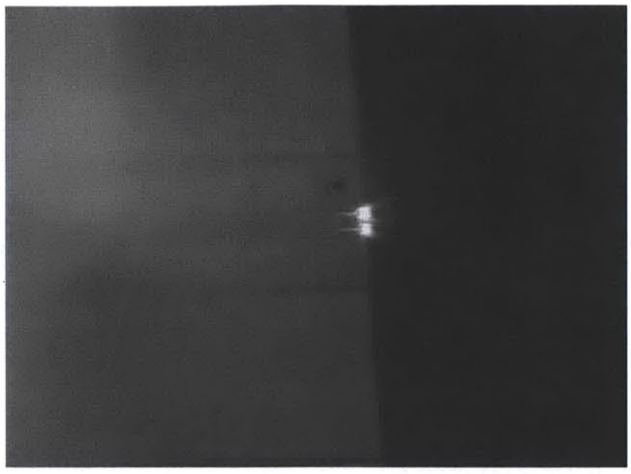

(a)

(b)

Figure 4-26: Camera-captured top facet views of the output of (a) a 16μm-wide, 560μ-long 1x2 MMI power splitter device and of (b) a 12μm-wide, 336μm-long MMI with one straight output waveguide and with another output waveguide that leads to a second 1x2 12μm-wide, 343μm-long MMI, resulting in three waveguides at the output.

non-ideal coupling or damaged facets, the measurements adhere to the theoretical curve and indeed expect that the 3dB power split occurs at the theoretical value of a 567μm-long MMI (with the Gehrsitz indices of refraction and at a wavelength of 785nm). An even power split was obtained at an MMI length of 560μm, with measured power transmission

at each output waveguide of -3.5dB relative to the output of a straight waveguide (no power splitting), corresponding to a 1dB loss associated with the MMI device. All MMI devices that were fabricated measured an even split between the output waveguides.

The 300μm and 650μm-long curves exhibited losses of 1dB and 2.3dB, respectively, indicating that the majority of the losses associated with the Y-splitters were the result of difficulties in defining the 200nm-wide tip. The optical losses of the curves are likely lower yet, as there were instances of damaged facets along the sample and as the losses from the longer curve are expected to be lower than the optical losses of the tighter bends.

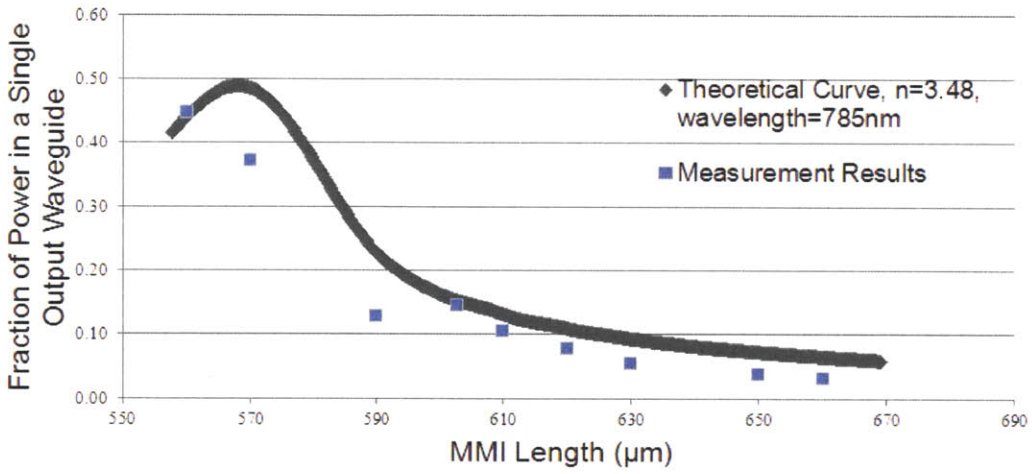

Figure 4-27: Comparison between the expected theoretical curve (calculated at an operational wavelength of λ=0.785μm and for an index of refraction of $n = 3.48$) for a 16μm-wide MMI of the fraction of power in a single output waveguide as a function of MMI length (grey curve). The characterization results of fabricated MMI structures (blue data points) are overlaid on top of the theoretical curve. Despite two outlying points that are the result of non-ideal coupling or damaged facets, measurements adhere to the theoretical curve and indeed expect that the 3dB power split occurs at the theoretical value of a 567μm-long MMI. An even power split was obtained at a length of 560μm, with MMI-associated losses of 11%, or 1dB per MMI device.

While the 12μm-wide MMIs did split the input power evenly between the output waveguides, the MMIs were more difficult to define accurately by photolithography as they were poorly defined on the mask and the 4μm gap between the output waveguides was difficult to resolve, leading to rounded edges instead of corners of the waveguides. The wider, 6μm separation of the output waveguides in the 16μm-wide improved the pattern transfer

from the mask to the photoresist, and displayed enhanced transmitted power at the output relative to the output of the 12μm-wide MMI.

4.5 Summary

In this chapter, a self-aligned mask set and extensive development of fabrication technologies have been offered and optimized, and were verified by the processing of modulator components. The waveguiding capability of the n-i-n heterostructure has been demonstrated, culminating with 1.45cm-long, 2μm-wide ridge waveguides that exhibit optical losses of 0.93dB/mm. Waveguide modulator multimode interferometer and Y-splitter power splitting components have been designed, simulated, and fabricated, and have achieved even power splitting between output waveguides. While the Y-splitters exhibited 10dB of loss per device, the 560μm-long, 16μm-wide MMIs have been shown to operate as theoretically expected, and have shown a -3.5dB power transmission at each output waveguide. Overall, the 560μm-long MMIs exhibit optical losses of 1dB per device. With the performance of the modulator components qualified, fabrication processes optimized, and the creation of a mask set ensuring successful power transmission between optical components, a final fabrication flow and mask set can be designed, integrating all developed processes and techniques to lead to a completed optical modulator.

Chapter 5

Final Remarks and Future Research Recommendations

The work that was presented in this thesis consists of the design, simulation, and growth of novel heterostructures as the foundation of broadband modulators that are based on the electrooptic effect. The electrical behavior of the n-i-n MOS ridge structure was simulated and studied through capacitance-voltage profiling, assessing the performance of the epitaxial structure as a modulator. The design of the modulator Mach-Zehnder Interferometer devices and power splitting components was detailed, and a self-aligned mask set which optimizes power coupling between the different segments of the modulator was developed and fabricated. Fabrication methods and techniques were investigated and verified through the processing and testing of waveguides, Y-junctions, and multimode interferometers, demonstrating the optical capabilities of the n-i-n metal-oxide-semiconductor heterostructure, and qualifying the fabrication methods and device designs.

With the separate components of the modulator characterized, effort can now turn to the integration of individual components and to improvements in the heterostructure and in the fabrication processes that can augment the performance of the modulator.

5.1 Next Generation Mask Set

Figure 5-1 shows the next generation self-aligned, five-layer mask set. The rectangular patterns on the first mask, which mark the areas of the MZI arms, have been moved further away (by 14μm) from each other so that the MZI arms are separated by 28μm center to

center. The larger separation will aid in achieving uniform planarization over the MZI arms and in the lift-off process of the topside contact metalization. In the second mask layer, multimode interferometers 16μm-wide and 565μm-long have been adopted as the power splitter components. As the output waveguides of the MMIs are separated by 6μm, 300μm-long curves extend from the MMI output waveguides to the MZI, and propagate the optical mode from the MZI arms back to a 2x1 MMI.

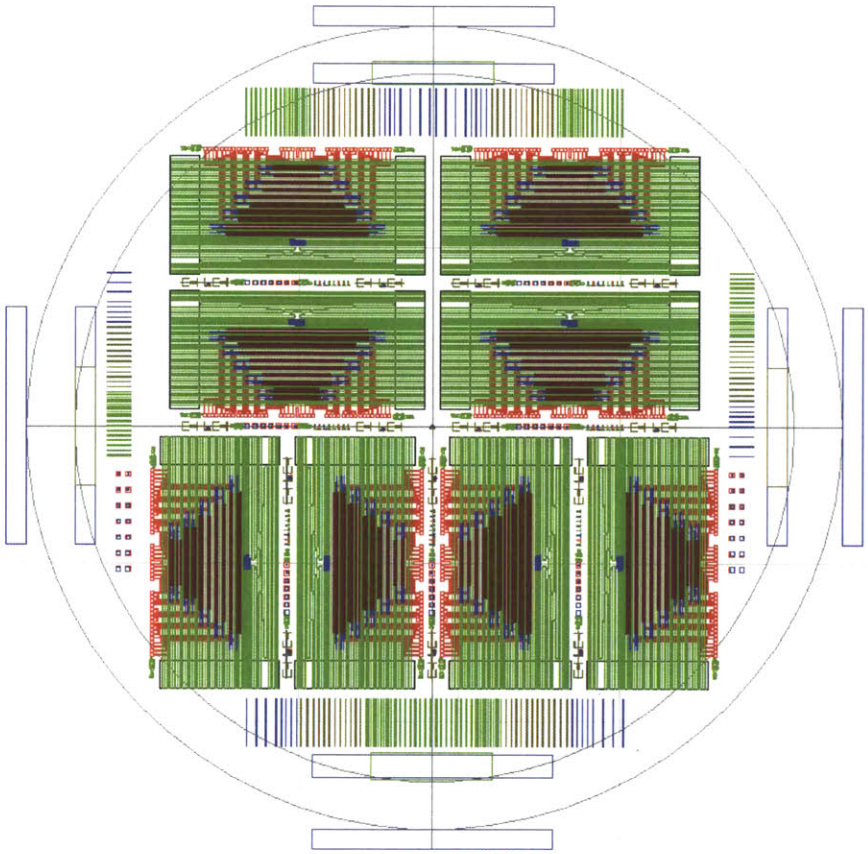

Figure 5-1: The next generation five-layer mask set. The MZI arms have been moved away from each other to a distance of 26μm to ease planarization and metalization. On the fourth mask, 200μm-wide square probe pads extend beyond the areas of the modulator devices, reducing concerns of damage to the device during characterization. A fifth BCB facet etch mask has also been added to the set to facilitate cleaving of the facets.

The third mask layer, employed in the BCB etch back process to expose the top of the ridge waveguides prior to metalization, has been changed to reflect the adjusted distances

between the MZI arms. The fourth lithography mask defines the probe pads which extend beyond the areas of the modulator devices, easing electrical probing and reducing concerns of damage to the device during characterization. Finally, the BCB facet etch mask has been integrated into the mask set, facilitating cleaving of the facets and improving fiber-to-facet coupling.

5.2 Push-Pull Operation

The oxidized AlAs layers in the n-i-n MOS heterostructure enable the modulator to withstand higher operating voltages both in reverse and forward bias without concern of breakdown or carrier loss. Consequently, the device is essentially unipolar and can be powered in a push-pull manner that reduces the required Mach Zehnder arm length. A Mach Zehnder-based modulator with two interferometer arms (1 and 2) requires that

$$(\beta_1 - \beta_2)L = \pi \tag{5.1}$$

The phase difference is achieved by:

- Applying voltage across arm 1, and varying β_1 relative to β_2
- Applying voltage across arm 2, and varying β_2 relative to β_1
- Or by applying a voltage across both interferometer arms, and increasing β_1 and decreasing β_2 (or vice versa)

The latter option is the push-pull operation, which provides chirp-free modulator performance with a transfer function of

$$\frac{|A_o|^2}{|A_i|^2} = cos^2\left(\frac{\pi}{2}\frac{V(t)}{V_\pi}\right) \tag{5.2}$$

Modulators that were investigated by Sakamoto et al ([58]) and Shin et al ([59]) achieved push-pull operation in which the substrate was removed. To fabricate substrate-removed modulators, the modulator device is placed on top of a transfer GaAs wafer and glued using a BCB polymer. The heterostructure is grown by MBE on a growth wafer with an etch stop layer on top that is used to remove the growth wafer. The modulator devices are processed as normal through the evaporation and lift-off of topside contacts (which ultimately become

the backside contacts). The sample is then turned over and placed on a GaAs transfer wafer with a layer of BCB. The BCB is annealed to harden the film and secure the samples to the transfer wafer. A wet etch removes the growth substrate, and deposition of topside contacts completes the fabrication prior to wafer lapping and cleaving.

Construction of a push-pull modulator with the substrate-removal method is a difficult endeavor for several reasons. First of all, the accurate alignment between the original sample and the transfer wafer is very difficult to achieve, and if not executed correctly, is problematic during the cleaving of the samples. Secondly, the removal of the growth substrate is a crude process, and wet etchant could easily damage the devices on the sample that are improperly protected. Finally, the top doped layers must be exposed to some method of etching during the removal of the etch stop layer by either wet or dry etching. Both etching processes can cause surface damage to the top semiconductor and degrade the quality of the top-side contacts.

Instead, variations on the n-i-n MOS heterostructure, the fabrication process, and the mask layout are proposed to allow for the placement of the backside contacts on the front side of the growth wafer. Figure 5-2(a) shows the topside schematic of the proposed device. The input and output waveguides, MMIs, and bottom contacts are covered by BCB with the exception of the input and output facets and the probing pads of the bottom contacts, all of which are made accessible for characterization. Both MZI arms have top and bottom contact to allow each arm to be independently powered. In this configuration, the electrodes over each of the MZI arms can be biased independently, doubling the device efficiency and reducing the required active arm length by two [106].

The black dashed line in Figure 5-2(a) points to a cross-sectional image of the n-i-n MOS modulator device provided in Figure 5-2(b). Several modifications have been made to the heterostructure to allow for the definition of front-side bottom contacts and to improve device operation. The undoped $Al_{0.27}Ga_{0.73}As$ cladding layers have been removed from the structure due to their behavior as capacitors under an applied voltage. The purpose of the cladding layers was to distance the optical mode from the charge carriers that are located in the doped semiconductor layers surrounding the dilute core, a function that can also be fulfilled by thicker Al_xO_y layers.

To form the bottom contacts, the lower $10^{18}cm^{-3}$, Si-doped semiconductor layers have been changed to a stack of Si-doped $Al_{0.27}Ga_{0.73}As/In_xGa_{1-x}As/Al_{0.27}Ga_{0.73}As$. The $In_xGa_{1-x}As$

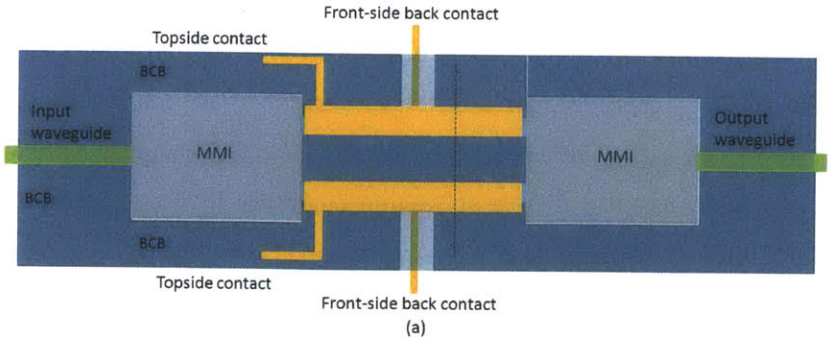

(a)

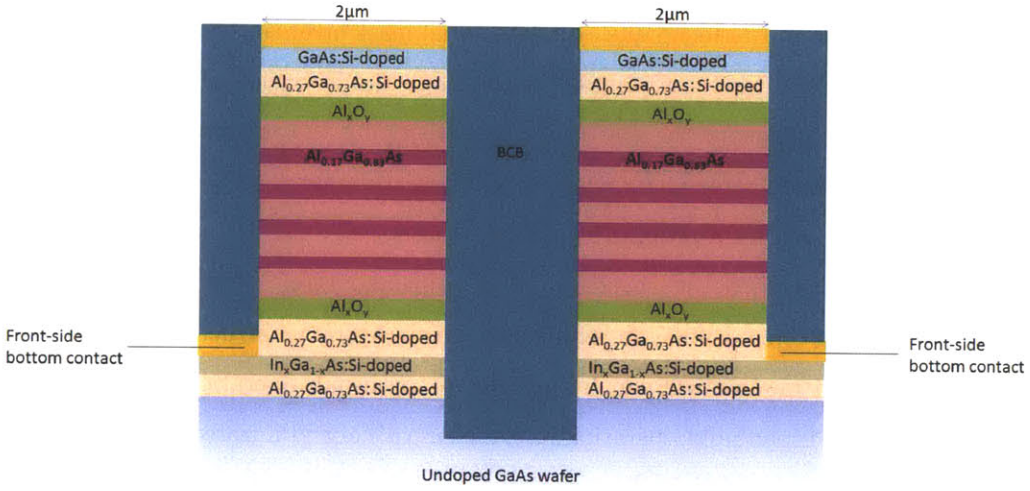

(b)

Figure 5-2: Topside (a) and cross-sectional (b) schematics of a push-pull modulator. The black dashed line identifies the location of the cross-sectional cut highlighting the schematic of the heterostructure in (b). The front-side bottom and top electrodes around each of the MZI arms can be independently biased, which allows for push-pull operation of the modulator and reduces the required active MZI arm length by two. A Si-doped $In_xGa_{1-x}As$ etch stop layer has been added to the bottom doped semiconductor stack to facilitate the placement of the bottom electrodes. In the absence of undoped $Al_{0.27}Ga_{0.73}As$ cladding layers, the thickness of the Al_xO_y layers has been increased to distance the optical mode from carriers in the doped semiconductor layers surrounding the core. Thick doped $Al_{0.27}Ga_{0.73}As$ layers were placed at the bottom of the heterostructure to enable coupling into the waveguide core, by distancing the dilute core from the absorbing substrate and $In_xGa_{1-x}As$ material.

serves as an etch stop layer during the ridge-defining ICP-RIE of the III-V semiconductor films. The etch exposes the $In_xGa_{1-x}As$ material so that bottom contacts can be defined. $In_xGa_{1-x}As$ is a good candidate for a contact layer due to the narrow bandgap relative to GaAs, but also has a higher index of refraction than $Al_{0.27}Ga_{0.73}As$ at λ=0.8μm. Si-doped $Al_{0.27}Ga_{0.73}As$ layers are grown both above and below the $In_xGa_{1-x}As$ material to further distance the dilute core from the higher refractive index of the $In_xGa_{1-x}As$ and the doped GaAs substrate. To isolate the bottom contact, the III-V areas beyond the contact are etched into the undoped GaAs wafer on which the structure is grown.

The method of constructing a push-pull modulator detailed here does not require sensitive and difficult alignments or long wet etches that can jeopardize devices as is proposed by the substrate-removal technique. An additional mask layer is necessary for the definition of bottom contacts after the formation of the ridge and oxidation of the AlAs layers. Due to the large dimensions of the electrodes and with only the requirement of placing them on top of the doped $In_xGa_{1-x}As$, the added fabrication steps are not expected to further complicate the fabrication process.

This thesis discussed the development of p-i-n and n-i-n MOS modulators operating at λ=0.8μm, and offered possible refinements to the epitaxial structure of the broadband, n-i-n MOS-based modulators which can lead to push-pull operation. The realization of modulators with broadband operation in the near-visible and infrared spectrum will enable the development of an optical arbitrary waveform generation system, which will in turn lead to new and unimagined applications of ultra-short pulses generated by a Ti:Sapphire laser.

Appendix A

Processing Technologies

This appendix provides an overview of the processing technologies relevant to the work in this thesis. The following sections shed light on the considerations, requirements, advantages, and disadvantages of several fabrication methods that were used or considered in the processing of the modulator components.

A.1 Molecular Beam Epitaxy

There are three ways of depositing epitaxial thin films: Molecular Beam Epitaxy (MBE), Liquid Phase Epitaxy (LPE), and Metal Organic Chemical Vapor Deposition (MOCVD). All methods are used to grow compound semiconductors, but MBE and MOCVD typically deposits crystals for laser and electronic applications. This section explains the operation of the Veeco Gen200 solid source MBE system that was used in the growth of the modulator heterostructures. For more information on growth by MBE, consult the work of Chang [107].

The deposition chamber of the molecular beam epitaxy tool is under an Ultra-High-Vacuum (UHV), at pressures on the order of 10^{-10} Torr. The chamber is thoroughly cleaned and pumped to avoid contamination and the introduction of impurities into the system under atmospheric conditions. The low pressures during the deposition process ensure a long mean-free path, λ, defined by

$$\Lambda = \frac{kT}{\pi D_{atom}^2 P\sqrt{2}} \tag{A.1}$$

and is dependent upon temperature, T, atom diameter, D, and pressure, P. A long mean free path reduces interaction between the deposited molecules on their way to the substrate from the source. The low pressure environment also minimizes contaminants or products in the chamber, ensuring the high purity of the deposited layer.

Substrates are introduced into the chamber via a load lock chamber which is pumped down to 10^{-2} Torr. After switching to a cryo pump, the load lock chamber is pumped down to approximately 10^{-8} Torr, at which point the substrate can be transferred to a UHV transfer chamber where the substrate is heated to remove moisture prior to growth. In the deposition chamber, the wafer is heated to aid in the desorption of the substrate's native oxide. Simultaneously, effusion cells containing groups III and V elements, as well as dopants of groups II and IV elements, are heated individually to temperatures between 300°C and 1200°C (depending on the vapor pressure of each element) to evaporate the elements. The evaporated elements form beams which diverge within the deposition chamber, with a flux set by the effusion cell temperature. The cells are placed in a calculated configuration which directs the diverging beam onto the substrate. Computer-operated shutters that are placed above the effusion cells control the growth thickness, and enable transitions between materials during growth. During film growth, the substrate is heated to temperatures that allow the adsorbed atoms, known as adatoms, to migrate and find an energetically favorable site where they may be incorporated into the lattice.

Samples can be monitored by reflection high-energy electron diffraction, or RHEED, or by measuring sample transparency. Following the deposition, photoluminescence and x-ray measurements of the layers are taken to verify the accuracy of the growth.

A.2 Photolithography

Photolithography is a process that uses light and heat to produce chemical reactions resulting in patterns in light-sensitive organic material (photoresist). There are two varieties of lithography processes - positive and negative. Positive photolithography employs a positive resist which is baked and exposed to ultraviolet light through a quartz mask with chrome-coated patterns. The exposed areas of the photoresist develop away in specially formulated developer chemistries, while unexposed areas identical to the chrome pattern remain. In negative photolithography and image reversal, the pattern transferred is the negative of the

mask image. The mask pattern determines which type of lithography, positive or negative, is used; however, as the mask is most often designed to simplify alignments or enhance pattern transfer resolution, the choice of lithography process is typically an afterthought and not a design consideration.

A.2.1 Positive Photolithography

An illustration of the positive photolithography process is provided in Figure A-1. Photoresist is spun for a time period and at a speed that are related to the final film thickness and submitted to a pre-exposure bake. The objective of the pre-bake is to sufficiently drive out the solvents in the resist as well as prevent adhesion to the mask during exposure, which could result in unbalanced contact with the mask and the possible breaking of the wafer upon contact. As a result, the baking temperature, time and uniformity are not critical and a convection oven may be used. However, if the baking temperature is too low, adhesion at the oxide/semiconductor-photoresist interface may be compromised. If an oxide is present on the wafer surface, hexamethyldisilazane (HMDS) is applied prior to resist application. The HMDS reacts with the oxide, forming a hydrophobic layer that promotes adhesion at the oxide-photoresist interface by repelling developer molecules that could otherwise seep into the interface and remove the desired photoresist features.

Once the resist is pre-baked, the wafer and mask are brought into contact by an aligner, and a shutter opens to expose the resist to ultraviolet light. Photoresist areas under chrome-coated patterns of the mask are shielded and receive no light, while regions of resist beneath the transparent quartz material are exposed to a light dosage set by

$$Dosage = I \cdot t \tag{A.2}$$

where I is the exposure intensity in units of $\mathrm{mW/cm^2}$ and t is the exposure time. The dosage is a constant for the photoresist material and pre-bake time and temperature. As the bulb intensity may drift over time, the exposure time can be adjusted to account for the decrease in intensity. The exposure sets the resist profile and dimensions; therefore, determining and maintaining accurate dosage with good uniformity across the wafer is very important. Good contact between the mask and wafer is also imperative, as gaps significantly alter the defined features and make the lithography process unpredictable. The exposure to

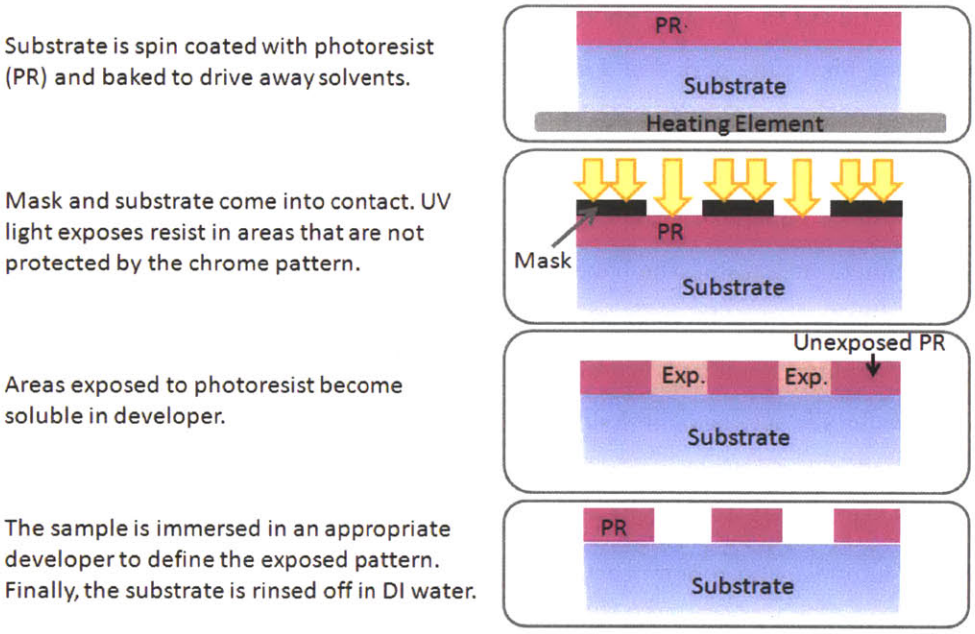

Figure A-1: Illustration of the positive photolithography process. The procedure results in the transfer of the mask image pattern to a photoresist layer. A substrate is coated with photoresist, which is baked to dispel solvents. After exposure to ultraviolet light, regions that were exposed dissolve in developer, while unexposed areas remain.

UV light modifies the resist chemistry so that the resist becomes insoluble in an aqueous solution called a "developer". Hence, unexposed areas set by the mask pattern remain after development. A rinse in deionized water terminates the development process, and the wafer is dried with a nitrogen gun in preparation for the next step.

A.2.2 Negative/Image Reversal Photolithography

The negative and image reversal processes (shown in Figure A-2) differ in a few ways from each other and from the previously described positive photolithography method. Negative photolithography is typically used as a protective mask during wet or plasma etches, and is therefore characterized by a near-vertical sidewall profile. Image reversal, on the other hand, is primarily used as part of a "lift off" technique, in which metal is evaporated over a photoresist pattern that is subsequently dissolved in acetone, causing any metal over the resist to be "lifted off". The sidewall profile of image reversal resists tends to be outwardly slanted, so that metal evaporation cannot coat the sidewall of the resist structure, and hence the acetone can easily penetrate to dissolve the photoresist.

Like positive lithography, the exposure step of the negative and image reversal processes chemically activates photoactive compounds (PAC) in the exposed portions of the resist. However, in the negative and image reversal processes, a post-exposure bake is added to thermally cross-link the active PAC and render exposed areas insoluble in developer. Image reversal requires one additional long UV light exposure prior to development which activates PAC much like the positive process, turning single-exposure sections of the photoresist soluble to the developer solution.

Much has been written of the sensitivity of the post-exposure bake step. Setting the bake time constant and running trials involving coated, pre-baked and exposed wafers can narrow down the range of suitable post-baking temperatures. If the post-bake temperature is too high, the resist layer will be thermally cross-linked and will remain in its entirety after development. If the temperature is too low, the resist will be completely removed during emersion in developer.

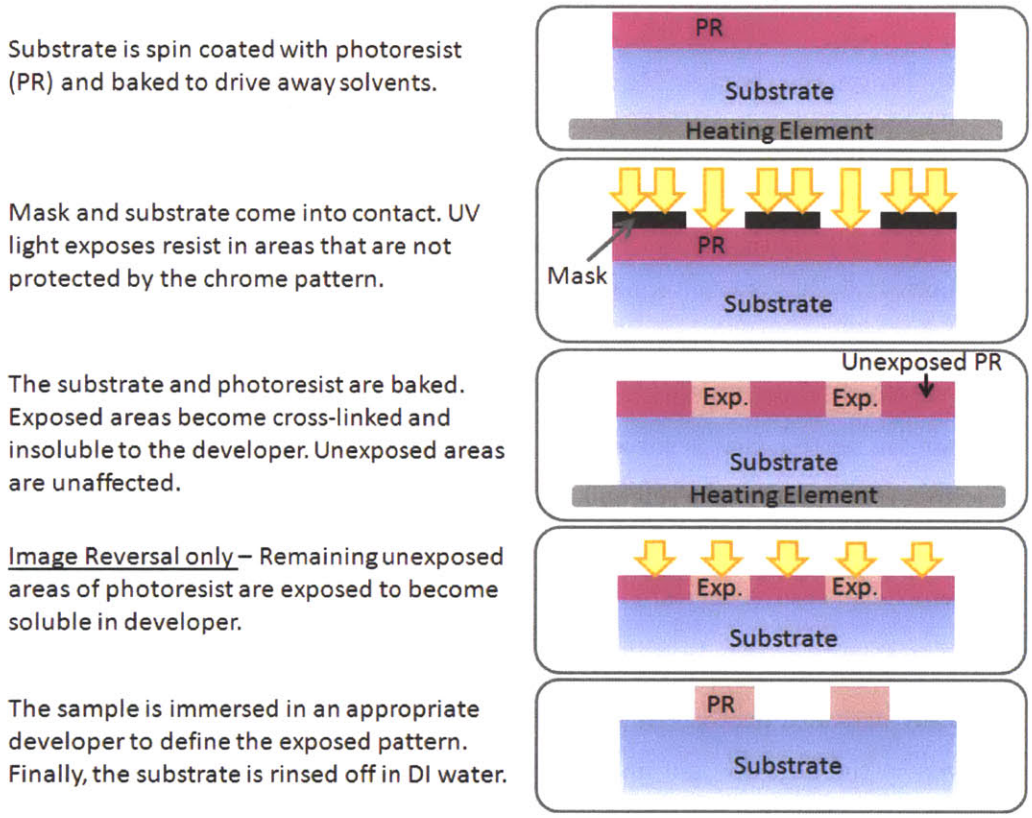

Figure A-2: Negative and image reversal photolithography processes.

A.3 Dielectric Deposition

Chemical vapor deposition (CVD) is a versatile method of depositing high-quality thin films. Within a low-pressure chamber, carrier gases transport precursor gases to the wafer surface, where they react or decompose to form a deposited layer. Any by-products of the reaction are thereafter pumped out of the system along with the carrier gases.

Any number of reactant gases or reactions can be chosen to produce the final reaction product, making the deposition process quite flexible. A silicon dioxide, SiO_2, film commonly uses oxygen (O_2) and silane (SiH_4) gases in the reaction:

$$SiH_4 + O_2 \rightarrow SiO_2 + 2H_2 \tag{A.3}$$

Oxide can also be deposited with a nitrous oxide (N_2O) :

$$SiH_4 + 2N_2O \rightarrow SiO_2 + 2N_2 + 2H_2 \tag{A.4}$$

Stoichiometric silicon nitride, or Si_3N_4, can be produced by combining silane with either nitrogen gas (N_2) or ammonia (NH_3) in the following manners:

$$3SiH_4 + 2N_2 \rightarrow Si_3N_4 + 6H_2 \tag{A.5}$$

$$3SiH_4 + 4NH_3 \rightarrow Si_3N_4 + 12H_2 \tag{A.6}$$

The refractive index of nitride is highly dependent on the concentration of silane in the product. Maintaining a low refractive index (<2) is difficult, but can be achieved by adding a high percentage of nitrogen gas while flowing a sufficient amount of silane necessary for the deposition to take place [108, 109].

Plasma-enhanced CVD (PECVD) uses discharge from an RF source-generated plasma to promote the chemical reaction between the substrate surface and gas reactants, and produces films with varying density depending on the temperature of the deposition. A high-density plasma can also lead to sputtering of the grown film due to a high density of ions. In turn, this effect allows uneven surfaces such as vias and trenches to be conformally coated. Variables that are considered in the deposition process include the substrate temperature and the frequency of deposition. Higher temperatures and a high deposition frequency

typically result in dense films and consequently, have higher indices of refraction and low chemical etch rates [108, 110, 111].

A.4 Reactive Ion Etching

Lithography-set patterns in photoresist are transferred into dielectric material or semiconductor structure by a process of reactive ion etching (RIE). Etchers employ both physical ion bombardment and exposure to etching chemistries as a means of removing material anisotropically. Selectivity between the etched material and the masking material is possible with appropriate choices of etch gases, but the physical aspect of the etch (sputtering) typically makes RIE a less selective process than wet etching.

Reactive ion etchers consist of a chamber with gas inlets, an electrically powered stage on which the substrate is placed, and a grounded electrode. Once the chamber is pumped down to pressures around 10^{-5}Torr, gases flow into the chamber and are constantly pumped out by a vacuum pump. To begin etching, a radio frequency (RF) field is applied through the powered electrode, ionizing the molecules within the chamber and igniting a plasma. As atoms on the substrate surface react with species from the plasma, they form by-products which are removed by ion bombardment resulting from a DC voltage that is produced between a sample and the plasma.

There are several types of RIE systems, including an inductively-coupled plasma reactive ion etcher (ICP-RIE). An RF-powered magnetic field generates a high-density plasma of reactive gas atoms while another RF source is applied to an electrode beneath the sample holder, accelerating ions from the plasma to the substrate. The exceptional plasma density also accounts for increased etch rates and selectivities, such as a 200:1 GaAs to $Al_{0.2}Ga_{0.8}As$ selectivity as reported by Lee et al [112].

Several parameters can be adjusted in developing a reactive ion etch - chamber pressure, DC voltage, RF power, gas flow, material selectivity and etch length. As in the MBE, a longer mean free path in the RIE chamber translates into fewer inter-ion collisions which result in increased ion energy. Pressure plays a major role in the directionality of the ions; increasing the chamber pressure reduces ion energy due to collisions, and increases etch rate as there are more etchants in the chamber. High pressure etches tend to be less directional, even resulting in undercutting of the pattern. Decreasing the chamber pressure increases

ion energy, and enhances directionality and anisotropy, but reduces the etch rate as atom concentration drops. RF power also regulates the etch rate, with high RF power producing faster etching. High DC bias is associated with more anisotropy, but also leads to sputtering which reduces the selectivity between the etch mask and etched material [113]. Gas flow rates, flow chemistries and ratios thereof modify etch rates and can positively or adversely affect etch profiles, i.e. some chemistries passivate during RIE (as in the Bosch Process [114]) or are used primarily for ion bombardment.

A.4.1 Chamber Cross-contamination

Reactive ion etch chambers have a tendency to retain the effects of previous processing steps [113]. Etched materials, gases, byproducts and hard mask films that are sputtered during the RIE remain in the chamber and interfere with subsequent etches. The unwanted remnants can influence etch rates and structure profiles, many times producing a "grassy" surface and reducing the consistency in yield and RIE results from etch to etch.

A chamber cleaning procedure aid in removing debris of formerly etched materials and in pumping out gaseous residue and byproducts. Diagnosing the cleanliness of the chamber is easily done by tracking the power or voltage (whichever parameter is not set by the user) over time. If the level increases over time, the change is likely due to the state of the chamber. Additionally, running a conditioning etch prior to the primary sample etch is advised, as the run prepares the chamber environment for the subsequent etch, introducing only the desired gas species. The conditioning etch is identical to the real RIE process, but is typically considerably longer. Depending on the material that is to be etched, the conditioning run can help eliminate grass and increase the consistency of etch rates from etch run to run.

A.5 Planarization

Deep trenches, vias, and varying topography across a sample are difficult to metalize by directional and anisotropic methods of deposition such as evaporation, which works best on uniform planes. Uneven surfaces are similarly problematic in photolithography, where good contact between sample and mask determine the quality and resolution of patterns. Therefore, prior to metalization or photolithography, customarily the sample surface is

leveled with a technique known as planarization. One such approach applies a spin-on polymer that also passivates and solidifies upon curing to form an electrically insulating, heat dissipating dielectric.

The benzocylobutene (BCB, C_8H_8) molecule is composed of a benzene and cyclobutane rings and is a popular choice of planarizing polymer. Dow Chemical produces a line of B-stage BCB products (Cyclotene 3022 Series) which support an initial curing, or soft cure, of the BCB that can be prematurely arrested before all monomer molecules are fully cross-linked. This allows the full, or hard cure, of the film to be completed at a later time. Mechanical, electrical and thermal properties of the Cyclotene 3022 series are provided by Dow Chemical and shown in Table A.1. A chart of the BCB process flow is provided in Figure A-3.

Table A.1: Mechanical, electrical, and thermal properties of the Cylotene 3022 series.

Property	Value
Breakdown Voltage	5.3x10^6 V/cm
Volume Resistivity	1x$10^1$9 Ω-cm
Thermal Conductivity	0.29W/m^{o}K at 24^{o}C
Residual Stress	28+/-2MPa at room temperature

BCB can have poor adhesion to III-V semiconductor materials. A formulated adhesion promoter, AP3000, containing an organic silane group is applied prior to the application of BCB to further encourage adhesion at the dielectric surface by providing a compatible organic surface for the BCB polymer to bond with. Another approach to circumvent the issue of adhesion is to introduce an intermediate layer between the semiconductor-BCB interface. PECVD-deposited nitride or silicon dioxide are appropriate choices, but the stress in nitride films in conjunction with thick layers of BCB polymer can lead to peeling of both films after the BCB cure. If nitride is used, then adhesion at the nitride-BCB interface is improved with the use of a N_2 source rather than a NH_3 nitrogen source during film deposition.

The BCB is applied by spin coating at a speed that is related to a final coating thickness. The film is baked briefly to evaporate solvents and to sufficiently solidify the film for further handling. A hard cure in N_2 ambient achieves 95-100% polymerization of the BCB at temperatures that are higher than 250^{o}C and for lengths greater than 60min. As the

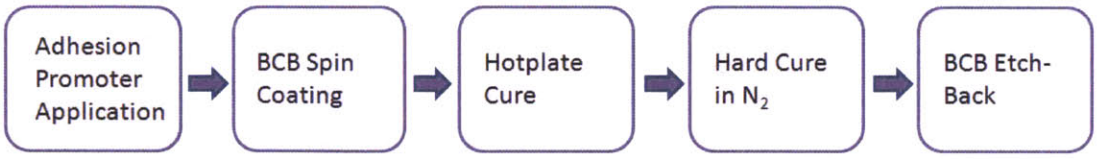

Figure A-3: Flow chart of the BCB application, cure, and removal steps.

thickness of the BCB film increases, longer cures in nitrogen may be required. Between 400°C and 475°C, the BCB undergoes molecular changes and begins to contract [115]. Though annealing of metals to reduce contact resistant takes place at such temperature ranges to reduce contact resistance, the advantage may be outweighed by the deterioration of the BCB.

A.5.1 BCB Etch-Back

As BCB is primarily organic with some Si presence, plasma etching by RIE demands both fluorine and oxygen components. Without fluorine species, an oxygen-based RIE self-passivates by forming amorphous silicon on the BCB surface that cannot be removed. According to Dow Chemical, the amorphous film is fragile and may also propagate cracking of the BCB layer, and therefore a fluorine component should always be included. The etch rate of BCB reaches a maximum at O_2:CF_4 ratio of 2:3 and decreases significantly away from this point [116]. The benefit of decreasing the fluorine to oxygen ratio is the increased selectivity between chemical vapor-deposited dielectrics and the BCB polymer. The etch rate is also increased by etching at higher powers or pressures.

A.6 Metalization

Metalization is a basic process of semiconductor fabrication and a fundamental part of integrated circuits. Proper choices of 1) semiconductor material (including doping levels and type) , 2) contact type, and 3) processing methods are integral to the successful design of metal contacts and optimization of semiconductor device operation. This section will provide insight to these factors and to the metal-GaAs system specifically.

A.6.1 Metal-Semiconductor Contacts

There are two types of metal contacts - Ohmic and Schottky. Ohmic contacts are characterized by low series resistance at the metal-semiconductor interface (with a linear I-V curve), while Schottky contacts display rectifying behavior much like a diode due to a high-resistance depletion region. This region, otherwise known as a Schottky barrier, is formed when the semiconductor and metal are brought into contact and the system is at thermal equilibrium. If the semiconductor is n-type, the higher energy electrons of the semiconductor will move into the metal until the Fermi levels of the two materials are equal. As positive ions accumulate in the electron-depleted boundary region, an electric field emerges that causes the semiconductor valence and conduction band edges to bend upward. At the metal-semiconductor boundary, the barrier height, ϕ_B, is described as the potential difference between the band edge of the semiconductor (χ_s, signifying electron affinity) and the metal Fermi level (ϕ_m):

$$\phi_B = (\phi_m - \chi_s) \tag{A.7}$$

Similarly, for a p-type semiconductor, the barrier height is defined as the difference between the valence band edge and the metal Fermi level.

Current transport in Schottky contacts is set primarily by diffusion of majority carriers in the metal-semiconductor junction and by thermionic emissions (carrier flow induced by heat) over the Schottky barrier [109]. In highly doped semiconductors (over 10^{17} cm^{-3}), current density is strongly dependent on impurity concentration [117]. The high doping level narrows the Schottky barrier significantly, allowing majority carriers to tunnel by a process known as thermionic-field emission directly from the semiconductor to the metal through the barrier. In the thermionic-field emission regime, the Schottky contact resistance is low, and the current-voltage behavior is that of an ohmic contact. Therefore, ohmic contacts can be achieved with a sufficiently highly-doped semiconductor-metal interface.

Contact metals have been categorized by Sinha and Poate into three groups [118]:

1) Noble metals with large electronegativities (i.e. Cu, Ag, Au) that drive the separation of the group III and V materials, causing group III elements to diffuse into the metal (in the Au/GaAs interface, Ga diffuses into the Au layer at low annealing temperatures 250^oC).

2) Near-transition metals and near-noble, with large electronegativities (i.e. Ni, Pd, Pt). These metals form reliable and stable compounds with group III and V elements that

migrate into the layer at annealing temperatures 350^oC.

3) Early transition metals with small electronegativity (i.e. Ti, W, Cr). The metal-semiconductor interface react only at temperatures $>500^oC$.

Alloyed thin films based on Au are often employed in the pursuit of low resistance ohmic contacts to III-V materials. The stacks typically include Ge for an n-doped interface or Zn for a p-doped interface. The Au-Ge/Ni metal system provides low resistance contacts with n-type semiconductors. The contact resistance, r_c of Au-Ge/Ni alloyed to GaAs is determined by

$$r_c = (1.8 \cdot 10^{12})/n \tag{A.8}$$

where n is defined as the majority carrier concentration, typically 10^{15} - 10^{19} cm^{-3} [109, 119]. For 10^{18}-doped n-type $Al_{0.4}Ga_{0.6}As$, the Au-Ge/Ni contacts have a minimal resistance of r_c=$2 \cdot 10^{-4}$ Ω-cm^2.

At 400^oC and theoretically above 360^oC, Ge (as part of a Au-Ge alloyed contact on n-type GaAs) diffuses through and dopes the GaAs [120], producing an n+ doped layer and resulting in linear I-V behavior of an ohmic contact [121]. In order for the doped layer to successfully form, the Au-Ge must sufficiently melt into, or wet, the semiconductor surface; this mechanism is significantly improved with the addition of Ni. Au, a non-reactive metal with high conductivity and low resistance, is added on top of the ohmic contact stack to aid with probing and for plating and wire-bonding.

A popular choice of contact alloyed to p-type GaAs and III-V materials is Ti/Pt. Annealing is performed between 350^oC (below this point no reactions occur between the compounds) and 500^oC (above this point, the formation of TiAs hampers the alloying of the Ga and Pt, damaging contact quality) [109].

A.6.2 Methods of Metalization

Ideally, ohmic contact should be high quality, thermally stable, and exhibit low stress and resistance. Along with the semiconductor doping levels and alloyed metal stack, the deposition process itself plays a large role in the success or failure of contact fabrication. For instance, metalization by sputtering and ion bombardment affords full coverage of metal over the semiconductor surface but can also inflict considerable damage.

Metal sheet resistance also presents a problem. Assume a metal contact layer of thick-

ness, t, has been deposited over the area of a semiconductor ridge (Figure A-4) of width, W, and length, L, and a voltage is applied to the device by probing the metal at a random point along the sheet. If the sheet resistance of the metal is low, the voltage along the metal

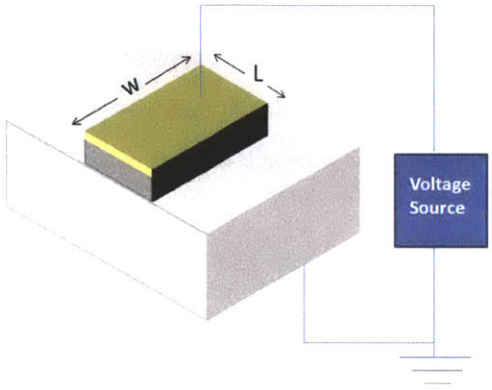

Figure A-4: Depiction of voltage applied to a metal sheet of thickness, t, deposited over a ridge of width, W, and length, L.

contact layer will be fairly uniform and the effect on the semiconductor device is expected to be fairly uniform throughout. However, if the sheet resistance is high, the voltage will differ significantly along the length of the sheet, hampering device operation. The relationship between sheet resistance, R, and the contact layer geometry is given by

$$R = \rho \frac{L}{Wt} \tag{A.9}$$

Reduction of the sheet resistance can be more easily achieved by increasing the metal thickness, t, rather than by adjusting the device dimensions that are often set by a variety of factors. Thicker contact metals also ease device probing during the measurement process, as crude metal probes can puncture through thin layers of metal and damage the semiconductor surface.

Three methods of metal deposition have been identified for the purposes of this work. The first, electron beam physical vapor deposition or e-beam, is primarily used for the thin-film deposition of ohmic and Schottky contact structures. The later two processes, electroplating and electroless plating, offer two techniques of thicker Au metal deposition. An overview of the operation, advantages, and disadvantages of the three approaches is provided in the following sections.

Electron Beam Physical Vapor Deposition

Evaporation of metal contacts by electron beam physical vapor remains a popular method of deposition. The system chamber holds crucibles filled with ingots of material to-be deposited, an electron beam guns and a substrate holder. The gun generates an electron beam that is focused onto the solid material ingot. Upon contact with the crucible surface, a majority of the beam energy is converted to thermal energy, melting the ingot first to a liquid (with the exception of materials that sublimate), and then to a vapor that leaves the crucible. Collisions between gas atoms in the chamber are minimized by pumping the chamber down to pressures as low as 10^{-6}-10^{-7} Torr in order to achieve long mean free paths. The atoms solidify on the sample and chamber walls to produce a coating that is primarily non-conformal. This directionality is preferable for evaporation processes that will be used in conjunction with the lift-off technique.

The thickness of deposited metal in the lift-off process is limited mainly by photolithography. The definition of contacts by e-beam evaporation typically involves an image reversal or negative photolithography step (see section A.2.2). Once a photoresist pattern is set such that areas to be metalized are exposed while areas that should not see metal are protected by photoresist, metal is deposited by evaporation over the entire sample. Subsequently,

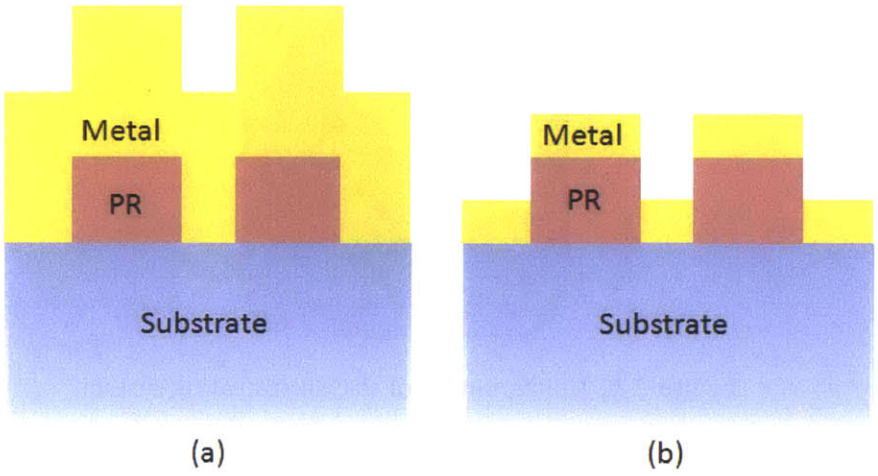

Figure A-5: Process of metal contact definition by metal evaporation and lift-off. If the thickness of deposited metal exceeds that of the photoresist pattern (a), acetone is not able to infiltrate and dissolve the photoresist; as a result, metal in undesired areas remains. However, if metal thickness is less than half of the photoresist thickness (b), the photoresist is successfully dissolved and the overlaying metal is removed.

the sample is immersed in acetone, dissolving the photoresist and removing the overlaying metal. If the metal thickness is greater than the thickness of the photoresist, as in Figure A-5(a), acetone will not reach the photoresist and the superimposed metal will not be removed. Ideally, photoresist thickness should be 2-3x that of the deposited metal (see Figure A-5(b)), exposing the organic material to acetone and lifting off any metal coating.

In this work, negative photoresists NR7-1500PY and NR9-1000PY of thicknesses 1500nm and 1000nm respectively were employed. These resists limit the metal deposition thicknesses to thicknesses of 500-750nm for consistent, successful liftoff of metals, but require only one photolithography step and no wet etches.

Electroplating

There are four components to the electroplating process setup, shown in Figure A-6: a power supply, anode, cathode, and an electrolyte-filled bath. Once power is applied, electrons from the metal, or anode, flow toward the power supply, leaving positive cations behind that dissolve into the immersing electrolyte bath. Due to the potential difference between

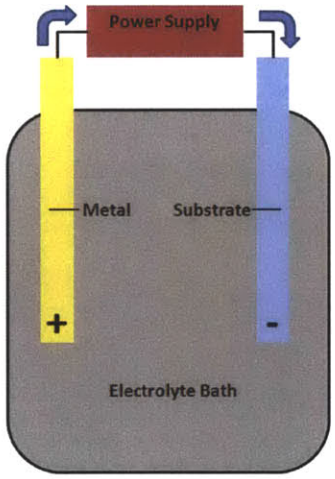

Figure A-6: Configuration of the electroplating system.

the metal and substrate, the metal ions diffuse to the substrate where they are deposited by accepting an electron and reverting to a metal. The plating process of time length τ for a metal of thickness T is described by the following [122]:

$$\frac{T}{\tau} = \frac{JE\alpha}{\rho} \tag{A.10}$$

where J represents the current density, E is the electrochemical equivalent, α is the current efficiency, and ρ represents the density of the deposited metal.

In order for electroplating to take place, the substrate surface must be conductive to the current. A thin seed layer of the metal, that will be electroplated, is deposited over the entire sample by either sputtering or evaporation and supports electron flow during the process. On top of the seed layer, a photoresist pattern is defined by image reversal prior to electroplating to protects areas on which a metal contacts is undesired. Some requirements of successful electroplating are:

- Clean substrate
- Conducting seed layer with no disconnects
- Plating solution that is compatible with all materials on the substrate
- Strong adhesion between the photoresist and the substrate

This method of deposition can achieve high aspect ratios and can fill densely-packed areas. However, the electroplating process can be crude, as contact to the substrate is made by alligator clips, and involves two contact photolithography steps (one for the ohmic or schottky metal contact, and another for the thicker electroplating deposition) as well as a wet etch to remove the seed layer beneath the photoresist. On uneven topography, the deposition of a uniform and seamless seed layer may also present a challenge to a successful electroplating process.

Electroless Plating

Electroless plating requires no current sources and operates in one of three ways: 1) Galvanic displacement, 2) an autocatalytic process, and 3) a substrate-catalyzed process. The later two methods include a reducing agent and can produce thick films of metal more than a few microns in thickness (in theory, an autocatalytic process should even continue indefinitely).

The deposition of Au using alkali borohydrides as a reducing agent is a multi-step reaction that requires excess free cyanide (CN^-) as a stabilizing agent. The $Au(CN)_2^-$ is reduced by BH_2OH^- through [123]:

$$BH_2OH^- + 3OH^- \rightarrow BO_3^- + \frac{3}{2}H_2 + 2H_2O + 3e^- \tag{A.11}$$

which combines with

$$Au(CN)_2^- + e^- \rightarrow Au(metal) + 2CN^- \tag{A.12}$$

to give

$$BH_2OH^- + 3Au(CN)_2^- + 3OH^- \rightarrow BO_3^- + \frac{3}{2}H_2 + 2H_2O + 3Au(metal) + 6CN^- \tag{A.13}$$

Electroless Au can be deposited on noble metals such as Au and Pd or on active metals, i.e. Cu and Ni. Inherently, the deposition process on noble metals is catalytic while on active metals it is driven by galvanic displacement. Au ions replace Ni atoms during galvanic replacement, and the process continues until the surface Ni atoms are depleted or covered by Au ions; therefore this is not an auto-catalytic process and typically terminates with layers that are less than 0.5μm thick. When used in conjunction with borohydride baths, even very thin Ni films (Ni concentration in the bath of $<10^{-1}$M) encourage bath decomposition and should hence be avoided [124].

Another disadvantage of galvanic displacement is the porous film quality which has shown greater diffusion of substrate metals upon heat treatment than that of films deposited by an electrolytic process [125]. This occurrence presents a formidable problem at the packaging stage, as the substrate metal (Ni in particular) can contaminate the plated surface by forming compounds, and lower the pull strength of wire bonding [126, 127]. The diffusion of Ni through to the Au layer can be minimized by depositing an intermediate layer of Pd between the two [127], or by including a plasma treatment to remove the Ni compound layer [128]. There are consequences to both of these options, as an intermediate Pd layer may alter the contact behavior and a plasma treatment can cause damage to the sample surface.

Appendix B

Fabrication Process Flows

B.1 n-i-n Modulator Process Flow Details

This section provides the details of the fabrication process of the n-i-n modulator that was discussed in Section 4.2.

Table B.1: Oxide chemical vapor deposition process

System	TRL STS-CVD
SiO_2 Thickness	100nm
N_2O Flow	1420 sccm (25%)
N_2 Flow	392 sccm (25%)
SiH_4 Flow	12 sccm (25%)
Power	30W
Frequency	13.56 MHz
Platen Temperature	250^oC
Showerhead Temperature	300^oC

Table B.2: Mask 1 - AZ5214 positive photoresist 1.5μm-thick photolithography process

System	TRL EV620
HMDS	Yes
Ramp Speed	750 rpm (6 sec)
Spin Speed	4000 rpm (30 sec)
Bake	95^oC (35 min)
Exposure Dosage	98mJ/cm^2
Development	AZ422 (90 sec)

Table B.3: AZ5214 curing/plasma ashing process

System	NSL Plasmatherm
Vacuum Cure	15 min
Glass Slide	Yes
He:O_2 RIE duration	(10 sec)
He:O_2 Flows	5:10 sccm
Pressure	20mT
Power	150W
Heating	No

Table B.4: SiO_2 RIE process with an AZ5214 protective etch mask

System	NSL Plasmatherm
Glass Slide	Yes
CF_4 Etch Rate	30nm/min
CF_4 Flows	15 sccm
Pressure	10mT
Voltage	50V
Heating	No

Table B.5: Removal process of the AZ5214 photoresist following the SiO_2 RIE

Solvent	Acetone
Solvent Rinse	Yes

Table B.6: HBr RIE for the removal of the top doped semiconductor layers

System	SNL Plasmatherm
Etch Rate	400nm/min
Gas	BCl_3
Gas Flow	15 sccm
Pressure	10mT
Voltage	325V
Plate Temperature	75^{o}C

Table B.7: Oxide chemical vapor deposition process for ICP-RIE etch mask

System	TRL STS-CVD
SiO_2 Thickness	200nm
N_2O Flow	1420 sccm (25%)
N_2 Flow	392 sccm (25%)
SiH_4 Flow	12 sccm (25%)
Power	30W
Frequency	13.56 MHz
Platen Temperature	250°C
Showerhead Temperature	300°C

Table B.8: Mask 2 - NR7-3000P negative photoresist 3μm-thick photolithography process

System	TRL EV620
Adhesion promoter application	No
Spin application photoresist	3 krpm, 40 sec
Hot plate bake	150°C, 1:00 min
Exposure dosage	680mJ/cm^2
Hot plate bake	100°C, 1:00 min
Development in RD6	18 sec

Table B.9: SiO_2 RIE process with an NR7-3000P etch mask

System	NSL Plasmatherm
Glass Slide	Yes
CF_4 Etch Rate	30nm/min
CF_4 Flows	15 sccm
Pressure	10mT
Voltage	50V
Heating	No

Table B.10: NR7-3000P negative photoresist stripping process

Step	Duration
Ultrasonic in Acetone	30 sec at level 1 (lowest)
Acetone Rinse	15 sec
Ultrasonic in Acetone	10 sec at level 2
Acetone Rinse	10 sec
Isopropanol Rinse	10 sec
Immerse in RR4 at 100°C	20 min

Table B.11: ICP-RIE process for GaAs-based materials

System	NSL SAMCO RIE-200iP
Plate Temperature	100°C
Pre-Conditioning Run Duration	15 min
$SiCl_4$:Cl_2:Ar Flows	10:0.5:50 sccm
Pressure	0.4 Pa
Bias	50W
ICP	100W
Etch Rate	0.8μm/min

Table B.12: AlAs oxidation process

System	Lincoln Labs oxidation furnace
Oxidation Rate	1.6μm/min
Furnace temperature	435°C

Table B.13: Benzocyclobutene application process

Adhesion Promoter	AP3000
Spin Application AP3000	Static Dispense; 300 rpm, 5 sec; 2.5 krpm 25 sec
Hotplate Bake AP3000	100°C, 5 min
BCB Formulation	3022-46
BCB Spin Application	Static Dispense; 500 rpm, 5 sec; 3.0 krpm 25 sec
Hotplate Bake BCB	100°C, 1:00 min

Table B.14: Benzocyclobutene furnace anneal process

System	EML diffusion furnace
N_2 >20 scfh Gas Flow	30 min
Anneal at 250°C, N_2=5 scfh	60 min
Hotplate Bake AP3000	100°C, 5 min
Cooling	120 min

Table B.15: Oxide chemical vapor deposition process for the etch of the Benzocyclobutene to expose the Mach-Zehnder Interferometer arms

System	TRL STS-CVD
SiO_2 Thickness	1000nm
N_2O Flow	1420 sccm (25%)
N_2 Flow	392 sccm (25%)
SiH_4 Flow	12 sccm (25%)
Power	30W
Frequency	13.56 MHz
Platen Temperature	250°C
Showerhead Temperature	300°C

Table B.16: Mask 3 - NR7-3000P negative photoresist 3μm-thick photolithography process

System	TRL EV620
Adhesion promoter application	No
Spin application photoresist	3 krpm, 40 sec
Hot plate bake	150°C, 1:00 min
Exposure dosage	680mJ/cm^2
Hot plate bake	100°C, 1:00 min
Development in RD6	18 sec

Table B.17: SiO_2 RIE process with an NR7-3000P etch mask

System	NSL Plasmatherm
Glass Slide	Yes
CF_4 Etch Rate	30nm/min
CF_4 Flows	15 sccm
Pressure	10mT
Voltage	50V
Heating	No

Table B.18: NR7-3000P negative photoresist stripping process

Ultrasonic in Acetone	30 sec at level 1 (lowest)
Acetone Rinse	15 sec
Ultrasonic in Acetone	10 sec at level 2
Acetone Rinse	10 sec
Isopropanol Rinse	10 sec
Immerse in RR4 at 100°C	20 min

Table B.19: Benzocyclobutene RIE etch back with the SiO_2 etch mask

System	NSL Plasmatherm
Glass Slide	No
Etch Rate	120nm/min
O_2/CF_4 Flows	20 sccm/8 sccm
Pressure	15mT
Voltage	500V
Heating	No

Table B.20: Hydrofluoric dip for removal of SiO_2 over the Mach-Zehnder Interferometer arms

Etch Rate High Frequency SiO_2 in HF	400nm/min
Duration	30 sec
Water Rinse	1:00 min

Table B.21: Mask 4 - NR7-1500PY negative photoresist 1.5μm-thick photolithography process

System	TRL EV620
Adhesion promoter application	No
Spin application photoresist	2 krpm, 40 sec
Hot plate bake	150°C, 1:00 min
Exposure dosage	810mJ/cm^2
Hot plate bake	100°C, 1:00 min
Development in RD6	20 sec

Table B.22: Top ohmic contact evaporation

System	NSL evaporator
Materials	Ge/Au/Ni/Au
Thicknesses	30nm/60nm/30nm/200nm

Table B.23: Lift off after top ohmic contact evaporation

Solvent	Acetone
Solvent Rinse	Yes

Table B.24: Bottom ohmic contact evaporation

System	NSL evaporator
Materials	Ge/Au/Ni/Au
Thicknesses	30nm/60nm/30nm/200nm

Table B.25: Anneal of ohmic contacts

System	IPDM oxidation furnace
Temperature	390°C
Duration	5min

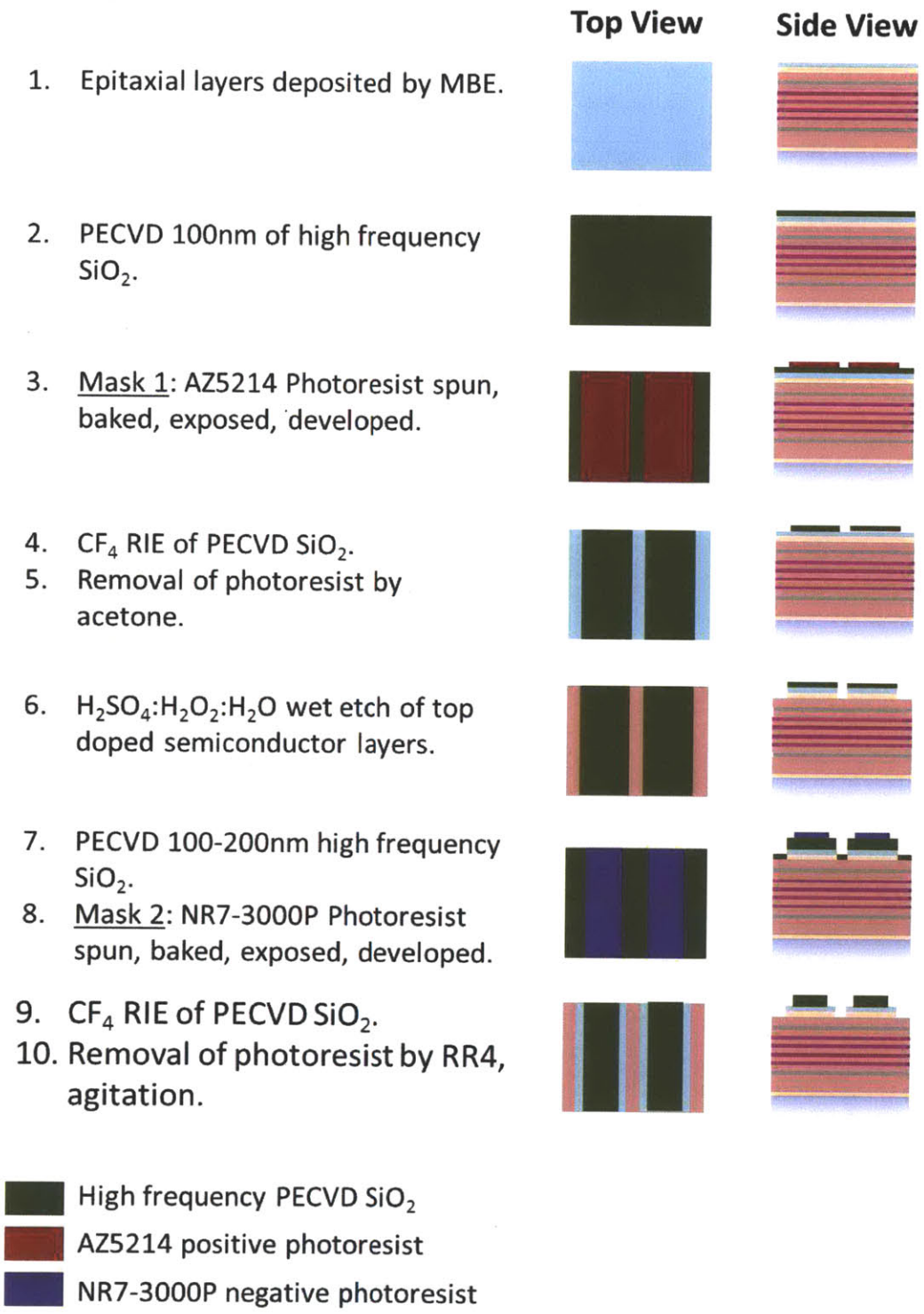

Figure B-1: Illustration of the n-i-n MOS modulator process flow (part 1 of 2).

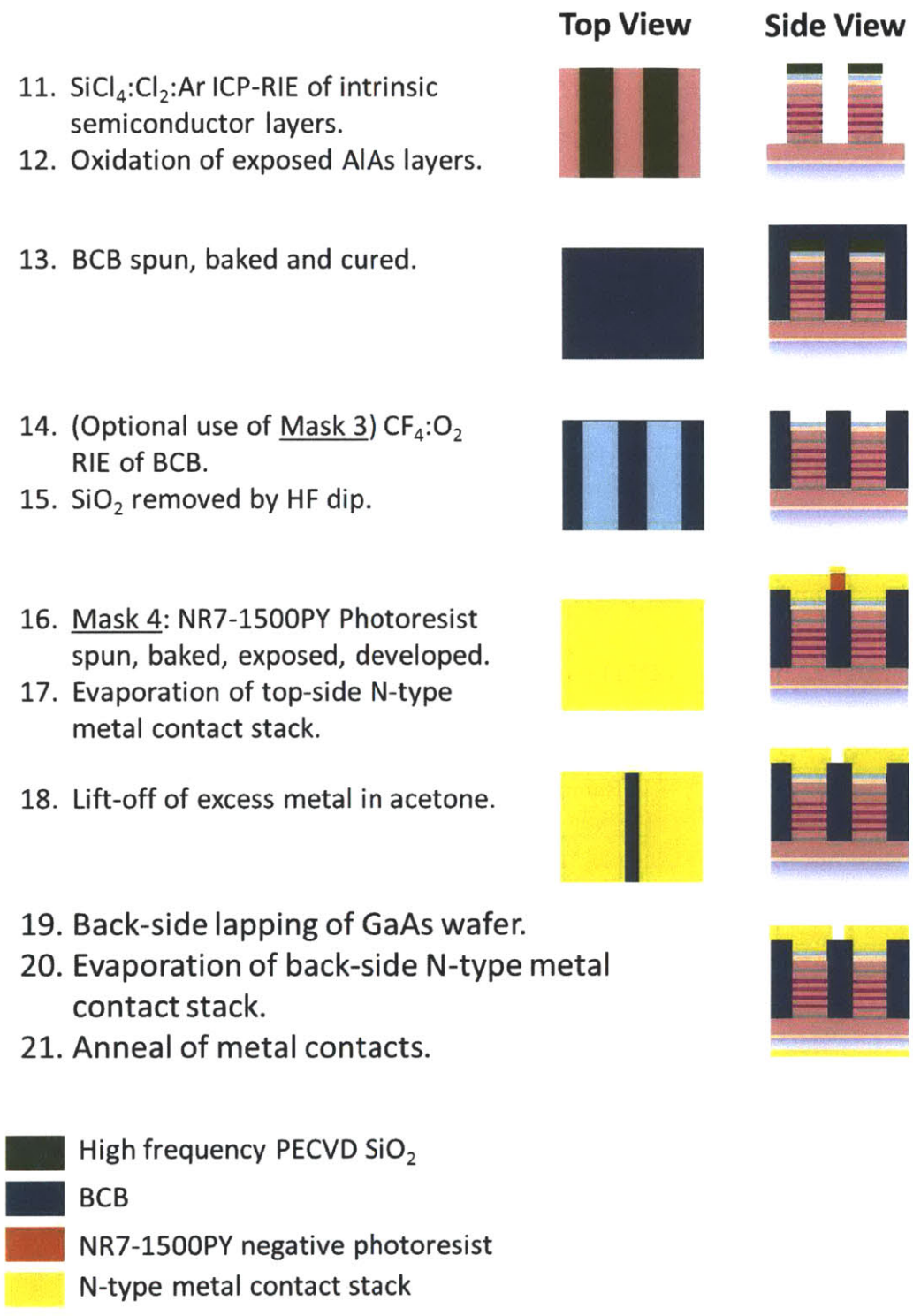

Figure B-2: Illustration of the n-i-n MOS modulator process flow (part 2 of 2).

B.2 Optimized Process Flow (Passive Components)

This section provides the details of the optimized fabrication process that was discussed in Section 4.4 and employed in the processing of passive components.

Table B.26: Oxide chemical vapor deposition process for wet etch mask

System	TRL STS-CVD
SiO_2 Thickness	100nm
N_2O Flow	1420 sccm (25%)
N_2 Flow	392 sccm (25%)
SiH_4 Flow	12 sccm (25%)
Power	30W
Frequency	13.56 MHz
Platen Temperature	250°C
Showerhead Temperature	300°C

Table B.27: Mask 1 - AZ5214 positive photoresist 1.5μm-thick photolithography process

System	TRL EV620
HMDS	Yes
Ramp Speed	750 rpm (6 sec)
Spin Speed	4000 rpm (30 sec)
Bake	95°C (35 min)
Exposure Dosage	98mJ/cm^2
Development	AZ422 (90 sec)

Table B.28: AZ5214 curing/plasma ashing process

System	NSL Plasmatherm
Vacuum Cure	15 min
Glass Slide	Yes
He:O_2 RIE duration	(10 sec)
He:O_2 Flows	5:10 sccm
Pressure	20mT
Power	150W
Heating	No

Table B.29: SiO_2 RIE process with an AZ5214 etch mask

System	NSL Plasmatherm
Glass Slide	Yes
CF_4 Etch Rate	30nm/min
CF_4 Flows	15 sccm
Pressure	10mT
Power	150W
Heating	No

Table B.30: Removal process of the AZ5214 photoresist following SiO_2 RIE

Solvent	Acetone
Solvent Rinse	Yes

Table B.31: Wet etching procedure for the removal of the top doped semiconductor layers

Etchants	$H_2SO_4/H_2O_2/H_2O$
Concentration Ratios	1:1:40
Etch Rate of $Al_{0.27}Ga_{0.73}As$	120μm/min

Table B.32: Oxide chemical vapor deposition process for ICP-RIE etch mask

System	TRL STS-CVD
SiO_2 Thickness	200nm
N_2O Flow	1420 sccm (25%)
N_2 Flow	392 sccm (25%)
SiH_4 Flow	12 sccm (25%)
Power	30W
Frequency	13.56 MHz
Platen Temperature	250^{o}C
Showerhead Temperature	300^{o}C

Table B.33: Mask 2 - NR7-3000P negative photoresist 3μm-thick photolithography process

System	TRL EV620
Adhesion promoter application	No
Spin application photoresist	3 krpm, 40 sec
Hot plate bake	80°C, 3:00 min
Exposure dosage	280mJ/cm^2
Hot plate bake	110°C, 70 sec
Development in RD6	13 sec

Table B.34: SiO_2 RIE process with an NR7-3000P etch mask

System	NSL Plasmatherm
Glass Slide	Yes
CF_4 Etch Rate	30nm/min
CF_4 Flows	15 sccm
Pressure	10mT
Power	150W
Heating	No

Table B.35: NR7-3000P negative photoresist stripping process

Ultrasonic in Acetone	30 sec at level 1 (lowest)
Acetone Rinse	15 sec
Ultrasonic in Acetone	10 sec at level 2
Acetone Rinse	10 sec
Isopropanol Rinse	10 sec
Immerse in RR4 at 100°C	20 min

Table B.36: ICP-RIE process of GaAs-based materials

System	NSL SAMCO RIE-200iP
Plate Temperature	100°C
Pre-Conditioning Run Duration	15 min
$SiCl_4$:Cl_2:Ar Flows	10:0.5:50 sccm
Pressure	0.4 Pa
Bias	50W
ICP	100W
Etch Rate	0.8μm/min

Table B.37: AlAs oxidation process

System	IPDM oxidation furnace
Oxidation Rate	1μm/min
Water Bath Temperature	80°C
Furnace temperature	420°C

Table B.38: Benzocyclobutene application process

Adhesion Promoter	No
BCB Formulation	3022-57
BCB Spin Application	Static Dispense; 500 rpm, 8 sec; 4.0 krpm, 30 sec
Hotplate Bake BCB	100°C, 1:00 min

Table B.39: Benzocyclobutene furnace anneal process

System	EML diffusion furnace
N_2 >20 scfh Gas Flow	30min
Temperature Ramp 1, N_2 = 5scfh	100°C, hold for 10 min
Temperature Ramp 2	150°C, hold for 20 min
Temperature Ramp 3	200°C, hold for 10 min
Temperature Ramp 4	250°C, hold for 120 min
Cooling	120 min

The placement of the planarized substrate on the quartz boat in preparation for the annealing process is crucial. Given the smaller sample sizes (2" wafers that must sit on a 4" boat), a 4" Si wafer is laid on the boat, and the sample is placed on top. Due to BCB reflow during the duration of the cure, the substrate edges should not come in direct contact with the Si wafer as the BCB will engulf the edges and harden, effectively bonding the two wafers. One solution is to place smaller pieces of Si wafer on which the planarized substrate can "float" (see Figure B-3(a)). If multiple pieces are used and placed toward

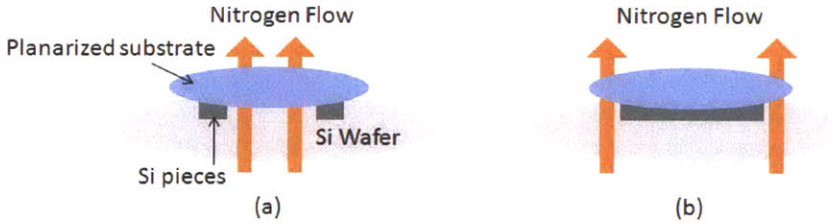

Figure B-3: Placement of the planarized substrate during the BCB hard cure step. The substrate is set on pieces of Si wafer atop a 4" Si wafer that lies on a quartz boat. (a) If multiple supporting pieces of Si are used the open area underneath the substrate will allow a flow of nitrogen to cools the sample and build stress in the BCB layer. (b) The substrate is alternately placed on top of a single piece of Si that covers the majority of the substrate area without extending to the edges, eliminating the cooling flow and minimizing built-up stress in the film.

the perimeter of the substrate, the open area underneath the substrate will allow a flow of nitrogen to pass that cools the sample. The temperature drop builds a significant amount of stress in the BCB layer, to the point where during any subsequent cleaves, the fracture energy is exceeded by the energy applied to the film, and the adhesion of the layer simply fails and delaminates [129]. If the substrate is alternately placed on top of a piece of Si that covers the majority of the substrate area without extending to the edges (Figure B-3(b)), the sample is not cooled and stress in the BCB film is minimized.

Table B.40: Mask 5 - NR7-3000P negative photoresist 3μm-thick process, facet etch mask

System	TRL EV620
Adhesion promoter application	No
Spin application photoresist	3 krpm, 40 sec
Hot plate bake	150°C, 1:00 min
Exposure dosage	680mJ/cm^2
Hot plate bake	100°C, 1:00 min
Development in RD6	13 sec

Table B.41: Benzocyclobutene RIE etch back over facets

System	NSL Plasmatherm
Glass Slide	No
Etch Rate	120nm/min
O_2/CF_4 Flows	16 sccm/8 sccm
Pressure	15mT
Voltage	500V
Heating	No

B.3 Mask Layouts

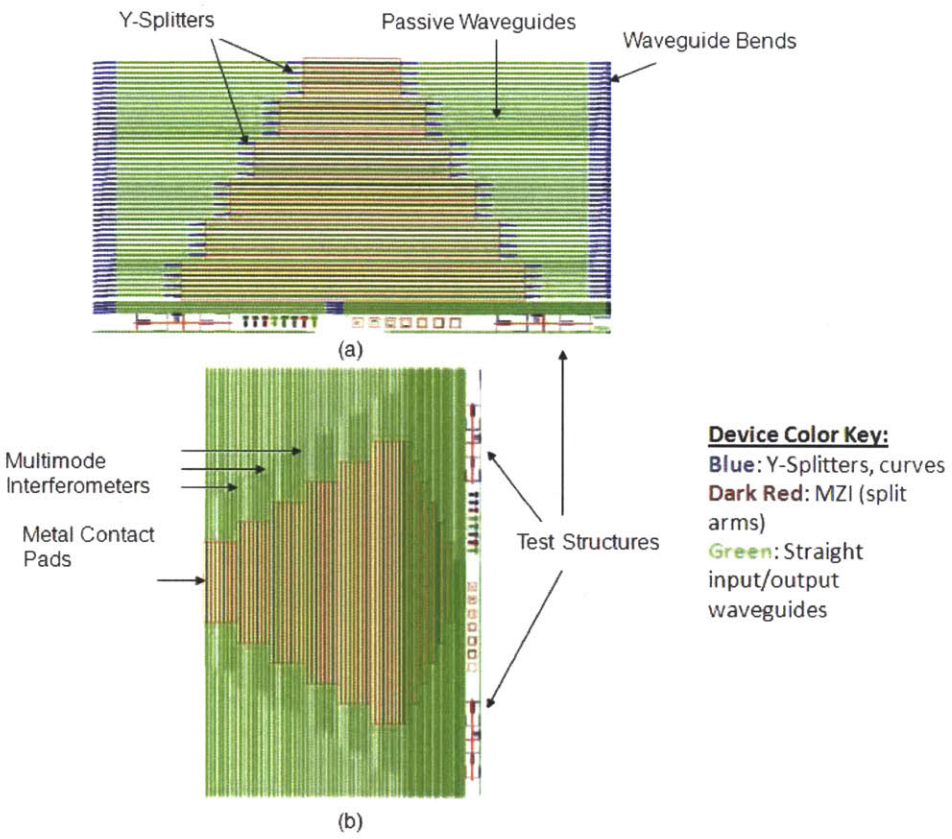

Figure B-4: Magnified view of the device dies on the n-i-n MOS mask set.

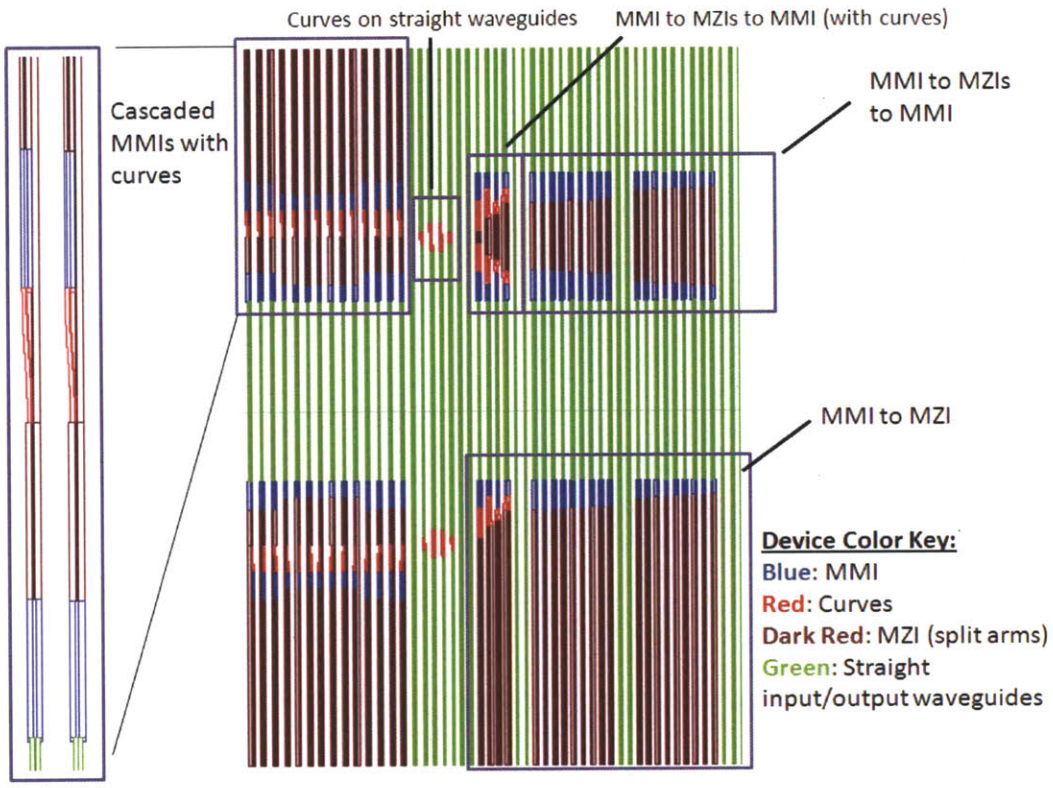

Figure B-5: Magnified view of the device dies on the MMI mask.

References

[1] Center for Free-Electron Laser Science. http://desy.cfel.de/.

[2] O.A. Shamir. Development of Ultra-Broadband Modulators. Master's thesis, Cambridge, MA, 2008.

[3] T.H. Maiman. Stimulated Optical Radiation in Ruby. *Nature*, 187(4736):493–494, 1960.

[4] F. Tavernier and M. Steyaert. *High-Speed Optical Receivers with Integrated Photodiode in Nanoscale CMOS*. Springer, New York, 2011.

[5] T. He, N.K. Fontaine, R.P. Scott, D.J. Geisler, J.P. Heritage, and S. Yoo. Optical Arbitrary Waveform Generation-Based Packet Generation and All-Optical Separation for Optical-Label Switching. *Photonics Technology Letters*, 22(10):715–717, 2010.

[6] M.J.R. Heck, P. Munoz, B.W. Tilma, E.A.J.M. Bente, Y. Barbarin, Y.-S. Oei, R. Notzel, and M.K. Smit. Design, Fabrication and Characterization of an InP-Based Tunable Integrated Optical Pulse Shaper. *Quantum Electronics, IEEE Journal of*, 44(4):370 –377, 2008.

[7] F.M. Soares, J.H. Baek, N.K. Fontaine, X. Zhou, Y. Wang, R.P. Scott, J.P. Heritage, C. Junesand, S. Lourdudoss, K.Y. Liou, R.A. Hamm, W. Wang, B. Patel, S. Vatanapradit, L.A. Gruezke, W.T. Tsang, and S.J. Yoo. Monolithically Integrated InP Wafer-Scale 100-Channel x 10-GHz AWG and Michelson Interferometers for 1-THz-Bandwidth Optical Arbitrary Waveform Generation. In *Optical Fiber Communication Conference*. Optical Society of America, 2010.

[8] M.A. Dugan, J.X. Tull, and W.S. Warren. High-Resolution Acousto-Optic Shaping of Unamplified and Amplified Femtosecond Laser Pulses. *J. Opt. Soc. Am. B*, 14(9):2348–2358, 1997.

[9] M.M. Wefers and K.A. Nelson. Generation of High-Fidelity Programmable Ultrafast Optical Waveforms. *Opt. Lett.*, 20(9):1047–1049, 1995.

[10] A.M. Weiner, D.E. Leaird, J.S. Patel, and J.R. Wullert II. Programmable Shaping of Femtosecond Optical Pulses by Use of 128-Element Liquid Crystal Phase Modulator. *Quantum Electronics, IEEE Journal of*, 28(4):908–920, 1992.

[11] J. Chou, Y. Han, and B. Jalali. Adaptive RF-Photonic Arbitrary Waveform Generator. *Photonics Technology Letters*, 15(4):581–583, 2003.

[12] J.W. Sickler. *High Repetition Rate Mode-Locked Erbium-Doped Fiber Lasers with Complete Electric Field Control.* PhD thesis, Cambridge, MA, 2008.

[13] F. Zeng and J. Yao. An Approach to Ultrawideband Pulse Generation and Distribution Over Optical Fiber. *Photonics Technology Letters*, 18(7):823–825, 2006.

[14] Y. Dai, X. Chen, H. Ji, and S. Xie. Optical Arbitrary Waveform Generation Based on Sampled Fiber Bragg Gratings. *Photonic Technology Letters*, 19(23):1916–1918, 2007.

[15] D.J. Geisler, N.K. Fontaine, R.P. Scott, T. He, L. Paraschis, J.P. Heritage, and S.J.B. Yoo. 400-Gb/s Modulation-Format-Independent Single-Channel Transmission With Chromatic Dispersion Precompensation Based on OAWG. *Photonics Technology Letters, IEEE*, 22(12):905–907, 2010.

[16] D.J. Geisler, N.K. Fontaine, T. He, R.P. Scott, L. Paraschis, J.P. Heritage, and S.J.B. Yoo. Modulation-Format Agile, Reconfigurable Tb/s Transmitter Based on Optical Arbitrary Waveform Generation. *Opt. Express*, 17(18):15911–15925, 2009.

[17] N.K. Fontaine, D.J. Geisler, R.P. Scott, C. Yang, F.M. Soares, A. Karalar, J. Yang, K. Okamoto, J.P. Heritage, and S.B. Yoo. High-Resolution, Loop-Back AWG for Compact, High-Fidelity, Optical Arbitrary Waveform Generation. In *Technical Digest of IEEE/OSA Optical Fiber Communication Conference*, 2008.

[18] S.T. Cundiff and A.M. Weiner. Optical Arbitrary Waveform Generation. *Nature Photonics*, 4:760–766, 2010.

[19] A.M. Weiner. Femtosecond Pulse Shaping Using Spatial Light Modulators. *Review of Scientific Instruments*, 71(5):1929–1960, 2000.

[20] P.F. Moulton. Spectroscopic and Laser Characteristics of Ti:Al_2O_3. *J. Opt. Soc. Am. B*, 3(1):125–133, Jan 1986.

[21] A.J. Benedick, U. Demirbas, D. Li, J.G. Fujimoto, and F.X. Kartner. Attosecond Ti:Sapphire Pulse Train Phase Noise. In *2011 Conference on Lasers and Electro-Optics (CLEO)*, pages 1–2, may 2011.

[22] E. Ippen, A. Benedick, J. Birge, H. Byun, L.-J. Chen, G. Chang, D. Chao, J. Morse, A. Motamedi, M. Sander, G. Petrich, L. Kolodziejski, and F. Kartner. Optical Arbitrary Waveform Generation. In *2010 Conference on Lasers and Electro-Optics (CLEO) and Quantum Electronics and Laser Science Conference (QELS)*, pages 1–2, May 2010.

[23] M.Y. Sander, E.P. Ippen, and F.X. Kärtner. Carrier-Envelope Phase Dynamics of Octave-Spanning Dispersion-Managed Ti:Sapphire Lasers. *Opt. Express*, 18(5):4948–4960, 2010.

[24] E. P. Ippen. Principles of Passive Mode Locking. *Applied Physics B: Lasers and Optics*, 58(3):159–170, 1994.

[25] K. Lau. *Ultra-high Frequency Linear Fiber Optic Systems.* Springer, Berlin, 2011.

[26] R.G. Hunsperger. Losses in Optical Waveguides. In *Integrated Optics*. Springer New York, 2009.

[27] G. Schiellerup, R.J.S. Pedersen, H. Olesen, and B. Tromborg. Center Frequency Shift and Reduction of Feedback in Directly Modulated External Cavity Lasers. *Photonics Technology Letters, IEEE*, 1(10):288–290, 1989.

[28] N. Dagli. *High-Speed Photonic Devices*. CRC Press, Boca Raton, FL., 2007.

[29] R.C. Alferness. Waveguide Electrooptic Modulators. *IEEE Transactions on Microwave Theory Techniques*, 30(8):1121–1137, 1982.

[30] J. Dakin and R.G.W. Brown. *Handbook of Optoelectronics*. CRC Press, Boca Raton, FL., 2006.

[31] L. Pavesi and G. Guillot. *Optical Interconnects: The Silicon Approach*. Springer, Netherlands, 2006.

[32] I. Kang, S. Chandrasekhar, L. Buhl, P.G. Bernasconi, X. Liu, G. Raybon, C.R. Giles, C. Kazmierski, N. Dupuis, J. Decobert, F. Alexandre, C. Jany, A. Garreau, J. Landreau, M. Rasras, M. Cappuzzo, L.T. Gomez, Y.F. Chen, M.P. Earnshaw, J. Lee, and A. Leven. Pulse-Carver-Free 50-Gb/s RZ-DQPSK Generation Using Hybrid Photonic-Integrated Electroabsorption Modulators. In *34th European Conference on Optical Communication, 2008*, pages 1–2, Sept. 2008.

[33] Y. Kawamura, K. Wakita, Y. Itaya, Y. Yoshikuni, and H. Asahi. Monolithic Integration of InGaAs/InP DFB Lasers and InGaAs/InAlAs MQW Optical Modulators. *Electronics Letters*, 22(5):242–243, 1986.

[34] A.K. Dutta, N.K. Dutta, and M. Fujiwara. *WDM Technologies: Active Optical Components*. Elsevier Academic Press, Burlington, MA, 2004.

[35] B. Knüpfer, P. Kiesel, M. Kneissl, S. Dankowski, N. Linder, and G. Weimann. Polarization-Insensitive High-Contrast GaAs/AlGaAs Waveguide Modulator Based on the Franz-Keldysh Effect. *Photonics Technology Letters*, 5(12):1386–1388, 1993.

[36] T.H. Wood, C.A. Burrus, D.A.B. Miller, D.S. Chemla, T.C. Damen, A.C. Gossard, and W. Wiegmann. High-Speed Optical Modulation with GaAs/AlGaAs Quantum Wells in a p-i-n Diode Structure. *Applied Physics Letters*, 44(1):16–18, 1984.

[37] M.S. Tobin and J.D. Bruno. Quantum-Confined Stark Effect Modulator Based on Multiple Triple-Quantum Wells. *Journal of Applied Sciences*, 89(3):1885–1889, 2001.

[38] M. Jarrahi, T.H. Lee, and D.A.B. Miller. Wideband, Low Driving Voltage Traveling-Wave Mach-Zehnder Modulator for RF Photonics. *Photonics Technology Letters, IEEE*, 20(7):517–519, 2008.

[39] C.R. Pollock. *Fundamentals of Optoelectronics*. Irwin, Chicago, 1995.

[40] P. Bhattacharya. *Semiconductor Optoelectronic Devices*. Prentice-Hall, Englewood Cliffs, N.J., 1994.

[41] H.G. Bach, J. Krauser, H.P. Nolting, R.A. Logan, and F.K. Reinhart. Electro-Optical Light Modulation in InGaAsP/InP Double Heterostructure Diodes. *Applied Physics Letters*, 42(8):692–694, 1983.

[42] F.K. Reinhart and B.I. Miller. Efficient GaAs/$Al_xGa_{1-x}As$ Double-Heterostructure Light Modulators. *Applied Physics Letters*, 20(1):36–38, 1972.

[43] J.E. Zucker, K.L. Jones, B.I. Miller, M.G. Young, U. Koren, J.D. Evankow, and C.A. Burrus. Zero-Loss Quantum Well Waveguide Mach-Zehnder Modulator at 1.55μm. *Applied Physics Letters*, 60(3):277–279, 1992.

[44] K. Tsuzuki, H. Ishibashi, Yasaka, and Y. Tohmori. InP-based n-i-n Mach-Zehnder Optical Modulator. *Electronics and Communications in Japan, Part 2*, 88(8):1–9, 2003.

[45] B.E.A. Saleh and M.C. Teich. *Fundamentals of Photonics.* John Wiley and Sons, New York, 1991.

[46] H.A. Haus. *Waves and Fields in Optoelectronics.* Prentice-Hall, Englewood Cliffs, NJ, 1984.

[47] J.-M. Liu. *Photonic Devices.* Cambridge University Press, Cambridge; New York, 2005.

[48] O. Solgaard. *Photonic Microsystems: Micro and Nanotechnology Applied to Optical Devices and Systems.* Springer, New York; London, 2009.

[49] M.N. Khan, W. Yang, and A. Gopinath. Directional Coupler Electro-Optic Modulator in AlGaAs/GaAs with Low Voltage-Length Product. *Applied Physics Letters*, 62(17):2033–2035, 1993.

[50] L. Zehnder. *Z. Instrumentenkunde*, 11:275, 1891.

[51] L. Mach. *Z. Instrumentenkunde*, 12:89, 1892.

[52] J.C. Whitaker. *The Electronics Handbook.* CRC Press, Boca Raton, FL., 2005.

[53] R. Alferness, C. Joyner, L. Buhl, and S. Korotky. High-Speed Traveling-Wave Directional Coupler Switch/Modulator for λ=1.32μm. *Quantum Electronics, IEEE Journal of*, 19(9):1339–1341, 1983.

[54] Y. Cui and P. Berini. Modeling and Design of GaAs Traveling-Wave Electrooptic Modulators Based on Capacitively Loaded Coplanar Strips. *J. Lightwave Technol.*, 24(1):544, 2006.

[55] E.F. Schubert. *Light Emitting Diodes.* Cambridge University Press, Cambridge, UK; New York, 2003.

[56] R. Spickermann, M.G. Peters, and N. Dagli. A Polarization Independent GaAs-AlGaAs Electrooptic Modulator. *Quantum Electronics, IEEE Journal of*, 32(5):764–769, 1996.

[57] S.R. Sakamoto, R. Spickermann, and N. Dagli. Narrow Gap Coplanar Slow Wave Electrode for Travelling Wave Electro-Optic Modulators. *Electronics Letters*, 31(14):1183–1185, 1995.

[58] S.R. Sakamoto, A. Jackson, and N. Dagli. Substrate Removed GaAs-AlGaAs Electrooptic Modulators. *Photonics Technology Letters*, 11(10):1244–1246, 1999.

[59] J. Shin, S. Wu, and N. Dagli. Bulk Undoped GaAs-AlGaAs Substrate-Removed Electrooptic Modulators With 3.7-V-cm Drive Voltage at 1.55μm. *Photonics Technology Letters*, 18(21):2251–2253, 2006.

[60] C. Rolland, R.S. Moore, F. Shepherd, and G. Hillier. 10Gbit/s, 1.56μm Multiquantum Well InP/InGaAsP Mach-Zehnder Optical Modulator. *Electronic Letters*, 29(5):471–472, 1993.

[61] S. Akiyama, S. Hirose, T. Watanabe, M. Ueda, S. Sekiguchi, T. Morii, N. Yamamoto, A. Kuramata, and H. Soda. Novel InP-based Mach-Zehnder Modulator for 40Gb/s Integrated Light Source. In *Conf. Dig. 2002 IEEE Int. Semiconductor Laser Conf. (ISLC 2002)*, pages 57–58, 2002.

[62] J.S. Cites and P.R. Ashley. High-Performance Mach-Zehnder Modulators in Multiple Quantum Well GaAs/AlGaAs. *Lightwave Technology, Journal of*, 12(7):1167–1173, 1994.

[63] P.W. Juodawlkis, F.J. O'Donnell, R.J. Bailey, J.J. Plant, K.G. Ray, D.C. Oakley, A. Napoleone, and G.E. Betts. Sub-Volt-V_π InGaAsP Electrorefractive Modulators Using Symmetric, Uncoupled Quantum Wells. In *Lasers and Electro-Optics Society*, pages 788–789, 2003.

[64] K. Tsuzuki, T. Ishibashi, T. Ito, S. Oku, Y. Shibata, R. Iga, Y. Kondo, and Y. Tohmori. 40 Gb/s n-i-n InP Mach-Zehnder Modulator with a π Voltage of 2.2V. *Electronic Letters*, 39(20):1464–1466, 2003.

[65] K. Tsuzuki, T. Ishibashi, T. Ito, S. Oku, Y. Shibata, T. Ito, R. Iga, Y. Kondo, and Y. Tohmori. A 40 Gb/s InGaAlAs-InAlAs MQW n-i-n Mach-Zehnder Modulator with a Drive Voltage of 2.3V. *Photonic Technology Letters*, 17(1):46–48, 2005.

[66] Luxpop Thin Film and Bulk Index of Refraction and Photonics Calculations. http://luxpop.com.

[67] R-Soft BeamPROP Simulation Software. http://www.rsoftdesign.com/.

[68] S.S. Lee, R.V. Ramaswamy, and V.S. Sundaram. Analysis and Design of High-speed High-Efficiency GaAs-AlGaAs Double-Heterostructure Waveguide Phase Modulator. *Lightwave Technology, Journal of*, 27(3):726–736, 1991.

[69] J.G. Mendoza-Alvarez, L.A. Coldren, A. Alping, R.H. Yan, T. Hausken, K. Lee, and K. Pedrotti. Analysis of Depletion Edge Translation Lightwave Modulators. *Lightwave Technology, Journal of*, 6(6):793–808, 1988.

[70] W. Choi. Investigation of the Quadratic Electrooptic Effect in GaAs/AlGaAs Optical Modulator on p-i-n Rib Waveguide. In *Integrated Photonics Research*. Optical Society of America, 2001.

[71] M. Erman, P. Jarry, R. Gamonal, P. Autier, J.-P. Chane, and P. Frijlink. Mach-Zehnder Modulators and Optical Switches on III-V Semiconductors. *Lightwave Technology, Journal of*, 6(6):837–846, 1988.

[72] P.A. Besse, M. Bachmann, H. Melchior, L.B. Soldano, and M.K. Smit. Optical Bandwidth and Fabrication Tolerances of Multimode Interference Couplers. *Lightwave Technology, Journal of*, 12(6):1004–1009, 1994.

[73] J.M. Heaton, R.M. Jenkins, D.R. Wight, J.T. Parker, J.C.H. Birbeck, and K.P. Hilton. Novel 1-to-N Way Integrated Optical Beam Splitters Using Symmetric Mode Mixing in GaAs/AlGaAs Multimode Waveguides. *Applied Physics Letters*, 61(15), 1992.

[74] P. Buchmann, H. Kaufmann, H. Melchior, and G. Guekos. Broadband Y-Branch Electrooptic GaAs Waveguide Interferometer for 1.3μm. *Applied Physics Letters*, 46(5):462–464, 1985.

[75] P. Buchmann and A.J.N. Houghton. Optical Y-Junctions and S-Bends Formed by Preferentially Etched Single-Mode Rib Waveguides in InP. *Electronics Letters*, 18(19):850–852, 1982.

[76] J.C. Campbell, F.A. Blum, D.W. Shaw, and K.L. Lawley. GaAs Electro-Optic Directional-Coupler Switch. *Applied Physics Letters*, 27(4):202–205, 1975.

[77] J.C. Shelton, F.K. Reinhart, and R.A. Logan. Rib Waveguide Switches with MOS Electrooptic Control for Monolithic Integrated Optics in GaAs-$Al_xGa_{1-x}As$. *Appl. Opt.*, 17(16):2548–2555, 1978.

[78] F.J. Leonberger, J.P. Donnelly, and C.O. Bozler. GaAs p+n-n+ Directional-Coupler Switch. *Applied Physics Letters*, 29(10):652–654, 1976.

[79] J. Donnelly, N. DeMeo, and G. Ferrante. Three-Guide Optical Couplers in GaAs. *Lightwave Technology, Journal of*, 1(2):417–424, 1983.

[80] J.P. Donnelly, N.L. DeMeo, G.A. Ferrante, K.B. Nichols, and F.J. O'Donnell. Optical Guided-Wave Gallium Arsenide Monolithic Interferometer. *Applied Physics Letters*, 45(4):360–362, 1984.

[81] F.J. Leonberger, J.P. Donnelly, and C.O. Bozler. Wavelength Dependence of GaAs Directional Couplers and Electrooptic Switches. *Appl. Opt.*, 17(14):2250–2254, 1978.

[82] L.B. Soldano and E.C.M. Pennings. Optical Multi-Mode Interference Devices Based on Self-Imaging: Principles and Applications. *Lightwave Technology, Journal of*, 13(4):615–627, 1995.

[83] E.J. Murphy. *Integrated Optical Circuits and Components: Design and Applications.* Marcel Dekker, New York, 1999.

[84] D.S. Levy, Y.M. Li, R. Scarmozzino, and R.M. Osgood Jr. A Multimode Interference-Based Variable Power Splitter in GaAs-AlGaAs. *Photonics Technology Letters, IEEE*, 9(10):1373–1375, 1997.

[85] Optiwave OptiBPM Simulation Software. http://www.optiwave.com/.

[86] R.D. Williams. *Photonic Integrated Circuits for Optical Logic Applications.* PhD thesis, MIT, Cambridge, MA, 2007.

[87] A. Liu, R. Jones, L. Liao, D. Samara-Rubio, D. Rubin, O. Cohen, R. Nicolaescu, and M. Paniccia. A High-Speed Silicon Optical Modulator Based on a Metal-Oxide-Semiconductor Capacitor. *Nature*, 427:615–618, 2004.

[88] Q. Xu, B. Schmidt, S. Pradhan, and M. Lipson. Micrometre-Scale Silicon Electro-Optic Modulator. *Nature*, 435:325–327, 2005.

[89] Device Simulation Framework to Simulate Electrical, Optical, and Thermal Behavior of Semiconductor Devices. http://www.silvaco.com.

[90] F. Argall and A.K. Jonscher. Dielectric Properties of Thin Films of Aluminium Oxide and Silicon Oxide. *Thin Solid Films*, 2(3):185 – 210, 1968.

[91] S. Adachi. GaAs, AlAs, and $Al_xGa_{1-x}As$ B: Material Parameters for Use in Research and Device Applications. *Journal of Applied Physics*, 58(3):R1–R29, 1985.

[92] S. Gehrsitz, F. K. Reinhart, C. Gourgon, N. Herres, A. Vonlanthen, and H. Sigg. The Refractive Index of $Al_xGa_{1-x}As$ Below the Band Gap: Accurate Determination and Empirical Modeling. *Journal of Applied Physics*, 87(11):7825–7837, 2000.

[93] K. Hikosaka, T. Mimura, and K. Joshin. Selective Dry Etching of AlGaAs-GaAs Heterojunction. *Japanese Journal of Applied Physics*, 20(11):L847–L850, 1981.

[94] J.W. Lee, M.W. Devre, B.H. Reelfs, D. Johnson, J.N. Sasserath, F. Clayton, D. Hays, and S.J. Pearton. Advanced Selective Dry Etching of GaAs/AlGaAs in High Density Inductively Coupled Plasmas. volume 18, pages 1220–1224. AVS, 2000.

[95] A.R. Pratt, T. Takamori, and T. Kamijoh. Photoluminescence of InGaAs/GaAs Single Quantum Well Adjacent to a Selectively Oxidized AlAs Layer. *Applied Physics Letters*, 71(10):1394–1396, 1997.

[96] P. Chavarkar, L. Zhao, S. Keller, A. Fisher, C. Zheng, J.S. Speck, and U.K. Mishra. Strain Relaxation of $In_xGa_{1-x}As$ During Lateral Oxidation of Underlying AlAs Layers. *Applied Physics Letters*, 75(15):2253–2255, 1999.

[97] H.-E. Shin, Y.-G. Ju, H.-W. Song, D.-S. Song, I.-Y. Han, J.-H. Ser, H.-Y. Ryu, Y.-H. Lee, and H.-H. Park. High-Finesse Al_xO_y/AlGaAs Nonabsorbing Optical Cavity. *Applied Physics Letters*, 72(18):2205–2207, 1998.

[98] H.J. Levinson. *Principles of Lithography.* SPIE Press, Bellingham, WA., 2005.

[99] V. Van, P.P. Absil, J.V. Hryniewicz, and P.-T. Ho. Propagation Loss in Single-Mode GaAs-AlGaAs Microring Resonators: Measurement and Model. *Lightwave Technology, Journal of*, 19(11):1734–1739, 2001.

[100] J.W. Lee and S.J. Pearton. Investigation of Masking Materials for High Ion Density Cl_2/Ar Plasma Etching of GaAs. *Semicond. Sci. Technol.*, 11:812–815, 1991.

[101] R.J. Shul and S.J. Pearton. *Handbook of Advanced Plasma Processing Techniques.* Springer, Berlin; New York, 2000.

[102] P.K. Tien. Light Waves in Thin Films and Integrated Optics. *Appl. Opt.*, 10(11):2395–2413, 1971.

[103] R.J. Deri and E. Kapon. Low-Loss III-V Semiconductor Optical Waveguides. *Quantum Electronics, IEEE Journal of*, 27(3):626–640, 1991.

[104] L.B. Rothman. Properties of Thin Polyimide Films. *Journal of The Electrochemical Society*, 127(10):2216–2220, 1980.

[105] T.M. Stokich, C.C. Fulks, M.T. Bernius, and D.C. Burdeaux. Planarization with Cylotene 3022 (BCB) Polymer Coatings. In *Material Research Society Symposium Proceedings*, volume 308, pages 517–526, 1993.

[106] R.G. Walker. High-Speed III-V Semiconductor Intensity Modulators. *Journal of Quantum Electronics*, 27(3):654–667, 1991.

[107] L.L. Chang and K. Ploog. *Molecular Beam Epitaxy and Heterostructure.* Springer, 1985.

[108] R.S. Rosler, W.C. Benzing, and J.A. Baldo. Carrier Transport Across Metal-Semiconductor Barriers. *Solid State Technology*, 19(6):45, 1976.

[109] C.Y. Chang and F. Kai. *GaAs High-Speed Devices.* John Wiley and Sons, INC., 1994.

[110] R.E. Williams. *Gallium Arsenide Processing Techniques.* Artech House, Boston, 1985.

[111] C.H. Ling, C.Y. Kwok, and K. Prasad. Silicon Nitride Films Prepared by Plasma-Enhanced Chemical Vapour Deposition (PECVD) of $SiH_4/NH_3/N_2$ Mixtures: Some Physical Properties. *Japanese Journal of Applied Physics*, 25(10).

[112] J.W. Lee, M.W. Devre, B.H. Reelfs, D. Johnson, J.N. Sasserath, F. Clayton, D. Hays, and S.J. Pearton. Advanced Selective Dry Etching of GaAs/AlGaAs in High Density Inductively Coupled Plasmas. *Journal of Vacuum Science and Technology A*, 18(4):1220–1224, 2000.

[113] Z. Cui. *Micro-Nanofabrication Technologies and Applications.* Springer, Berlin, 2005.

[114] F. Laermer and A. Schilp. Method of Anisotropically Etching Silicon. US-Patent No. 5501 893.

[115] R. Kirchoff, C. Carriere, K. Bruza, N. Rondan, and R. Sammler. Benzocyclobutenes: A New Class of High Performance Polymers. *Journal of Macromolecular Science. Part A: Pure and Applied Chemistry*, 28:1079–1113, 1991.

[116] M. Schier. Reactive Ion Etching of Benzocyclobutene Using a Silicon Nitride Dielectric Etch Mask. *Journal of The Electrochemical Society*, 142(9):3238–3240, 1995.

[117] C.Y. Chang and S.M. Sze. Carrier Transport Across Metal-Semiconductor Barriers. *Solid State Electronics*, 13:727–740, 1970.

[118] J.M. Poate, K.-N. Tu, and J.W. Mayer. *Thin Films: Interdiffusion and Reactions.* John Wiley and Sons, INC., 1978.

[119] G.Y. Robinson. *Physics and Chemistry of III-V Compound Semiconductor Interfaces.* C.W. Wilmsen, Plenum Press, 1985.

[120] M. Ogawa. Alloying Behavior of Ni/Au-Ge Films on GaAs. *Journal of Applied Physics*, 51(1):406–412, 1980.

[121] A.M. Andrews and N. Holonyak Jr. Properties of n Type Ge-Doped Epitaxial GaAs Layers Grown from Au-Rich Melts. *Solid-State Electronics*, 15(6):601–604, 1972.

[122] A. Elshabini-Riad and F.D. Barlow III. *Thin Film Technology Handbook.* McGraw-Hill, New York, 1998.

[123] Y. Okinaka. *Gold Plating Technology.* Electrochemical Publications Ltd., 1974.

[124] Y. Okinaka. *Electroless Plating: Fundamentals and Applications.* Cambridge University Press, Scotland, 1990.

[125] R. Asher. The Potentialities of Electroless Gold Plating of Transistor Headers. *Gold Bulletin*, 13(1):7–8, 1980.

[126] R.W. Johnson, M.J. Palmer, M.J. Bozack, and T. Isaacs-Smith. Thermosonic Gold Wire Bonding to Laminate Substrates with Palladium Surface Finishes. *Electronics Packaging Manufacturing, IEEE Transactions on*, 22(1):7–15, 1999.

[127] K. Hasegawa, A. Takahashi, and A. Nakaso. Electroless Gold Plating For Semiconductor Package Substrate. In *IEMT/IMC Symposium, 1997., 1st [Joint International Electronic Manufacturing Symposium and the International Microelectronics Conference]*, pages 230–233, April 1997.

[128] R. Furukawa. Realizing Low Cost and High Reliability in CSP Packages with Surface Treatment and Material Technology - Plasma Treatment Technology. In *Electronics Manufacturing Technology Symposium, 2004. IEEE/CPMT/SEMI 29th International*, pages 177–179, 2004.

[129] J.-h. Im, E.O. Shaffer II, O. Stokich Jr., A. Strandjord, J. Hetzner, J. Curphy, C. Karas, G. Meyers, D. Hawn, A. Chakrabarti, and S. Froelicher. On the Mechanical Reliability of Photo-BCB-Based Thin Film Dielectric Polymer for Electronic Packaging Applications. *Journal of Electronic Packaging*, 122(1):28–33, 2000.